Synthetic, Spectroscopic, and Theoretical Investigations into the Interactions and Detoxification of Nitric Oxide in Biology

by

Timothy C. Berto

A dissertation submitted in partial fulfillment
of the requirements for the degree of
Doctor of Philosophy
(Chemistry)
in The University of Michigan
2012

Doctoral Committee:

Associate Professor Nicolai Lehnert, Chair
Assistant Professor Bart M. Bartlett
Professor Mark E. Meyerhoff
Professor Ruma V. Banerjee

Dedication

This thesis is dedicated to my family; Ken, Andrea, and Tristan.

Acknowledgements

I would like to acknowledge the continuous support of my friends and family who have stuck with me during my doctoral work. I also need to thank my grandfather Walter Plaut and my uncle Steve Dunn for developing my interest in science from a young age. My teachers and professors throughout high school and college, in particular Mr. Singstock and Dr. Kari Cunningham, helped to advance my curiosity and ultimately carried me to where I am today. Finally, I need to express my gratitude to Dr. Nicolai Lehnert and the members of the Lehnert lab whose guidance and support are much appreciated. I am deeply grateful for the guidance and direction Nicolai provided during my doctoral work. I also need to specifically thank Lauren Goodrich who helped to keep me sane during five years of hard work.

Table of Contents

List of Tables

List of Figures

List of Schemes

Abstract

Bacterial nitric oxide reductase (NorBC) is responsible for NO reduction in denitrifying bacteria. This enzyme contains a dinuclear heme/non-heme iron active site in which the heme and non-heme iron centers are separated by only 3-4 Å. The mechanism of NO reduction in NorBC is of current interest and several possible mechanisms have been proposed for this enzyme. This work is focused on elucidating the mechanism of NorBC through the interaction of heme and non-heme iron nitrosyl model complexes. A six-coordinate heme nitrosyl model for the heme b_3 center of NorBC has been synthesized. Through the use of a covalently tethered imidazole moiety, this species is able to maintain a six-coordinate ferrous heme nitrosyl in solution without the need for excess base. Additionally, the non-heme iron site of NorBC has been modeled using ferrous complexes of substituted tris(2-pyridalmethyl)amine or di-2-picolyl amine derivatives. Covalent linkage of the heme and non-heme components yields a system which is structurally very similar to the NorBC active site. Reactivity studies between separate heme and non-heme iron nitrosyls as well as within the covalently linked complex are presented in an effort to elucidate the mechanism of NO reduction by NorBC. In particular, our results point away from a radical-based N-N coupling strategy as previously proposed but rather suggest a redox driven process. Finally, as enzymatic intermediates have yet to be isolated, the hyponitrite-bridged complex $[(OEP)Fe]_2(\mu\text{-}N_2O_2)$ has been examined as a model for bound $N_2O_2^{2-}$ within the dinuclear NorBC active site.

Chapter 1

Introduction

Historically, nitric oxide (NO) was often thought of as an environmental pollutant, due to its toxic and corrosive properties. NO is generated by the burning of fossil fuels and is a major component of automotive exhaust. Together with its homolog nitrogen dioxide (NO_2), it is one of the main contributors to smog and ozone depletion. NO is poisonous to humans at very low concentrations of only 100 ppm in air. Prior to the 1980s, NO was mostly used as a 'spin-label probe' to study the interactions of ferrous heme centers with O_2 in a variety of proteins. However, in the early 1980s it was discovered that the human body is capable of NO biosynthesis for the purpose of immune defense and signaling.[1-7] In 1992, NO was selected as the molecule of the year by the magazine Science.[8] Six years later, the Nobel Prize in Medicine was awarded to Furchgott, Ignarro and Murad for the discovery that nitric oxide is a signaling molecule in the cardiovascular system.[9-11]

1.1. Nitric Oxide Signaling and Biosynthesis

The biosynthesis of nitric oxide (NO) within humans and other mammals is facilitated by nitric oxide synthase (NOS) isozymes, which belong to the cytochrome P450 superfamily.[12] These enzymes are found throughout the human body and occur as three distinct classes which can be defined by their particular location and function.[4, 13] Each isozyme contains a similar heme active site which is responsible for the oxidation/hydroxylation of the substrate through heme-bound O_2-derived oxidants. Of the three isozymes, neuronal (*n*-) and endothelial (*e*-) NOS are found within neuronal cells in the brain and endothelial cells of inner artery walls, respectively, and are involved in signaling. Both of these NOS isozymes are sometimes referred to as 'constitutive' NOS (cNOS).[14] Constitutive NOS are constantly present in cells and are strictly regulated by the calcium ion concentration via calmodulin. Neuronal and endothelial NOS both produce NO as a signaling agent, which is responsible for nerve signal transduction, in the case of *n*-NOS, and blood

pressure control, in the case of *e*-NOS. For these applications, NO concentrations in the nanomolar range are used in order to avoid undesired toxic effects. Aside from signaling, NO is also a very effective immune defense agent. For example, it has been shown that NO exposure kills > 99% of *Mycobacterium tuberculosis* cells at concentrations of < 100 ppm.[15] In order to take advantage of this efficient antibacterial property, inducible (*i*-) NOS is used by macrophages to generate NO in micromolar concentrations as a means of immune defense. In contrast to the constitutive NOS enzymes discussed above, *i*-NOS is only expressed in response to bacterial infections, and is *de facto* not regulated by calmodulin. The use of NO in immune defense, however, can also lead to negative health effects: excessive NO production, for example in the case of severe or chronic bacterial infections, can lead to nitrosative stress, which, just like oxidative stress, has been related to many health problems[16] including the initiation of cancer,[17] cell damage and death (for example in stroke), atherogenesis, insulin-dependent diabetes mellitus,[18-20] septic shock,[21-23] sporadic Parkinson's disease,[24-27] and possibly multiple sclerosis.[28]

1.2. Detoxification of NO in Biological Systems

Due to its toxicity at high (μM) concentrations, NO production is tightly regulated in mammalian species. This is done primarily through control of the NOS isozymes. However, unlike bacteria and fungi, mammals lack an efficient means of NO detoxification. The primary means of NO detoxification in mammals is through NO dioxygenation (NOD), in which oxygenated Hb or Mb react with free NO to give nitrate and metHb/Mb.[29-30] However, this process is only viable under healthy O_2 levels. Excessively high concentrations of NO will deplete dioxygen through the formation of nitrate, rendering the NOD mechanism useless. Additionally, NO can be scavenged by ferrous deoxyHb/Mb.[31] Due to the extremely high binding constant of NO to ferrous heme centers, deoxygenated Hb and Mb make excellent NO scavengers.[32] Unfortunately, as with NOD, elevated NO concentration leads to an abundance of Hb/Mb-NO and inhibits NO scavenging.

1.3. Bacterial Nitric Oxide Reductase (NorBC)

Soil dwelling bacteria responsible for the breakdown of nitrogen oxides play a vital role in the greater nitrogen cycle. Such bacteria exist in mainly anaerobic conditions and thus must possess a method of respiration that does

not require the presence of dioxygen. To this end, denitrifying bacteria such as *Pseudomonas stutzeri, Paracoccus halodenitrificans,* and *Paracoccus denitrificans* contain a series of enzymes responsible for the stepwise reduction of nitrate to dinitrogen following the overall equation:[33-34]

$$2NO_3^- + 10e^- + 12H^+ \rightarrow N_2 + 6H_2O \quad (3)$$

The stepwise equation for bacterial denitrification is then:

$$2NO_3^- \rightarrow 2NO_2^- \rightarrow 2NO \rightarrow N_2O \rightarrow N_2 \quad (4)$$

wherein each step is catalyzed by different classes of enzymes. Through this systematic reduction of nitrate, these bacteria not only generate the proton gradient necessary for respiration, but also recycle plant waste and excess fertilizer into dinitrogen, completing the nitrogen cycle. Of particular interest is the detoxification of nitric oxide by bacterial NOR to yield less toxic nitrous oxide.[35] The overall reaction requires two equivalents of NO and corresponds to a net two-electron reduction:

$$2NO + 2e^- + 2H^+ \rightarrow N_2O + H_2O \quad (5)$$

There are three distinct classes of bacterial NORs that are defined by their electron source. Of these species, those which derive their electrons from cytochrome c (cNORs) are most commonly encountered.[33, 36] Other types, qNOR and qCu_ANOR, derive their electrons from quinones such as ubihydroquinone or menahydroquinone.[37-38] These so called alternative NORs will be discussed

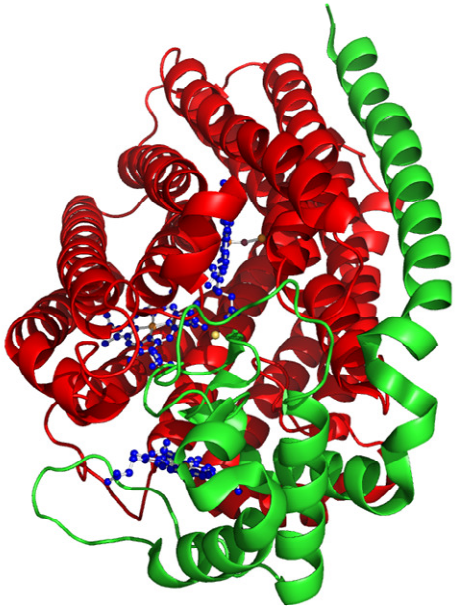

Figure 1.1. Crystal structure of NorBC in the ferric oxo-bridged resting state. The NorC and NorB subunits are shown in green and red, respectively. Heme cofactors are shown in blue. Generated using pymol from PDB 3O0R.

separately at the end of this section as most of what is known about bacterial NORs has been derived from the two-subunit cNOR enzyme, NorBC. Commonly purified from *P. denitrificans*, NorBC is generally representative of denitrifying bacterial NORs as all three varieties contain the same basic active site.[33, 39] Structurally, NorBC is a heterodimer (αβ) composed of a NorB and a NorC component as the name suggests (see Figure 1.1). The NorC subunit is a small 17 kDa protein which is primarily responsible for electron transfer. This component contains a single low-spin heme *c* redox center and shuttles electrons to NorB where the active site is located. The NorB subunit is a 56 kDa protein containing a redox active low-spin heme *b* which functions as the electron transfer center to the actual active site. The catalytically active di-iron site is also contained within NorB and is comprised of a second, high-spin heme *b*, termed heme b_3 due to its similarity to heme a_3 from cytochrome c oxidase, and an adjacent non-heme iron center, termed Fe_B (*vide infra*).[34]

NorBC Active Site Structure

In the crystal structure of the oxidized, resting form of the protein, the

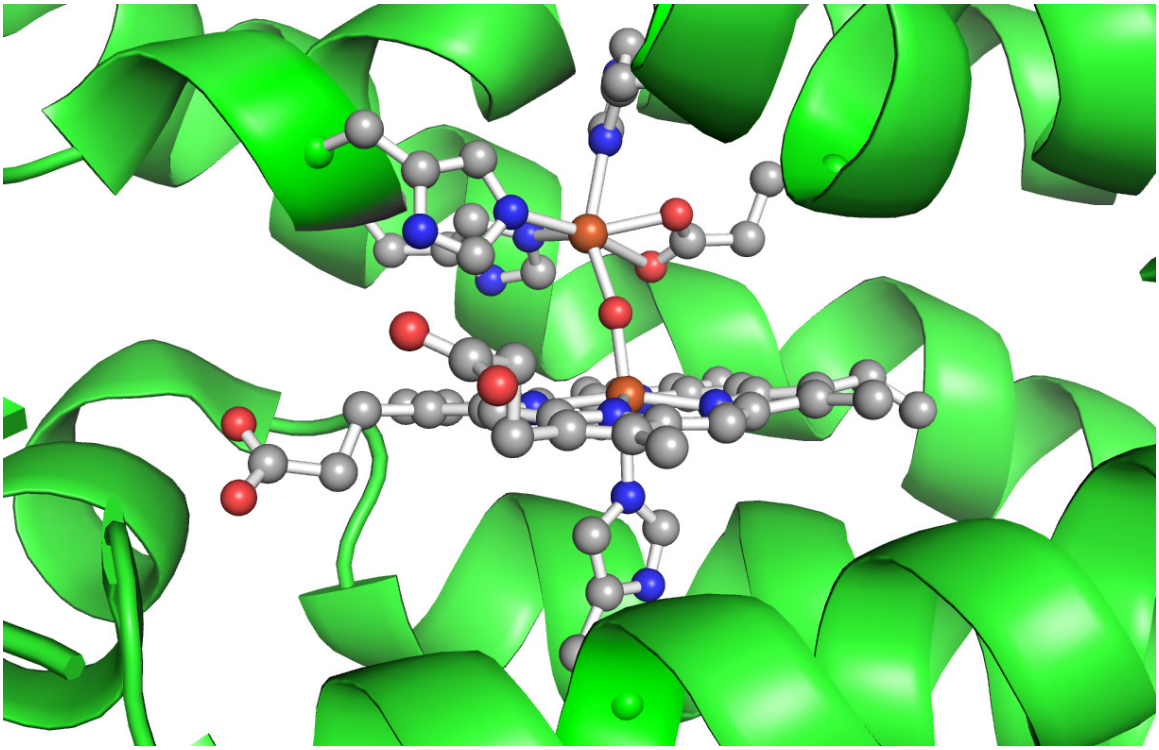

Figure 1.2. Crystallographically determined active site structure of NorBC. The non-heme Fe_B (top) is coordinated by three His residues and a single Glu. The heme b_3 (bottom) contains an axial His residue and is bridged to the Fe_B center through an oxo-bridge in the ferric resting state. Generated using pymol from PDB 3O0R.

non-heme Fe_B site is coordinated by three histidine residues, a glutamic acid, and an oxo bridge connecting it to the heme b_3 center in the di-ferric state of the active site (see Figure 1.2).[40] Several mechanisms have been proposed for NO reduction by NorBC. These include either a *trans*-type mechanism in which NO binds to both the heme b_3 and the non-heme Fe_B sites prior to formation of N_2O or a *cis*-type reaction where reduction takes place at a single iron center (see Scheme 1.1, below).[41-43] The details of this mechanism are currently being heavily investigated.[44-49]

Interestingly, detailed analyses of the amino acid sequences of NorBCs from different organisms[50-53] along with spectroscopic investigations[54-56] have shown that these enzymes are closely related to the respiratory heme-copper oxidases (HCOs) like cytochrome *c* oxidases (C*c*Os).[57] Divergent evolution of these two enzyme classes from a common NOR ancestor is the generally accepted explanation for these genetic, structural, and chemical similarities.[58-59] Due to this similarity, C*c*O was used as a blueprint for NorBC prior to its crystallographic identification in 2010.[40] A manifestation of this similarity is seen in the fact that HCOs are able to perform NOR chemistry and NorBC is able to perform HCO chemistry, albeit at significantly diminished capacity (see Table 1.1).

Table 1.1. Comparison of the catalytic activity for NOR and HCO enzymes.

Enzyme	Organism	NO reduction rate (mol NO/ mol min)	O_2 reduction rate (mol O_2/ mol min)	Reference
C*ba*$_3$O	*T. thermophilus*	3.0 ± 0.7 (20 ºC)		[60]
C*aa*$_3$O	*T. thermophilus*	32 ± 8 (20 ºC)		[60-61], [62]
	Bovine midochondria		3870 (37 ºC)	
C*bb*$_3$O	*P. stutzeri*	100 ± 9 (20 ºC)		[63]
C*bo*O	*E. coli*		4545 (35 ºC)	[62]
C*bd*O	*E. coli*		3660 (35 ºC)	[62]
NorBC	*P. stutzeri*	2200 (30 ºC)		[64]
NorBC	*P. denitrificans*	4020 (20 ºC)	600 (20 ºC)	[65]

Mechanism of NO Reduction by NorBC

The extremely low midpoint potential (60 mV vs. SHE) of heme b_3 has been proposed to act as a barrier against the formation of a stable (catalytically inactive) ferrous heme-nitrosyl complex.[57, 66] On the other hand, EPR spectra recorded for the fully reduced enzyme from *Pseudomonas aeruginosa* in single turnover studies show the presence of a ferrous heme-nitrosyl species upon

addition of NO gas, indicating that a ferrous heme-nitrosyl is indeed involved in NorBC catalysis.[67] In general, EPR spectroscopy is a powerful technique for the identification of iron nitrosyl complexes in biology. The EPR spectra of heme-nitrosyls show characteristic hyperfine splittings, due to the inherent nuclear spin of either ^{14}N or ^{15}N (I = 1 and I = ½, respectively) of the bound NO.[68] EPR-spectral features of reduced NorBC in the presence of NO were observed at g values of 2.08 and 2.012, the latter showing a well-resolved three-line hyperfine pattern (A = 45.1 MHz) of ^{14}NO. These results indicate the presence of a five-coordinate ferrous heme b_3 nitrosyl complex, where the ferrous iron is bound to NO, but the bond to the proximal histidine is broken.[67, 69]

While it has been suggested that obtaining a fully reduced enzyme is not biologically feasible due to the low reduction potential of heme b_3 as mentioned above,[57, 66] it is likely that such a state is accessible in the presence of NO, in agreement with the spectroscopic results described above. Here, the energetically favorable formation of the Fe(II)-NO species may result in an effective reduction potential greater than what is observed in the absence of NO.[70] To further complicate the matter, recent reports by Watmough and coworkers indicate that the redox potential of the non-heme Fe_B may actually be quite similar to that of heme b_3.[39, 71]

EPR spectroscopic investigations under turn-over conditions further reveal the formation of a 'high-spin' non-heme ferrous nitrosyl with S = 3/2 ground state.[55] In agreement with this, addition of NO to NorBC from *Pseudomonas aeruginosa* results in the growth of a g = 4 signal in the EPR spectra, which is consistent with an S = 3/2 complex.[67] These signals are characteristic of ferrous non-heme iron nitrosyls in which the iron center transfers one electron to NO. The result of this is a high-spin ferric iron center (S = 5/2), antiferromagnetically coupled to the bound NO^- (S = 1) ligand, which gives a total spin of S = 3/2 for the complex.[72] In addition to the g = 4 signal described in this study, the characteristic g = 2 signal of a 5C ferrous heme-nitrosyl complex was observed in the EPR spectra of the *P. aeruginosa* enzyme as mentioned above.[67] However, as the diiron active site of NorBC is likely magnetically coupled, formation of a dinitrosyl adduct during turnover would be expected to result in an EPR-silent intermediate. It is therefore possible that the observed heme and non-heme iron nitrosyls are formed non-productively and do not represent true intermediates in the catalytically active enzyme. In terms of vibrational spectroscopy, resonance

Raman[73] and FT-IR[74] data of NorBC further indicate binding of a second molecule of NO to the ferrous heme center, in agreement with the extremely large association constants of ferrous hemes for NO.[32] In summary, these NO binding studies point toward the formation of both ferrous heme-nitrosyls and ferrous non-heme iron-NO complexes during turnover of NorBC. However, it is yet unclear whether the observed species are relevant intermediates in the catalytic cycle.

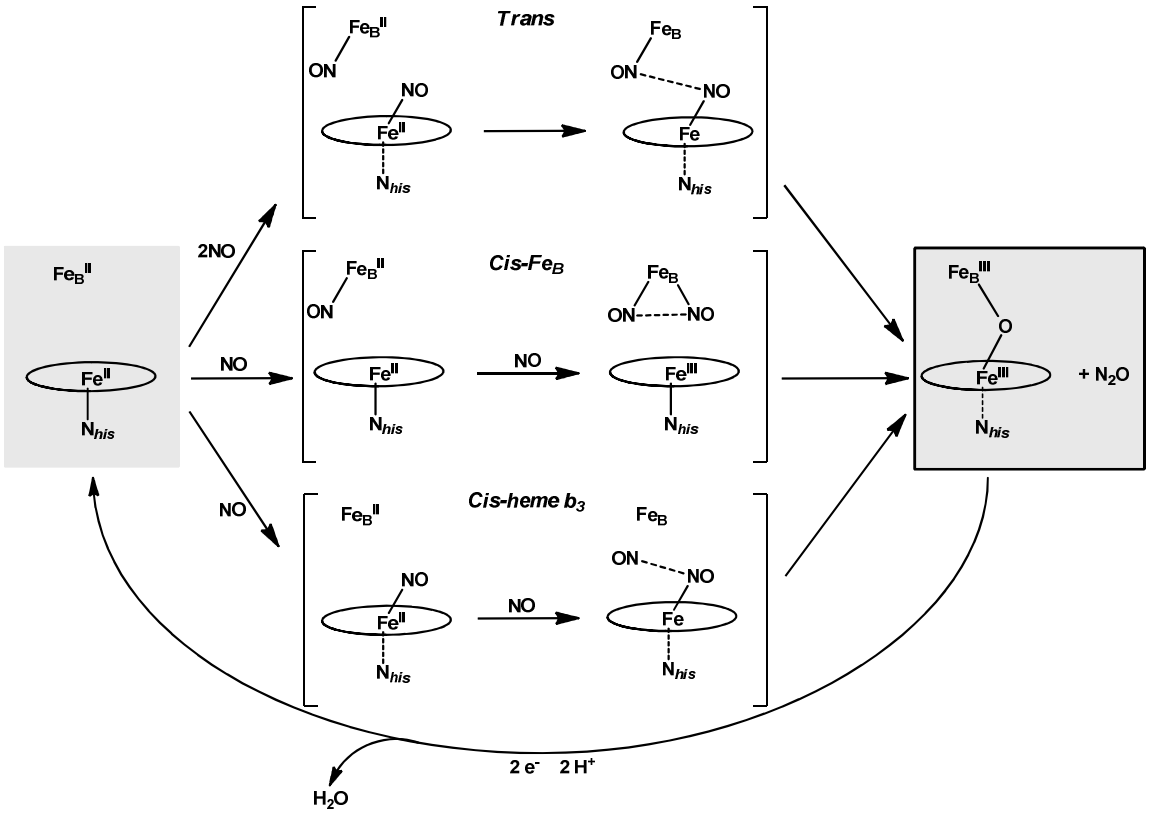

Scheme 1.1. General scheme of proposed *cis* and *trans* mechanisms for NO reduction by NorBC. The diferric oxo-bridged species (right) has been crystallographically characterized.

The molecular mechanism of NO reduction by NorBC is generally not well understood. In order to generate N_2O, two NO molecules must interact in such a way as to facilitate N-N bond formation. Subsequent scission of one of the N-O bonds then yields N_2O and a remaining oxygen atom, which is either protonated to form a hydroxy/water species or remains unprotonated as a μ-oxo bridge between the two catalytic iron centers.[75] The question is therefore how the two NO molecules initially bind to the diferrous active site of the enzyme, and subsequently react to form the necessary N-N bond. Currently, there are two

major theories on this matter, which are commonly described as the *cis* and *trans* mechanism as shown in Scheme 1.1.

In the case of the *trans* mechanism in Scheme 1.1, top,[76] two molecules of NO are bound to the diferrous active site, and then a radical type N-N bond formation is postulated. After release of N_2O, the two ferric iron centers are bridged by an oxo group.[54, 75-77] However, the detailed enzymatic mechanism involves many steps, and due to the lack of detailed kinetic studies, the rate limiting step is not well defined.[34, 76] In particular, no intermediate of this mechanism has ever been observed, which renders its central part, the N-N coupling, speculative. From DFT calculations[78] and in analogy to the proposed mechanism for the reduction of NO by HCOs,[79-81] a bridging hyponitrite complex is proposed as the intermediate. Interestingly, a corresponding model complex where hyponitrite bridges two hemes has recently been structurally characterized (see Chapter 5).[82] Alternative *cis* mechanisms have also been proposed, where, for example, only one of the two metal sites (heme or non-heme) reacts directly with NO, whereas the other metal only serves as an electron reservoir.[34, 83-85] Another important question, the coordination number of the heme-nitrosyl, is an additional issue: since ferrous heme-nitrosyls are notoriously stable and unreactive,[86] the proximal His ligand could help activate bound NO for catalysis. Due to the 'sharing' of the d_{z^2} orbital of iron(II) between the proximal His (imidazole) ligand and NO, this His ligand has the potential to regulate the electronic structure of NO bound in *trans* position to the ferrous heme.[56, 87-89]

Importantly, the observation of both ferrous heme b_3 and non-heme Fe_B nitrosyls during enzyme turnover as described above provides strong evidence in favor of the *trans* mechanism.[67, 75] However, due to spin coupling between the ferrous heme and non-heme iron nitrosyl complexes, EPR cannot observe intermediates in which the two bound NO molecules begin to interact. Here, antiferromagnetic coupling between the S = 1/2 heme b_3 nitrosyl and the S = 3/2 Fe_B(II)-NO complex leads to an EPR-silent S = 1 species. It is therefore unclear whether the observed 5C ferrous heme-nitrosyl (S = 1/2) and ferrous non-heme nitrosyl (S = 3/2) complexes are in fact part of the catalytic mechanism of NorBC, or whether they reflect catalytically non-productive binding modes of NO. Because the two iron centers within the active site pocket of NorBC are only about 3.5 Å apart (in the diferric μ-oxo complex),[34] N-N coupling would certainly be feasible with each NO bound to a different iron center.

In the *cis* mechanism shown in Scheme 1.1, both equivalents of NO interact at the same iron center, either heme b_3 or Fe_B. Support for both of the possible *cis* mechanisms comes mostly from mechanistic insight obtained for other NO reducing enzymes. Fungal NO reductase (P450nor) contains a single heme active site without the presence of a neighboring non-heme iron center. As a result, both equivalents of NO interact at the single heme site to generate the reduced product N_2O.[90-91] The possibility of a *cis* heme b_3 mechanism was also postulated based on UV-Visible absorption measurements on the interaction of fully reduced NorBC with NO.[92] The proposal of two NO molecules binding and reacting at the Fe_B site takes root from cytochrome *bo₃* studies, which proposed NO reductase activity of this enzyme as a result of reductive NO coupling at the Cu_B site of the enzyme.[84] Due to the striking similarity between the active site structures of NorBC and cytochrome bo_3 (*vide supra*), the *cis* Fe_B mechanism appeared plausible. Casting doubt on the *cis* mechanisms, however, is the fact that both heme b_3 and Fe_B ferrous nitrosyl species have been observed during NorBC turnover using EPR spectroscopy, as described above.[55, 69,67, 75] Additionally, the formation of two equivalents of nitroxyl (NO^-) at the non-heme Fe_B site via two consecutive electron transfer steps from the heme b_3 is unlikely. As the enzyme has been shown to function from the fully reduced Fe^{II}/Fe^{II} state and reach a diferric oxo-bridged resting state, the stepwise formation of two equivalents of NO^- would thus represent a four-electron process. Such a scenario is inconsistent with experimental evidence.

One other intriguing possibility is that the non-heme iron site transiently binds NO *en route* to formation of the observed heme-nitrosyl.[92] Evidence for this idea comes from flow-flash experiments utilizing CO-bound fully reduced NorBC coupled to optical absorbtion spectroscopy. The results indicate that NO binding to the heme b_3 is not dependent on bulk NO concentration. This observation points to the possibility of NO binding to other sites within the protein prior to coordinating to the active site heme. It could be envisioned that upon flash removal of CO, NO is already bound in the active site pocket, and thus, heme-nitrosyl formation is not dependent on the bulk NO concentration. A likely location for NO binding in this sense would be the non-heme Fe_B center. Here, a ferrous non-heme iron-nitrosyl would not be experimentally visible in the obtained optical spectra, which are dominated by the intense absorption bands of the heme b_3. While these data suggest binding of NO to both the heme and the non-heme iron center of the active site, this does not necessarily point towards a *trans*-type mechanism.

In fact, such a scenario opens the possibility of Fe_B acting as an NO holding site, which simply supplies NO to the active heme b_3 where NO is then reduced in accordance with the *cis* heme b_3 mechanism.[92]

Also in accordance with the reduction of NO via a *cis* heme b_3 mechanism are DFT studies performed by Siegbahn and coworkers.[78, 93] In an earlier 2006 study, the preferred coordination environment of the non-heme Fe_B center was investigated along with the mechanism by which NO reduction occurs based on calculated free energy profiles. Comparison of octahedral versus tetrahedral Fe_B complexes reveals an undesirable stabilization of key reaction intermediates in the tetrahedral model. This initial study favors an octahedral coordination of Fe_B and a *cis* heme b_3 reaction pathway. A more recent publication has re-examined the mechanism of NO reduction by NorBC using hybrid DFT calculations and an active site model based on the recently published crystal structure of NorBC.[40] Here, a comparison of *trans* versus *cis* heme b_3 mechanisms again favors the *cis* pathway. More specifically, the hyponitrite intermediate formed from the *cis* heme b_3 mechanism leads to a much more stable dianionic *cis* bound $N_2O_2^{2-}$ as compared to *trans*-bound hyponitrite intermediate which is disfavored by 16.9 kcal/mol over the diferric oxo-bridged resting state.

1.4. Scope of Thesis

This thesis is focused on the interaction of nitric oxide with ferrous iron complexes with the goal of modeling and elucidating the mechanism of NO reduction in bacterial nitric oxide reductase. Chapter 2 focuses on our efforts to model the heme b_3 center of NorBC using synthetic porphyrin model complexes. Here, a tetraphenylporphyrin macrocycle is modified to contain a covalently bound imidazole tether at one of the phenyl positions in order to mimic the histidine residue found in NorBC. The corresponding six-coordinate synthetic heme nitrosyl adduct is then characterized in detail using a variety of spectroscopic techniques. The work presented in Chapter 2 was performed in conjunction with Dr. V. K. K. Praneeth who developed the initial synthesis of the porphyrin ligands and corresponding nitrosyl complexes along with preliminary spectroscopic characterization. Fitting of the EPR spectra was performed by L. E. Goodrich. Chapter 2 is adapted with permission from Berto, T. C.; Praneeth, V. K. K.; Goodrich, L. E.; Lehnert, N. *J. Am. Chem. Soc.* **2009**, *131*, 17116-17126.

Chapter 3 focuses on model complexes based on the non-heme iron (Fe_B) center found in the active site of NorBC. This chapter is divided into two sections. Section 1 employs iron nitrosyl adducts of the BMPA-Pr ligand, first synthesized in our laboratory by Y. Murata and M. B. Hoffman, with counter ions of OTf^-, Cl^-, and ClO_4^-. Here, crystal structures and detailed spectroscopic analysis are presented (X-ray crystallographic analysis performed by K. B. Landenberger). The results indicate that NorBC may be able to modulate the degree of NO^- character at the Fe_B center through hydrogen bonding or other effects that moderate the effective nuclear charge of iron. Section 1 of chapter 3 is adapted with permission from Berto, T. C., Hoffman, M. B.; Murata, Y.; Landenberger, K. B.; Alp, E. E.; Zhao, J.; Lehnert, N. *J. Am. Chem. Soc.* **2011**, *133*, 16714-16717. Section 2 of chapter 3 focuses on alternative non-heme systems with ligands such as BEPA-Pr and BMPA-PhO. The corresponding ferrous non-heme iron nitrosyl complexes are again analyzed spectroscopically in an attempt to obtain information about the mechanism of NO reduction by NorBC.

Chapter 4 focuses on the interaction of the heme and non-heme iron nitrosyls discussed in chapters 2 and 3. Section 1 of this chapter also contains reactivity studies between various heme and non-heme iron nitrosyls as well as the reaction of these complexes with radical species. Section 2 contains preliminary results obtained for a covalently linked heme/non-heme diiron complex which represents a full synthetic model for the diiron active site of NorBC.

Chapter 5 focuses on the model complex $Fe_2OEP_2(N_2O_2)$ which represents a model for the proposed hyponitrite intermediate formed during NO reduction by NorBC. In section 1 the complex is introduced and its spectroscopic properties are presented. Section 2 focuses on its decomposition pathways which have been investigated using DFT, UV-Visible absorption, and EPR techniques. Analysis of the decomposition pathway sheds light on the opposing mechanism proposed for NorBC where hyponitrite is formed by the coupling of two NO molecules. The work presented in chapter 5 represents a collaboration with Dr. George Richter-Addo at the University of Oklahoma. The compound $[(OEP)Fe]_2(\mu\text{-}N_2O_2)$ studied in this chapter was synthesized by N. Xu in the Richter-Addo laboratory. Our role was then the detailed characterization and investigation of the reactivity of $[(OEP)Fe]_2(\mu\text{-}N_2O_2)$. A manuscript is currently in preparation for this work.

Chapter 6 focuses on a tangent DFT study which was preformed to elucidate the potential role of Hb/Mb-NO_2 in hypoxic signaling. Here, the interaction of NO with a simulated model of Hb/Mb-NO_2 shows that N_2O_3 formation is energetically feasible provided that nitrite is coordinated through one of its O-atoms to the heme center. Chapter 6 is adapted with permission from Berto, T. C.; Lehnert, N. *Inorg. Chem.* **2011**, *50*, 7361-7363.

References

(1) Moncada, S.; Palmer, R. M.; Higgs, E. A., Nitric oxide: physiology, pathophysiology, and pharmacology. *Pharmacol. Rev.* **1991,** *43*.
(2) Snyder, S. H., Nitric oxide: first in a new class of neurotransmitters. *Science* **1992,** *257*.
(3) Butler, A. R.; Williams, D. L. H., The physiological role of nitric oxide. *Chem. Soc. Rev.* **1993**.
(4) Bredt, D. S.; Snyder, S. H., Nitric Oxide: A Physiologic Messenger Molecule. *Annu. Rev. Biochem.* **1994,** *63*.
(5) Lancaster, J. R., Jr., In *Encyclopedia of Inorganic Chemistry*, Bruce, R. B., Ed. Wiley: Chichester, 1994.
(6) Feelisch, M.; Stamler, J. S., *Methods in Nitric Oxide Research*. Wiley: Chichester, 1996.
(7) Ignarro, L., *Nitric Oxide: Biology and Pathobiology*. Academic Press: San Diego, 2000.
(8) Culotta, E.; Koshland, D. E., Jr., NO news is good news. *Science* **1992,** *258*.
(9) Murad, F., *Angew. Chem. Int. Ed.* **1999,** *38*.
(10) Furchgott, R. F., *Angew. Chem. Int. Ed.* **1999,** *38*.
(11) Ignarro, L., *Angew. Chem. Int. Ed.* **1999,** *38*.
(12) White, K. A.; Marletta, M. A., Nitric oxide synthase is a cytochrome P-450 type hemoprotein. *Biochemistry* **1992,** *31* (29).
(13) Stuehr, D. J., Structure-Function Aspects in the Nitric Oxide Synthases. *Annu. Rev. Pharmacol. Toxicol.* **1997,** *37*.
(14) Wink, D. A.; Mitchell, J. B., Chemical biology of nitric oxide: insights into regulatory, cytotoxic, and cytoprotective mechanisms of nitric oxide. *Free Rad. Biol. Med.* **1998,** *25* (4-5).
(15) Long, R.; Light, B.; Talbot, J. A., Mycobacteriocidal action of exogenous nitric oxide. *Antimicrob. Agents Chemother.* **1999,** *43*.
(16) Wink, D. A.; Miranda, K. M.; Espey, M. G., Cytotoxicity Related to Oxidative and Nitrosative Stress by Nitric Oxide. *Exp. Biol. Med.* **2001,** *226*.
(17) Wink, D. A.; Mitchell, J. B., NITRIC OXIDE AND CANCER: AN INTRODUCTION. *Free Rad. Biol. Med.* **2003,** *34*.
(18) Corbett, J. A.; Lancaster, J. R., Jr.; Sweetland, M. A.; McDaniel, M. L., Interleukin-1 β-induced formation of EPR-detectable iron-nitrosyl complexes in islets of Langerhans. Role of nitric oxide in interleukin-1 beta-induced inhibition of insulin secretion. *J. Biol. Chem.* **1991,** *266*.
(19) Corbett, J. A.; Tilton, R. G.; Chang, K.; Hasen, K. S.; Ido, Y.; Wang, J. L.; Sweetland, M. A.; Lancaster, J. R., Jr.; Williamson, J. R.; McDaniel, M. L., *Diabetes* **1992,** *41*.
(20) Corbett, J. A.; Wang, J. L.; Sweetland, M. A.; Lancaster, J. R., Jr.; McDaniel, M. L., *J. Clin. Invest.* **1992,** *90*.
(21) Vincent, J.-L.; Zhang, H.; Szabo, C.; Preiser, J.-C., Effects of Nitric Oxide in Septic Shock. *Am. J. Respir. Crit. Care Med.* **2000,** *161*.
(22) Thiemermann, C., Nitric oxide and septic shock. *Gen. Pharmacol.* **1997,** *29*.
(23) Kuhl, S. J.; Rosen, H., Nitric oxide and septic shock. From bench to bedside. *West. J. Med.* **1998,** *163*.
(24) Benhar, M.; Forrester, M. T.; Stamler, J. S., Nitrosative stress in the ER: a new role for S-nitrosylation in neurodegenerative diseases. *ACS Chem. Biol.* **2006,** *1*.

(25) Yao, D.; Gu, Z.; Nakamura, T.; Shi, Z.-Q.; Ma, Y.; Gaston, B.; Palmer, L. A.; Rockenstein, E. M.; Zhang, Z.; Masliah, E.; Uehara, T.; Lipton, S. A., Nitrosative stress linked to sporadic Parkinson's disease: S-nitrosylation of parkin regulates its E3 ubiquitin ligase activity *Proc. Natl. Acad. Sci. USA* **2004,** *101*.
(26) Klatt, P.; Lamas, S., Regulation of protein function by S-glutathiolation in response to oxidative and nitrosative stress. *Eur. J. Biochem.* **2000,** *267*.
(27) Tylor, B. S.; Kion, Y. M.; Wang, Q. I.; Sharpio, R. A.; Billiar, T. R.; Geller, D. A., Nitric oxide down regulates hepatocyte-inducible nitric oxide synthase gene expression. *Arch. Surg.* **1997,** *1*.
(28) Lin, R. F.; Lin, T.-S.; Tilton, R. G.; Cross, A. H., *J. Exp. Med.* **1993,** *178*, 643.
(29) Eich, R. F., *Biochemistry and cell biology*. Rice University: Houston, 1997.
(30) Eich, R. F.; Li, T.; Lemon, D. D.; Doherty, D. H.; Curry, S. R.; Aitken, J. F.; Mathews, A. J.; Johnson, K. A.; Smith, R. D.; Phillips, G. N., Jr.; Olson, J. S., Mechanism of NO-induced oxidation of myoglobin and hemoglobin. *Biochemistry* **1996,** *35*.
(31) Gow, A.; Luchsinger, B. P.; Pawloski, J. R.; Singel, D. J.; Stamler, J. S., *Proc. Natl. Acad. Sci. USA* **1999,** *96*.
(32) Cooper, C. E., Nitric oxide and iron proteins. *Biochim. Biophys. Acta* **1999,** *1411*.
(33) Wasser, I. M.; deVries, S.; Moënne-Loccoz, P.; Schröder, I.; Karlin, K. D., Nitric Oxide in Biological Denitrification: Fe/Cu Metalloenzymes and Metal Complex NO_x Redox Chemistry. *Chem. Rev.* **2002,** *102*.
(34) Zumft, W. G., Nitric oxide reductases of prokaryotes with emphasis on the respiratory, heme–copper oxidase type. *J. Inorg. Biochem.* **2005,** *99*.
(35) Field, S. J.; Prior, L.; Roldán, M. D.; Cheesman, M. R.; Thomson, A. J.; Spiro, S.; Butt, J. N.; Watmough, N. J.; Richardson, D. J., Spectral Properties of Bacterial Nitric-oxide Reductase: RESOLUTION OF pH-DEPENDENT FORMS OF THE ACTIVE SITE HEMEb 3 *J. Biol. Chem.* **2002,** *277*.
(36) Hendriks, J.; Oubrie, A.; Castresana, J.; Urbani, A.; Gemeinhardt, S.; Saraste, M., Nitric oxide reductases in bacteria. *Biochim. Biophys. Acta, Bioenerg.* **2000,** *1459* (2-3).
(37) Cramm, R.; Pohlmann, A.; Friedrich, B., Purification and characterization of the single-component nitric oxide reductase from Ralstonia eutropha H16. *FEBS Lett.* **1999,** *460* (1).
(38) Suharti; Strampraad, M. J. F.; Schroder, I.; de Vries, S., A novel copper A containing menaquinol NO reductase from Bacillus azotoformans. *Biochemistry* **2001,** *40* (8).
(39) Watmough, N. J.; Field, S. J.; Hughes, R. J. L.; Richardson, D. J., The Bacterial Respiratory Nitric Oxide Reductase. *Biochem. Soc. Trans.* **2009,** *37*.
(40) Hino, T.; Matsumoto, Y.; Nagano, S.; Sugimoto, H.; Fukumori, Y.; Murata, T.; Iwata, S.; Shiro, Y., *Science* **2010,** *330*, 1666.
(41) Butler, C. S.; Seward, H. E.; Greenwood, C.; Thomson, A. J., *Biochemistry* **1997,** *36*, 16259.
(42) Girsch, P.; de Vries, S., *Biochem. Biophys. Acta* **1997,** *1318*, 202.
(43) Watmough, N. J.; Cheesman, M. R.; Butler, C. S.; Little, R. H.; Greenwood, C.; Thomson, A. J., *J. Bioenerg. Biomemb.* **1998,** *30*, 55.
(44) Berto, T. C.; Hoffman, M. B.; Murata, Y.; Landenberger, K. B.; Alp, E. E.; Zhao, J.; Lehnert, N., *J. Am. Chem. Soc.* **2011,** *133*, 16714.
(45) Berto, T. C.; Praneeth, V. K. K.; Goodrich, L. E.; Lehnert, N., *J. Am. Chem. Soc.* **2009,** *131*, 17116.

(46) Collman, J. P.; Yang, Y.; Dey, A.; Decreau, R. A.; Ghosh, S.; Ohta, T.; Solomon, E. I., *Proc. Natl. Acad. Sci. USA* **2008,** *105*, 15660.
(47) Hayashi, T.; Miner, K. D.; Yeung, N.; Lin, Y.-W.; Lu, Y.; Moenne-Loccoz, P., *Biochemistry* **2011,** *50*, 5939.
(48) Wasser, I. M.; Huang, H.-W.; Moenne-Loccoz, P.; Karlin, K. D., *J. Am. Chem. Soc.* **2005,** *127*, 3310.
(49) Yeung, N.; Lin, Y.-W.; Gao, Y.-G.; Zhao, X.; Russell, B. S.; Lei, L.; Miner, K. D.; Robinson, H.; Lu, Y., *Nature* **2009,** *462*, 1079.
(50) van der Oost, J.; de Boer, A. P. N.; de Gier, J.-W. L.; Zumft, W. G.; Stouthamer, A. H.; van Spanning, R. J. M., The heme-copper oxidase family consists of three distinct types of terminal oxidases and is related to nitric oxide reductase. *FEMS Microbiol. Lett.* **1994,** *121*.
(51) Saraste, M.; Castresana, J., Cytochrome oxidase evolved by tinkering with denitrification enzymes. *FEBS Lett.* **1994,** *341*.
(52) Arai, H.; Igarashi, Y.; Kodama, T., The structural genes for nitric oxide reductase from Pseudomonas aeruginosa. *Biochim. Biophys. Acta* **1995,** *1261*.
(53) de Boer, A. P. N.; van der Oost, J.; Reijnders, W. N. M.; Westerhoff, H. V.; Stouthamer, A. H.; van Spanning, R. J. M., Mutational analysis of the nor gene cluster which encodes nitric-oxide reductase from Paracoccus denitrificans. *Eur. J. Biochem.* **1996,** *242*.
(54) Cheesman, M. R.; Zumft, W. G.; Thomson, A. J., The MCD and EPR of the Heme Centers of Nitric Oxide Reductase from Pseudomonas stutzeri: Evidence That the Enzyme Is Structurally Related to the Heme-Copper Oxidases. *Biochemistry* **1998,** *37*.
(55) Hendriks, J.; Warne, A.; Gohlke, U.; Haltia, T.; Ludovici, C.; Lübben, M.; Saraste, M., The Active Site of the Bacterial Nitric Oxide Reductase Is a Dinuclear Iron Center. *Biochemistry* **1998,** *37*.
(56) Moënne-Loccoz, P.; de Vries, S., Structural Characterization of the Catalytic High-Spin Heme b of Nitric Oxide Reductase: A Resonance Raman Study. *J. Am. Chem. Soc.* **1998,** *120*.
(57) Grönberg, K. L. C.; Roldán, M. D.; Prior, L.; Butland, G.; Cheesman, M. R.; Richardson, D. J.; Spiro, S.; Thomson, A. J.; Watmough, N. J., A Low-Redox Potential Heme in the Dinuclear Center of Bacterial Nitric Oxide Reductase: Implications for the Evolution of Energy-Conserving Heme-Copper Oxidases. *Biochemistry* **1999,** *38*.
(58) Castresana, J.; Saraste, M., Evolution of energetic metabolism: the respiration-early hypothesis. *Trends in Biochem. Sci.* **1995,** *20* (11).
(59) Musser, S. M.; Chan, S. I., Evolution of the cytochrome c oxidase proton pump. *J. Mol. Evol.* **1998,** *46* (5).
(60) Giuffrè, A.; Stubauer, G.; Sarti, P.; Brunori, M.; zumft, W. G.; Buse, G.; Soulimane, T., The heme copper oxidases of *thermos theromophilus* catalyze the reduction of nitric oxide: Evolutionary implications. *Proc. Natl. Acad. Sci. USA* **1999,** *96*.
(61) Cooper, C. E.; Davies, N. A.; Psychoulis, M.; Canevari, L.; Bates, T. E.; Dobbie, M. S.; Casley, C. S.; Sharpe, M. A., Nitric oxide and peroxynitrite cause irreversible increases in the Km for oxygen of mitochondrial cytochrome oxidase: in vitro and in vivo studies. *Biochem. Biophys. Acta. Bioenerg.* **2003,** *1607* (1).
(62) Mason, M. G.; Shepherd, M.; Nicholls, P.; Dobbin, P. S.; Dodsworth, K. S.; Poole, R. K.; Cooper, C. E., Cytochrome bd confers nitric oxide resistance to Escherichia coli. *Nat. Chem. Biol.* **2008,** *5* (2).
(63) Forte, E.; Urbani, A.; Saraste, M.; Sarti, P.; Brunori, M.; Giuffrè, A., The cytochrome cbb3 from Pseudomonas stutzeri displays nitric oxide reductase activity. *Eur. J. Biochem.* **2001,** *268* (24).

(64) Heiss, B.; Frunzke, K.; Zumft, W. G., Formation of the NN bond from nitric oxide by a membrane-bound cytochrome bc complex of nitrate-respiring (denitrifying) Pseudomonas stutzeri. *J. Bacteriol.* **1989,** *171* (6).
(65) Fujiwara, T.; Fukumori, Y., Cytochrome cb-type nitric oxide reductase with cytochrome c oxidase activity from *Paracoccus denitrificans* ATCC 35512. *J. Bacteriol.* **1996,** *178*.
(66) Collman, J. P.; Yan, Y.-L.; Lei, L.; Dinolfo, P. H., Active-Site Models of Bacterial Nitric Oxide Reductase Featuring Tris-Histidyl and Glutamic Acid Mimics: Influence of a Carboxylate Ligand on FeB Binding and the Heme Fe/FeB Redox Potential *Inorg. Chem.* **2006,** *45*.
(67) Kumita, H.; Matsuura, K.; Hino, T.; Takahashi, S.; Hori, H.; Fukumori, Y.; Morishima, I.; Shiro, Y., NO reduction by nitric-oxide reductase from denitrifying bacterium Pseudomonas aeruginosa: characterization of reaction intermediates that appear in the single turnover cycle. *J. Biol. Chem.* **2004,** *279* (53).
(68) Lehnert, N., Electron Paramagnetic Resonance and Low-Temperature Magnetic Circular Dichroism Spectroscopy of Ferrous Heme Nitrosyls. In *The Smallest Biomolecules: Diatomics and their Interactions with Heme Proteins*, Ghosh, A., Ed. Elseviere: Amsterdam, 2008; pp 147-171.
(69) Sakurai, T.; Sakurai, N.; Matsumoto, H.; Hirota, S.; Yamauchi, O., Roles of Four Iron Centers in *Paracoccus halodenitrificans* Nitric Oxide Reductase. *Biochem. Biophys. Res. Commun.* **1998,** *251*.
(70) Kapetanaki, S. M.; Field, S. J.; Hughes, R. J. L.; Watmough, N. J.; Liebl, U.; Vos, M. H., Ultrafast ligand binding dynamics in the active site of native bacterial nitric oxide reductase. *Biochem. Biophys. Acta. Bioenerg.* **2008,** *1777* (7-8).
(71) Field, S. J.; Thorndycroft, F. H.; Matorin, A. D.; Richardson, D. J.; Watmough, N. J., The respiratory nitric oxide reductase (NorBC) from Paracoccus denitrificans. *Methods Enzymol.* **2008,** *437*.
(72) Brown, C. A.; Pavlosky, M. A.; Westre, T. E.; Zhang, Y.; Hedman, B.; Hodgson, K. O.; Solomon, E. I., Spectroscopic and Theoretical Description of the Electronic Structure of S = 3/2 Iron-Nitrosyl Complexes and Their Relation to O_2 Activation by Non-Heme Iron Enzyme Active Sites *J. Am. Chem. Soc.* **1995,** *117*.
(73) Pinakoulaki, E.; Gemeinhardt, S.; Saraste, M.; Varotsis, C., Nitric-oxide Reductase. Structure and Properties of the Catalytic Site from Resonance Raman Scattering. *J. Biol. Chem.* **2002,** *277*.
(74) Lu, S.; Suharti; de Vries, S.; Moënne-Loccoz, P., Two CO Molecules Can Bind Concomitantly at the Diiron Site of NO Reductase from *Bacillus azotoformans*. *J. Am. Chem. Soc.* **2004,** *126*.
(75) Moënne-Loccoz, P.; Richter, O.-M. H.; Huang, H.; Wasser, I. M.; Ghiladi, R. A.; Karlin, K. D.; de Vries, S., Nitric Oxide Reductase from Paracoccus denitrificans Contains an Oxo-Bridged Heme/Non-Heme Diiron Center *J. Am. Chem. Soc.* **2000,** *122*.
(76) Girsch, P.; de Vries, S., Purification and initial kinetic and spectroscopic characterization of NO reductase from Paracoccus denitrificans. *Biochim. Biophys. Acta* **1997,** *1318*.
(77) Martens, C. F.; Murthy, N. N.; Obias, H. V.; Karlin, K. D., Oxo-bridged haem/non-haem iron complexes. *Chem. Commun.* **1996**.
(78) Blomberg, L. M.; Blomberg, M. R. A.; Siegbahn, P. E. M., Reduction of nitric oxide in bacterial nitric oxide reductase - a theoretical model study. *Biochim. Biophys. Acta* **2006,** *1757*.

(79) Ohta, T.; Kitagawa, T.; Varotsis, C., Characterization of a Bimetallic-Bridging Intermediate in the Reduction of NO to N_2O: a Density Functional Theory Study. *Inorg. Chem.* **2006,** *45*.
(80) Blomberg, L. M.; Blomberg, M. R. A.; Siegbahn, P. E. M., A theoretical study on nitric oxide reductase activity in ba_3-type heme-copper oxidase. *Biochim. Biophys. Acta* **2006,** *1757*.
(81) Varotsis, C.; Ohta, T.; Kitagawa, T.; Soulimane, T.; Pinakoulaki, E., The Structure of the Hyponitrite Species in a Heme Fe-Cu Binuclear Center. *Angew. Chem. Int. Ed.* **2007,** *46*.
(82) Xu, N.; Campbell, A. L. O.; Powell, D. R.; Khandogin, J.; Richter-Addo, G. B., A Stable Hyponitrite-Bridged Iron Porphyrin Complex. *J. Am. Chem. Soc.* **2009,** *131*.
(83) Butler, C. S.; Seward, H. E.; Greenwood, C.; Thomson, A. J., *Fast* Cytochrome bo from Escherichia coli Binds Two Molecules of Nitric Oxide at Cu_B. *Biochemistry* **1997,** *36*.
(84) Watmough, N. J.; Cheesman, M. R.; Butler, C. S.; Little, R. H.; Greenwood, C.; Thomson, A. J., The Dinuclear Center of Cytochrome bo_3 from *Escherichia coli*. *J. Bioenerg. Biomemb.* **1998,** *30*.
(85) Lin, R.; Farmer, P. J., O Atom Transfer from Nitric Oxide Catalyzed by Fe(TPP). *J. Am. Chem. Soc.* **2001,** *123*.
(86) Lim, M. D.; Lorkovic, I. M.; Ford, P. C., NO and NO_x interactions with group 8 metalloporphyrins. *J. Inorg. Biochem.* **2005,** *99*.
(87) Praneeth, V. K. K.; Neese, F.; Lehnert, N., Spin Density Distribution in Five- and Six-Coordinate Iron(II)-Porphyrin NO Complexes Evidenced by Magnetic Circular Dichroism Spectroscopy *Inorg. Chem.* **2005,** *44*.
(88) Praneeth, V. K. K.; Näther, C.; Peters, G.; Lehnert, N., Spectroscopic Properties and Electronic Structure of Five- and Six-Coordinate Iron(II) Porphyrin NO Complexes: Effect of the Axial N-Donor Ligand *Inorg. Chem.* **2006,** *45*.
(89) Pinakoulaki, E.; Ohta, T.; Soulimane, T.; Kitagawa, T.; Varotsis, C., Detection of the His-Heme Fe^{2+}-NO Species in the Reduction of NO to N_2O by ba_3-Oxidase from *Thermus thermophilus J. Am. Chem. Soc.* **2005,** *127*.
(90) Daiber, A.; Shoun, H.; Ullrich, V., Nitric oxide reductase ($P450_{nor}$) from *Fusarium oxysporum*. *J. Inorg. Biochem.* **2005,** *99*.
(91) Shiro, Y.; Fujii, M.; Iizuka, T.; Adachi, S.; Tsukamoto, K.; Nakahara, K.; Shoun, H., Spectroscopic and Kinetic Studies on Reaction of Cytochrome P450nor with Nitric Oxide. *J. Biol. Chem.* **1995,** *270*.
(92) Hendriks, J.; Jasaitis, A.; Saraste, M.; Verkhovsky, M. I., Proton and Electron Pathways in the Bacterial Nitric Oxide Reductase. *Biochemistry* **2002,** *41* (7).
(93) Blomberg, M. R. A.; Siegbahn, P. E. M., *Biochemistry* **2012,** *51*, 5173.

Chapter 2

Synthetic Models for the Heme b_3 Site of NorBC

Membrane-bound proteins such as NorBC are notoriously difficult to isolate. Additionally, high enzymatic turnover rates and the inability to control proton donation make it a significant challenge to identify and characterize reaction intermediates for proton-dependent reactions. As a result, synthetic model complexes which are stable in organic solvents and amicable to a wide variety of spectroscopic analyses are ideally suited to the study of the mechanism of NO reduction by NorBC. In this chapter, a series of substituted tetraphenylporphyrin type macrocycles (TMP or T*o*-F_2PP) with covalently attached N-donor ligands (pyridine or imidazole linker) are reported. Linkers with varying chain lengths and designs have been applied to systematically investigate the effect of chain length and rigidity on the binding affinity of the linker to the corresponding Fe(II)-NO heme complexes. The binding of the linker is monitored in solution using a variety of spectroscopic methods including UV-Vis absorption, EPR, and IR spectroscopy. Both the N-O stretching frequency and the imidazole ^{14}N hyperfine coupling constants show a good correlation with the Fe-N-donor bond strength in these systems. The complexes with covalently attached pyridyl and alkyl imidazole ligands only exhibit weak interactions of the linker with iron(II). However, the stable six-coordinate complex [Fe(T*o*-F_2PP-BzIM)(NO)] (**4**) is obtained when a rigid benzyl linker is applied. This complex exhibits typical properties of six-coordinate ferrous heme-nitrosyls in which an N-donor ligand is bound *trans* to NO, including the Soret band at 427 nm and the typical nine line ^{14}N hyperfine splitting in the EPR spectrum. A crystal structure has been obtained for the corresponding zinc complex. This work represents the first systematic study on the requirements for the formation of stable six-coordinate ferrous heme nitrosyl complexes in solution at room temperature in the absence of excess axial N-donor ligand. Adapted with permission from Berto, T. C.; Praneeth, V. K. K.; Goodrich, L. E.; Lehnert, N. *J. Am. Chem. Soc.* **2009**, *131*, 17116-17126.

2.1. Six-Coordinate Ferrous Heme Nitrosyls

Introduction

Heme proteins are involved in many important biological processes, including electron transfer, catalysis, and signaling. Many of these functions involve the interaction of ferrous hemes with diatomics, in particular O_2, NO, and CO.[1] Because of the exceptional significance of heme diatomic interactions, much research has been devoted to the synthesis of model complexes for the corresponding heme proteins. In many cases, a proximal histidine is present as the *trans* ligand to the diatomic bound at the distal site. Prominent examples of this structural motif are found in the O_2 transport and storage proteins hemoglobin (Hb) and myoglobin (Mb), the NO sensor soluble guanylate cyclase (sGC), and peroxidases.[2] A similar active site with a copper center in close proximity is also found in cytochrome c oxidase (CcO). Here, the heme-copper center binds and reduces dioxygen, and thus facilitates respiration within living organisms. Finally, the active site of bacterial nitric oxide reductase (NorBC) contains a heme with axial histidine coordination, which has been proposed to influence the binding and reactivity of NO bound at the distal site.[3] Because of this, many synthetic model complexes, for example those of Mb, Hb, CcO, and NorBC, have been equipped with pyridine (Py) or imidazole (IM) type ligands that are covalently tethered to the porphyrin core in order to model this proximal histidine.[4]

Model systems of biological hemes that include the proximal histidine usually consist of a modified synthetic porphyrin with a covalently tethered N-donor ligand.[4] Original work in this field, carried out by Traylor and coworkers, led to the development of the so called “cyclophane” porphyrins[5] in which alkyl imidazole or thiolate linked chains were anchored at the β-pyrrole positions of protoheme.[4c, 6] These models served as mimics for the active sites of globins and peroxidases. In separate studies, tethers at the β-pyrrole positions of porphyrin ligands have also been used to covalently connect two separate hemes via peptide linkages.[7] Work by Dolphin and coworkers focused on the investigation of the electronic structure of such dimeric porphyrin species as a function of the length of the $(CH_2)_n$ tether (n = 0-8).[8] Later, Momenteau and coworkers were able to improve the solubility of imidazole-tethered protohemes through the use of propionic acid side chains.[6a, 9] While a considerable amount of insight has been gained from these β-pyrrole and propionic acid tethered model systems, they have been shown to exhibit

undesirable intermolecular binding through the tethered donor ligands.[9] As an alternative, the use of tetraphenylporphyrin derivatives offers a convenient strategy for attaching such tethers by substituting the *ortho* positions of the *meso*-phenyl groups available in these systems. These models offer the distinct benefit that, due to the perpendicular orientation of the phenyl rings with respect to the porphyrin plane, *ortho*-phenyl substituents are conveniently directed towards the axial positions of the heme center and thus, intermolecular interactions are avoided. Collman and coworkers have shown the utility of such systems through their use of multi-tethered "picket fence porphyrins" which employ either ether or amide linkages.[10] Walker and coworkers have also utilized such porphyrin model systems to elucidate the properties of cytochromes *c*, *b*, and a_3 with respect to axial N-donor ligand geometry.[4d, 11] Recently, model systems from the Collman, Karlin, and Naruta groups have continued to exploit the effectiveness of *meso*-phenyl tethered porphyrin systems in their models for the active site of cytochrome c oxidase.[12]

Our particular interest is focused on bacterial nitric oxide reductase (NorBC) which is an enzyme found in soil dwelling bacteria that is responsible for the conversion of nitric oxide (NO) to nitrous oxide (N_2O) via a two-electron reduction:

$$\mathbf{2NO + 2e^- + 2H^+ \rightarrow N_2O + H_2O} \qquad \mathbf{(1)}$$

This enzyme fulfills a vital role in the process of denitrification where nitrate is reduced in a stepwise fashion to dinitrogen.[13] The site of catalytic NO reduction within the enzyme consists of a dinuclear iron center with both heme and non-heme type coordination. The non-heme iron site has three histidine ligands and has been proposed to also contain glutamate ligation.[14] Located 3.5 Å from the non-heme iron is a heme *b* site with additional proximal histidine ligation similar to that seen in the heme active sites of Hb and Mb. The bi-metallic heme/non-heme motif is catalytically active in the diferrous form.[13] Detailed investigations into the properties and reactivity of the heme component of the active site of NorBC could, in principle, be based on the Mb and Hb model complexes described above. However, in the case of NorBC, the interaction of NO, rather than O_2 or CO, with ferrous heme model complexes needs to be studied to arrive at a detailed structural and mechanistic understanding of this enzyme. This has important consequences for the design of model systems as the generation of six-coordinate (6C) ferrous heme nitrosyls constitutes a significant challenge.

The question of axial ligand binding is of direct relevance for the reactivity of ferrous heme nitrosyls. It has been shown that the *trans* ligand modulates the amount of radical character on the NO, and hence, the chemical behavior of these complexes. This is evident from spectroscopic studies including EPR, MCD, vibrational spectroscopy (coupled to normal coordinate analysis), and DFT calculations on five- and six-coordinate ferrous heme nitrosyl model systems.[15] In five-coordinate (5C) complexes a strong Fe-NO σ-bond is present between the singly occupied π^* orbital of NO and d_{z^2} of Fe(II).[15c, d] Additional backbonding is observed between the d_{xz} and d_{yz} orbitals of iron and the remaining unoccupied π^* orbital of NO. The strong σ-bond and substantial sharing of the unpaired electron via the d_{z^2} orbital of iron gives rise to the strong σ-*trans* interaction between NO and the proximal N-donor ligand in the corresponding 6C complexes. This has two consequences: (a) the binding of axial ligands *trans* to NO is weak, and (b) upon coordination of an N-donor ligand *trans* to NO, the Fe-NO bond is weakened and the unpaired electron is pushed back from the iron(II) to the NO ligand resulting in an electronic structure with Fe(II)-NO(radical) character in the 6C case.[15c, d] In this way, the N-donor ligand could help to activate the bound NO for catalysis. This is particularly relevant for the activation of NO in NorBC since ferrous heme nitrosyls are intrinsically stable and unreactive.[16]

To investigate this point further, 6C ferrous heme nitrosyl model complexes that are stable *in solution at room temperature* are needed. This is challenging because the binding constants of N-donor ligands *trans* to NO are generally very small (K_{eq} ~ 1 to 30 M^{-1}) due to the σ-*trans* effect detailed above.[15c, 17] This is very different compared to CO and O_2 complexes where such a *trans* effect is lacking. Correspondingly, a recent report on Fe(II)-NO complexes of protoheme with covalently linked IM shows that these complexes are indeed only 5C in solution.[18] In fact, only one model complex is known so far where the covalently tethered N-donor ligand seems to remain bound to iron(II) after coordination of NO without the formation of 5C species in solution.[19] Systematic investigations to optimize axial ligand binding properties in tailed ferrous heme nitrosyl model systems are completely lacking. It is apparent from the literature that this issue has not been given enough consideration, in many cases, where it has been simply assumed that the tethering of an N-donor ligand will always lead to coordination with the central metal ion. In order to advance the general design of 6C Fe(II)-heme NO

model complexes without the undesirable necessity to add a large excess of the axial ligand (which is unfavorable for reactivity studies)[15c], a detailed evaluation of various tailed porphyrin designs is required. This study represents the first step towards a much needed systematic investigation into the binding properties of tethered N-donor ligands in 6C ferrous heme nitrosyls in solution at room temperature.

Results and Discussion

In order to investigate the formation of a 6C ferrous heme nitrosyl in solution according to the equation:

$$\mathbf{Fe^{II}(NO) + IM \rightarrow Fe^{II}(NO)(IM)} \quad \mathbf{(IM = imidazole)} \qquad \mathbf{(2)}$$

it is most important to perform room temperature measurements. This is because the binding of axial ligands is entropically favored at low temperature, due to the temperature dependent component of the Gibbs-Helmholtz equation. Methods of assessing the strength of the N-donor coordination to the heme center which require low temperatures are thus not a definitive means of determining the room temperature behavior of these systems. They can, however, still provide a means by which to compare different systems. In this study, we use room temperature UV-Vis and IR spectroscopy, coupled to low temperature EPR spectroscopy, to access the binding properties of our tethered N-donor ligands. In the case of UV-Vis spectroscopy, the Soret band maximum shows a direct correlation with the coordination number of the iron center. 5C heme nitrosyls show Soret band positions of about 405 nm. With IM present, the Soret maximum shifts to 426 nm and the complex is 6C. A corresponding, direct correlation is also observed between the N-O stretching mode v(N-O) and the coordination number: 5C complexes exhibit v(N-O) around 1675 – 1700 cm^{-1}, whereas in 6C species, v(N-O) drops to ~1630 cm^{-1} in the presence of IM. Additionally, low temperature EPR spectroscopy can be an effective probe of N-donor coordination to ferrous heme nitrosyls.[1] Species which are 5C in solution show g values of 2.10, 2.06, and 2.01 as well as a three line hyperfine splitting on g(min). On the other hand, 6C ferrous heme nitrosyls with axial N-donor coordination will exhibit smaller g values around 2.08, 2.00, and 1.97 as well as a distinctive nine line hyperfine splitting observed on g(mid). Since EPR spectroscopy requires low (at least liquid nitrogen) temperatures, which, as discussed above, entropically favors the coordination of the axial N-donor ligand, it can be expected that N-donor binding at room temperature will generally be somewhat weaker than determined from EPR.

Finally, Raman spectroscopy could potentially be applied to ferrous heme nitrosyls to characterize the strength of the Fe-NO bond via measurement of the ν(Fe-NO) stretch. However, photo-decomposition is a serious problem in this case when these complexes are exposed to the laser radiation required for Raman measurements.

In this study, 'tailed' porphyrins with covalently attached imidazole (IM) or pyridine (Py) ligands have been investigated with the specific aim of determining the requirements for the generation of truly 6C ferrous heme nitrosyl model complexes in solution at room temperature. These tailed porphyrins are preferred over the use of excess free IM, because they offer (a) control over the molar stoichiometry, (b) defined structures of the complexes, and (c) prevention of side reactions due to the presence of free axial ligand.[20] The first consideration involved in designing a 6C ferrous heme nitrosyl complex is the choice of the axial N-donor ligand. We started this investigation with a model complex based on H_2TMP (TMP =

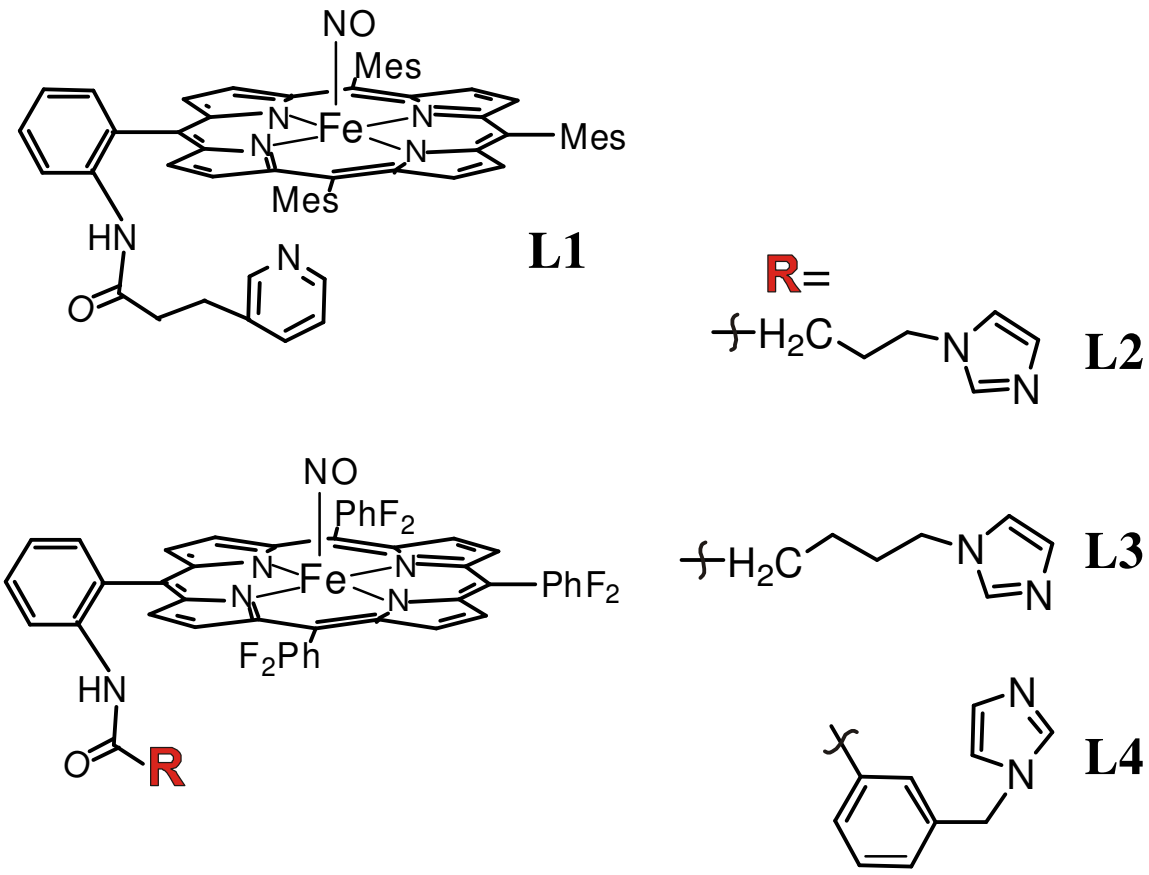

Figure 2.1. Drawings of the iron(II)-porphyrin NO complexes with covalently attached N-donor ligands employed in this study.

tetramesitylporphyrin) with a covalently attached Py (ligand **L1** in Figure 2.1). Reaction of the ferric precursor with NO gas in the presence of a small amount of methanol generates the corresponding ferrous heme nitrosyl complex.

However, the compound obtained, [Fe(TMP-*m*Py)(NO)] (**1**), forms only a 5C complex in solution, i.e. the Py does not bind to the Fe(II)-NO center. This is evident from the low-temperature (LT) EPR data of **1**, shown in Figure 2.3, where a characteristic 5C spectrum with g values of 2.10, 2.04, and 2.01 as well as a three line ^{14}N hyperfine pattern on the smallest g value, *g*(min) is observed.[1] The room temperature FT-IR spectrum of **1** exhibits ν(NO) at 1694 cm^{-1}, in agreement with values of other 5C complexes such as [Fe(TPP)NO] and [Fe(TMP)NO] at 1697 cm^{-1} and 1676 cm^{-1}, respectively.[21] Hence, the stereotype that simple attachment of an N-donor ligand to the porphyrin core should promote its coordination to the iron center is misleading. These results, however, agree with the very weak binding affinity of Py to Fe(II)-NO previously observed for different types of tetraphenylporphyrin ligands.[15c, 17b] In these studies it was found that binding constants of free pyridine are only in the range of 3 M^{-1} to 7 M^{-1} depending on the nature of the porphyrin ligand employed. During our axial ligation titration experiments reported in ref. [15c], we found that, in general, the binding constants for 1-methylimidazole (MI) are one order of magnitude larger (typically between 20-40 M^{-1}) than those seen for Py. Therefore, Py is not a suitable axial ligand for 6C ferrous heme nitrosyls and IM-type ligands are preferred due to their larger binding constants. However, even in the case of IM-type N-donors, the equilibrium between the 5C Fe(II)-NO complex and the 6C (IM)N-Fe(II)-NO adduct shown in equation 2 disfavors the formation of the 6C species. This is because the presence of 1 equivalent of an N-donor ligand with a typical binding constant (K_{eq}) < 50 M^{-1} will not lead to the formation of significant amounts of the 6C species in solution due to the equilibrium strongly favoring the reactant side.[22] In this case, the strong σ-*trans* effect of NO prevents binding of the axial ligand.[15c, 23] The formation of 6C Fe(II)-NO complexes in the absence of excess N-donor ligands thus presents a significant challenge.

Importantly, our previous studies have also shown that a further improvement of the axial ligand binding constant can be achieved by using the combination of a weakly electron-withdrawing tetra(*ortho*-difluorophenyl)-porphyrin ligand (H_2T*o*-F_2PP) and free imidazole. In this case, a dramatic increase of the IM binding constant to 2055 M^{-1} is observed.[15c] On the other hand, the application of the porphyrin H_2T*o*-F_2PP hardly affects the properties

of the Fe(II)-NO subunit as indicated by the ν(N-O) stretching mode, which is only 6 cm^{-1} lower in [Fe(T*o*-F_2PP)(MI)(NO)] compared to [Fe(TPP)(MI)(NO)].[15c] The binding constant of free MI to these fluorinated porphyrins therefore shows a nearly 300-fold increase over the pyridine derivative of the same system. In conclusion, the first requirements for the design of a truely 6C ferrous heme nitrosyl in solution are to (a) use IM as the N-donor ligand and (b) utilize *ortho* difluorophenyl substituted TPP or other slightly electron poor porphyrins. This provides a good basis in order to overcome the strong σ *trans* effect of NO and obtain a 6C complex in solution at room temperature in the presence of only one equivalent of the N-donor ligand. Based on these results, we decided to use IM ligands tethered to the fluorinated porphyrin T*o*-F_2PP for our further studies. In the next step, the linker arm which covalently links the N-donor ligand to the porphyrin core needs to be optimized.

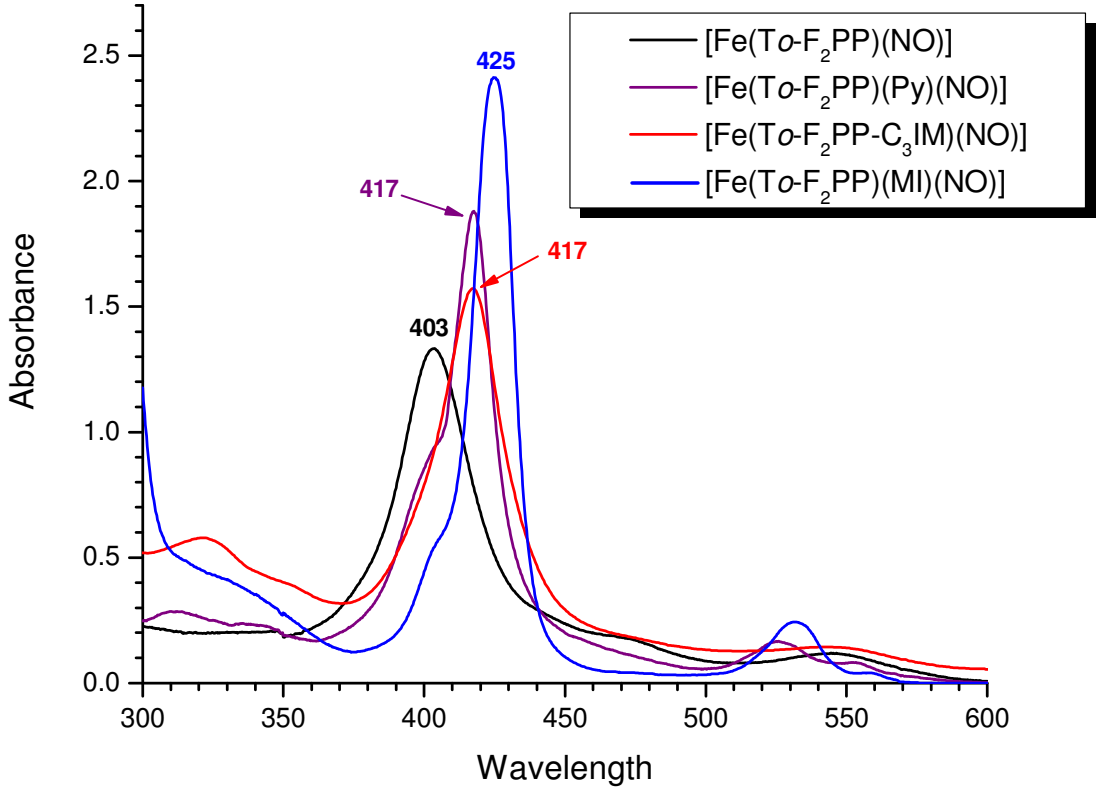

Figure 2.2. Electronic absorption spectrum of [Fe(T*o*-F_2PP-C_3IM)(NO)] (**2**, red) in comparison to 5C [Fe(T*o*-F_2PP)(NO)] (black), and the 6C complexes [Fe(T*o*-F_2PP)(MI)(NO)] (blue, MI = free 1-methylimidazole) and [Fe(T*o*-F_2PP)(Py)(NO)] (purple, Py = free pyridine). Spectra were recorded in CH_2Cl_2 or toluene solution at room temperature. No spectral shifts are observed between these solvents.

In light of the above mentioned results, we synthesized ligand **L2** in Figure 2.1 employing a C_3 alkyl chain-linked IM attached to a fluoro-substituted tetraphenylporphyrin. The UV-Vis spectrum of the obtained ferrous heme nitrosyl, [Fe(T*o*-F_2PP-C_3IM)(NO)] (**2**), exhibits the Soret band maximum at 417 nm as shown in Figure 2.2 (red curve). Interestingly, this is intermediate between the Soret position of the 5C complexes [Fe(TPP*)(NO)] (TPP* = tetraphenylporphyrin type ligand) at ~405 nm, and the IM coordinated (6C) species [Fe(TPP*)(IM)(NO)] at ~425 nm (cf. Figure 2.2). To test whether the 417 nm Soret band of **2** corresponds to weak binding of the axial ligand, we recorded the UV-Vis spectrum of the 6C Py complex [Fe(T*o*-F_2PP)(Py)(NO)] for comparison, because in this case, it is known that the Fe(II)-Py interaction is very weak.[15c, 23] As shown in Figure 2.2 (purple curve), the spectra of **2** and [Fe(T*o*-F_2PP)(Py)(NO)] show good agreement. Importantly, the lack of a shoulder between 400 - 407 nm and around 470 nm for **2** confirms that no (or very little) 5C species is present in solution. In addition to UV-Vis data, FT-IR spectroscopy can also be used to probe the coordination number of ferrous heme nitrosyls through the N-O stretching mode ν(N-O), as mentioned above. Interestingly, as elaborated below, the magnitude of the downshift of ν(N-O) is a direct function of the Fe-N(IM) bond strength, mediated by the *trans* interaction between the N-donor ligand and NO. The FT-IR spectrum of **2**, taken at room temperature in a KBr disk, shows a broad intense band at 1686 cm^{-1},

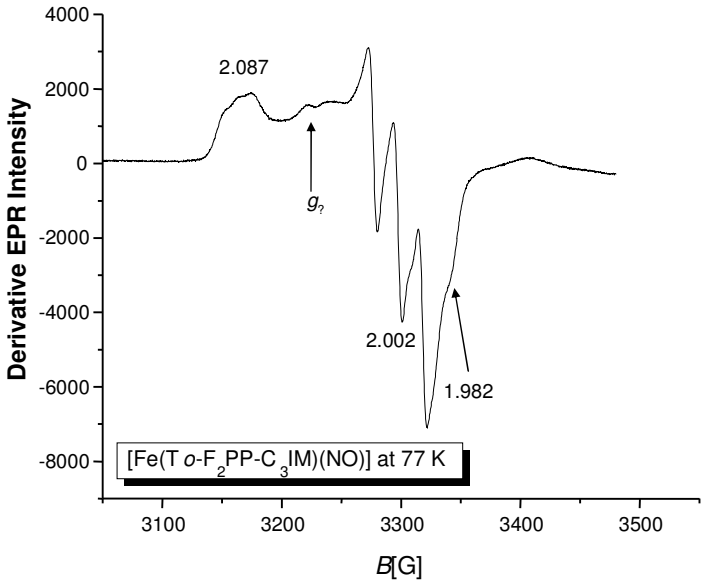

Figure 2.3. EPR spectrum of [Fe(T*o*-F_2PP-C_3IM)(NO)] showing partial binding of the alkyl-linked imidazole. Partial binding is evident from the broad distortions in the hyperfine splitting on g_{mid}.

which is assigned to the v(N-O) stretch. This energy of v(N-O) is not far off from values of known 5C complexes such as [Fe(TPP)NO] or [Fe(TMP)NO] (vide supra) and thus indicates a very weak covalent interaction between IM and the heme center.[15c]

More insight is available from EPR spectroscopy. The EPR spectrum of **2** (shown in Figure 2.3) clearly resemble the spectra of 6C complexes.[1] Hyperfine splittings observed within these spectra can reveal a great deal of information about the coordination environment of the central iron in heme nitrosyls and has traditionally been used to distinguish between 5C and 6C complexes.[1] This information manifests itself not only in the number of hyperfine lines observed, but also in the particular g value which exhibits the well-resolved hyperfine splittings. In the case of 5C ferrous heme nitrosyl complexes such as [Fe(TPP)(NO)], three g values are observed at 2.10, 2.06, and 2.01. The smallest of these, g(min), shows clear three line hyperfine splittings due to the interaction of the nuclear spin (I=1) of ^{14}N(O) with the unpaired electron of the Fe(II)-NO unit. The fact that the well-resolved hyperfine splittings are seen on g(min) indicates that the principle axis of this g-value is aligned closest to the Fe-N(O) axis.[1, 15d] For 6C complexes with NO and IM in the axial positions, the g shifts are smaller with g values of about 2.07, 2.00, and 1.97.[1] In addition, the three hyperfine lines are further split to give a nine line hyperfine pattern which is now observed on g(mid), due to a rotation of the g tensor.[1, 15d] The spectrum of **2** at 77 K (shown in Figure 2.3) exhibits strong ^{14}N hyperfine lines of NO on g(mid), and the *g* values are obtained at 2.09, 2.00, and 1.98. In the lq. helium spectrum additional, small, unresolved hyperfine splittings due to the axial IM ligand seem to be present on g(mid). The obtained g values and the presence of hyperfine splittings on g(mid) are generally indicative that **2** is a 6C complex in agreement with the UV-Vis result. However, the lack of clear nine-line hyperfine splittings of this signal indicates very weak binding of IM to iron as is also reflected by the large value of v(N-O). This is further supported by the small hyperfine coupling constant of the IM nitrogen estimated at around 2.0 MHz for **2** compared to 16-19 MHz for N-donor ligands in known 6C complexes.[24] EPR spectra are ideally suited for assessing the Fe-IM bond strength as the covalency of the Fe-IM bond directly correlates with the amount of spin density transfered from the Fe(II)-NO unit to the N-donor atom of IM.[15c] The spin density present on the IM nitrogen atom then correlates with the contact shift, and hence, the magnitude of the N(IM) hyperfine coupling

constant. In this sense, weak bonding results in minimal transfer of spin density between Fe and IM, resulting in almost no contact shift and a small hyperfine coupling constant, likely dominated by the dipolar contribution. A stronger Fe-IM bond will manifest itself in an increase in contact shift, leading to a larger hyperfine coupling constant, and thus a cleaner resolution of hyperfine lines on g(mid).

The EPR spectrum of **2** in Figure 2.2 also shows a fourth g value which is typically observed for 6C ferrous heme nitrosyl complexes in both proteins and model systems.[1] This signal is usually referred to as $g_?$ and is clearly identified in the case of both **2** and **3**. Interestingly, this additional signal seems to be absent in 5C heme nitrosyls. The origin of $g_?$ has been a matter of extended discussion in the literature.[25] It has been proposed that this signal arises from a second conformation of the complex where the relative orientation of NO, with respect to the IM plane, has shifted.[1] This is consistent with the observation that crystal structures of 6C model complexes usually show disorder of the NO ligand, giving rise to two major conformations.[15c, 23, 26] To rule out binding of the solvent DMSO in the case of **2** and **3**, the EPR spectrum of the 5C complex [Fe(TPP)(NO)] was recorded in a DMSO/toluene mixture (1:1). These data resemble more closely the typical 5C spectrum of this compound in pure toluene. Additionally, the UV-vis spectrum of [Fe(TPP)(NO)] in DMSO shows the Soret band at 409 nm, indicative of a 5C complex. Therefore, binding of DMSO to complex **2** can be ruled out in the EPR experiments. Based on all available spectroscopic results, it can be concluded that complex **2** is 6C in solution at room temperature, but that the interaction of the C_3 imidazole arm with the Fe(II)-NO center is weak.

There are two possible reasons for the weak binding of the C_3 imidazole linker in ligand **L2**: (a) the alkyl chain of the 'C_3' linker is too short to allow for a good interaction of IM with iron(II), or (b) the dynamic motion of the phenyl rings leads to a constant alkyl chain motion in solution, which prevents effective binding of the imidazole ligand to iron(II). In order to determine the influence of the alkyl chain length on the binding properties of the linked IM, we prepared a corresponding complex where the length of the alkyl chain is increased by one CH_2 unit (ligand **L3** in Figure 2.1). Importantly, the UV-Vis and EPR spectra of this complex, [Fe(T*o*-F_2PP-C_4IM)(NO)] (**3**), again show weak binding of the IM linker to the iron(II) center with a Soret maximum at 415 nm and EPR spectra similar to that shown in Figure 2.3. In particular, the absorption spectrum in Figure 2.4 is indicative of the

presence of a small amount of 5C complex in solution at room temperature, as evidenced by a very pronounced shoulder at 405 nm. This counter intuitive result shows that an increase of the alkyl chain length from 'C_3' to 'C_4' actually has a negative effect, i.e. *the increase in length or flexibility of the linker slightly decreases the binding constant of the tethered IM ligand to iron(II)*. This is most likely due to a loss of entropy of internal rotation as discussed before for tailed Zn-porphyrins.[27] Here, entropy loss was observed

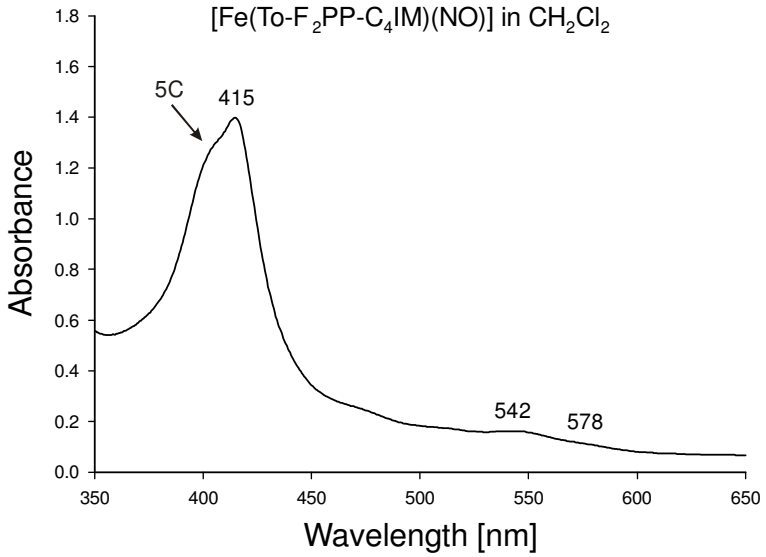

Figure 2.4. UV-Vis spectrum of [Fe(T*o*-F_2PP-C_4IM)(NO)] (**3**) in CH_2Cl_2 at room temperature. The indicated shoulder is indicative of a fraction of the 5C nitrosyl.

for each additional CH_2 unit added to the alkyl tethers within these systems. EPR spectra of complex **3** are in agreement with this conclusion and show g values at 2.07, 1.99, and 1.97, which are almost identical to those for **2**, indicating that an increase in tether length does not increase the Fe-IM covalency, and hence, bond strength. No 5C species is observed in the EPR spectra of **3**, but this is likely due to a slight increase in the IM binding constant at low temperature compared to the room temperature UV-Vis data (see Section A.1).

Our systematic studies on IM binding to ferrous heme nitrosyls presented above therefore show that pyridyl donors and C_3-IM or C_4-IM tethers (**L1** – **L3**) are poor designs for 6C ferrous heme nitrosyls in solution. Because of the poor binding seen for both **2** and **3**, it can be inferred that the length of the tether is not as important as its other structural properties.

Based on this result, we decided to explore whether a more rigid (less floppy) linker with a larger mass could change the dynamics of the linker

motion and facilitate a 6C complex. For this purpose, a benzyl group was incorporated into the linker, leading to ligand H_2To-F_2PP-BzIM (**L4**) in Figure 2.1. From the literature, work of Collman and coworkers has presented evidence that a similar linker could indeed allow for the formation of a 6C species in solution, although the room temperature characterization of the corresponding complex was incomplete.[19] Ligand **L4** was prepared and crystallographically characterized as the corresponding Zn complex. The crystal structure of this compound is shown in Figure 2.5. Crystallographic data and important

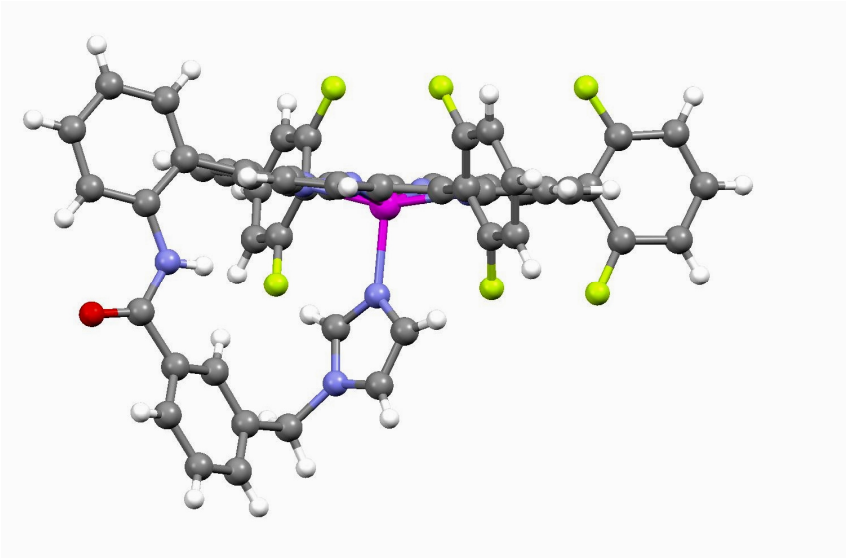

Figure 2.5. Molecular structure of [Zn(To-F_2PP-BzIM)] showing IM bound to Zn(II) where the Zn ion is displaced form the porphyrin plane by 0.5 Å. Two CH_2Cl_2 solvent molecules are present per unit cell and have been omitted, along with all hydrogen atoms, for clarity.

structural parameters are listed in Tables 2.1 and 2.2. The obtained bond distances and angles reveal very little strain within the tether. The only sizable perturbation from expected values is seen in the CNC angle of 129.1° for the amide linkage. This value is several degrees larger than expected for an idealized system but only slightly larger than amide CNC angles in other corresponding zinc porphyrin compounds. The zinc complex of α,α,α,α-Tetra-(2-[3,4-dimethoxyphenyl]-acetamidophenyl)porphyrin, for example, exhibits an amide CNC angle of 128°.[28] The zinc within the porphyrin center of the **L4** complex is clearly displaced towards the IM tether by about 0.5 Å from the porphyrin plane. The Zn-N(imidazole) bond distance is 2.079 Å. The average Zn-N(porphyrin) bond distance is 2.077 Å, which is slightly longer than the average bond length of 2.050 Å observed in four-coordinate [Zn(TPP)].[29] On the other hand, this value is in agreement with the 5C complexes [Zn(TPP)(3-APy)] (3-APy = 3-aminopyridine) and [Zn(OPP)(3-APy)] (OPP^{2-} = octaphenylporphyrin)

where average Zn-N(porphyrin) bond lengths of 2.080 Å and 2.075 Å have been determined, respectively.[30] The structure is well ordered with the single exception of the phenyl ring located opposite to the tether position. Two possible orientations are seen in the crystal structure where the phenyl ring

Table 2.1. Crystallographic data for compound [Zn(T*o*-F_2PP-BzIM)].

Empirical formula	$C_{56}H_{33}Cl_2F_6N_7OZn$
Formula weight (g/mol)	1070.16
T (K)	85
Space group	Triclinic, P-1
a (Å)	10.522
b (Å)	13.206
c (Å)	19.752
α (deg.)	103.955
β (deg.)	101.557
γ (deg.)	100.116
V ($Å^3$)	2536.1
Z	2
μ (mm^{-1})	0.659
λ (Å)	0.71073
Collected reflns	54977
Unique reflns	12597
R_{int}	0.0460
GOF	1.075
R1 [I>2σ(I)]	0.0570
wR2 (all data)	0.1770

Table 2.2. Selected crystallographic features of [Zn(T*o*-F_2PP-BzIM)]. All values are given in Å.

Zn1-N1 (porphyrin)	2.077
Zn1-N2 (porphyrin)	2.095
Zn1-N3 (porphyrin)	2.064
Zn1-N4 (porphyrin)	2.073
Zn1-N7 (axial IM)	2.079
Zn1 (displacement)	0.5

rotates slightly off the perpendicular geometry with respect to the porphyrin plane, in both possible directions. The porphyrin ligand itself shows very little distortion and appears only to be slightly domed towards the IM ligand. The UV-Vis adsorption data obtained for the complex [Zn(T*o*-F_2PP-BzIM)] show the Soret band at 427 nm. This is in agreement with know 5C Zn(II)-porphyrin complexes.[31] The analogous complex [Zn(T*o*-F_2PP-BzBr)], where IM has been

replaced by a non-coordinating bromine, shows typical UV-Vis absorption features of four-coordinate (4C) Zn(II)-porphyrin complexes where the Soret band is observed at 416 nm (cf. Figure 2.6). Due to these characteristic absorption features, zinc metallated porphyrin species can be a useful tool to determine the coordination environment of tethered porphyrin systems, and in particular, to probe for the presence and binding properties of an attached linker.

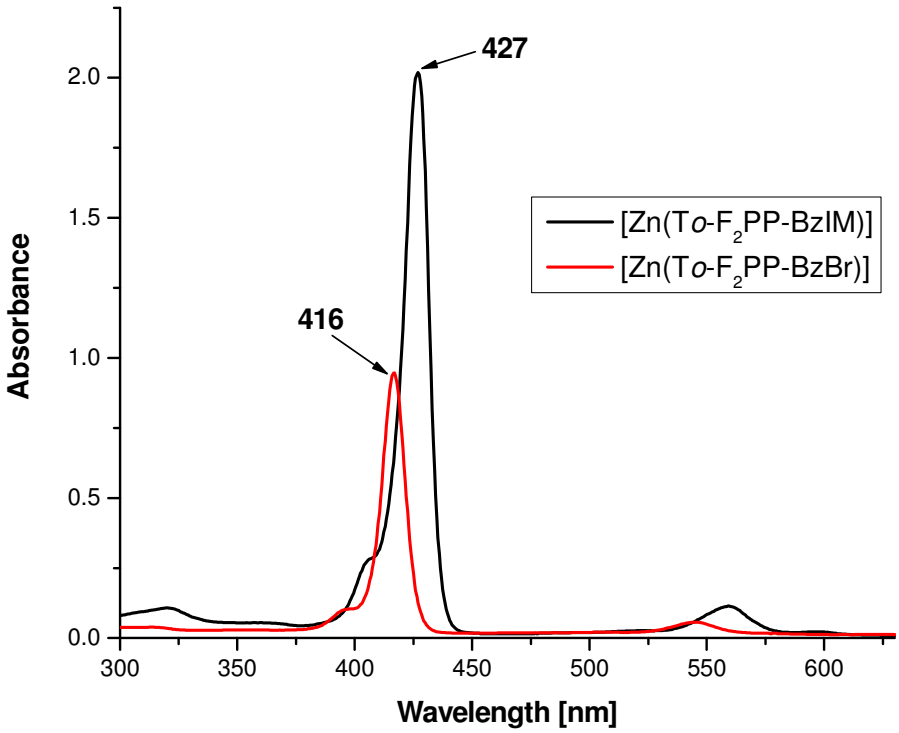

Figure 2.6. UV-Vis spectra of the zinc complexes [Zn(To-F_2PP-BzIM)] (black) and [Zn(To-F_2PP-BzBr)] (red). Typical Soret and Q band features in 5C zinc tetraphenylporphyrin complexes are seen at 427 nm and 559 nm, respectively, as found for the IM-bound complex. Upon replacement of IM with a non-coordinating bromine, the Soret and Q features shift to positions typically observed for 4C zinc complexes at 416 nm and 543 nm, respectively. This confirms the ability of the IM in ligands **L4** to coordinate to the central metal ion.

Next, the ferrous heme nitrosyl model complex **4** (shown in Scheme 2.1) was synthesized. Importantly, the iron(II)-NO complex exhibits the Soret band at 427 nm as shown in Figure 2.7 (red curve), which is indicative of the formation of a stable 6C adduct in solution. The spectral features compare well with those of the 6C complex [Fe(To-F_2PP)(MI)(NO)] (MI = free 1-methylimidazole), obtained in the presence of an excess of MI. In particular,

the lack of a shoulder around 410 nm, which is indicative of 5C species in solution, confirms the absence of any 5C complex for the benzyl-linked compound. To further investigate the strength of the Fe-IM interaction in **4**,

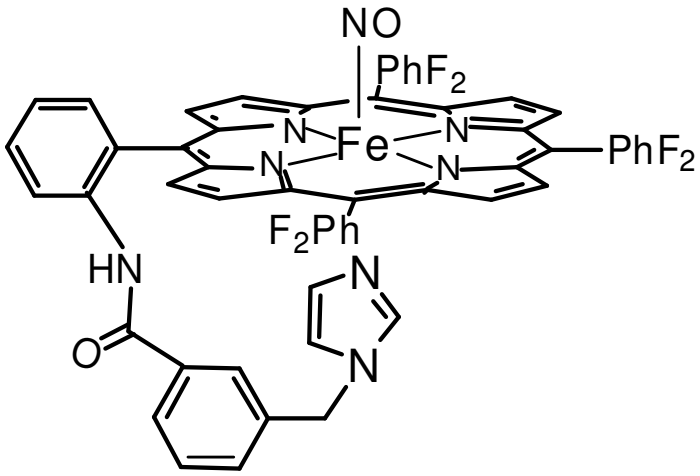

Scheme 2.1. Molecular structure of the 6C complex [Fe(T*o*-F_2PP-BzIM)(NO)] (**4**).

the EPR spectrum of this compound was recorded as shown in Figure 2.8. Both the observed g values of 2.08, 2.01, and 1.98, as well as the clean nine line hyperfine pattern on g(mid) with an IM-nitrogen hyperfine coupling constant of 19 MHz resemble those of well known 6C ferrous heme nitrosyls.[1] *These results confirm that **4** forms a stable 6C complex in solution where the interaction of the benzyl IM arm with the Fe(II)-NO center is strong*. Neither the UV-Vis data in Figure 2.7 nor the EPR spectrum indicate the presence of any 5C species in solution. To further quantify the strength of the Fe-IM interaction, solution FT-IR spectra were recorded at room temperature, since the strength of the N-O bond, represented by the N-O stretching frequency, is very sensitive to the strength of the Fe-IM interaction.[15] In 5C complexes of the type [Fe(porphyrin)(NO)], the N-O stretch ν(N-O) is observed at 1675 - 1700 cm^{-1} (1697 cm^{-1} for [Fe(TPP)(NO)]). The addition of free Py derivatives to [Fe(TPP)(NO)] results in weak coordination of the Py ligand and thus a moderate shift in the ν(N-O) frequency. In the case of [Fe(TPP)(4-NMe_2Py)(NO)] (4-NMe_2Py = 4-(dimethylamino)pyridine) the ν(N-O) frequency shifts down to 1653 cm^{-1} (recorded in the solid state).[23] On the other hand, upon coordination of free MI a substantial shift in the ν(N-O) stretching frequency to 1630 cm^{-1} (for [Fe(TPP)(MI)(NO)]) is observed. This indicates that binding of an N-donor ligand and donation into the d_{z^2} orbital of iron weakens the Fe-NO σ-bond, and, due to the reduced donation from a π^* orbital of NO, also weakens the N-O bond. Such an interpretation is in agreement with the experimentally observed

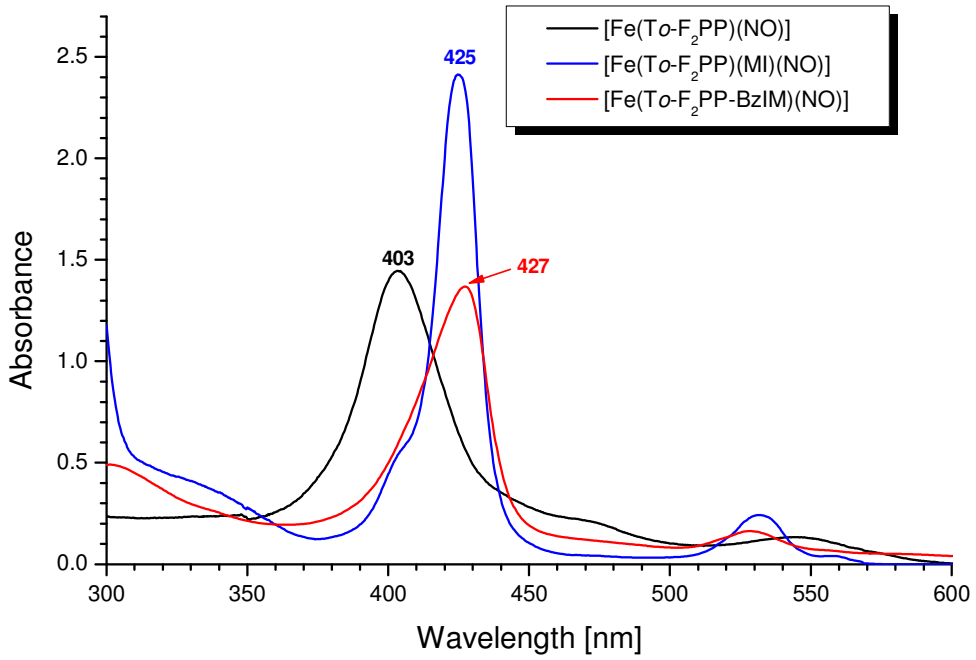

Figure 2.7. Electronic absorption spectra of [Fe(T*o*-F_2PP-BzIM)(NO)] (**4**, red), 5C [Fe(T*o*-F_2PP)(NO)] (black), and 6C [Fe(T*o*-F_2PP)(MI)(NO)] (MI = free 1-methylimidazole, blue).

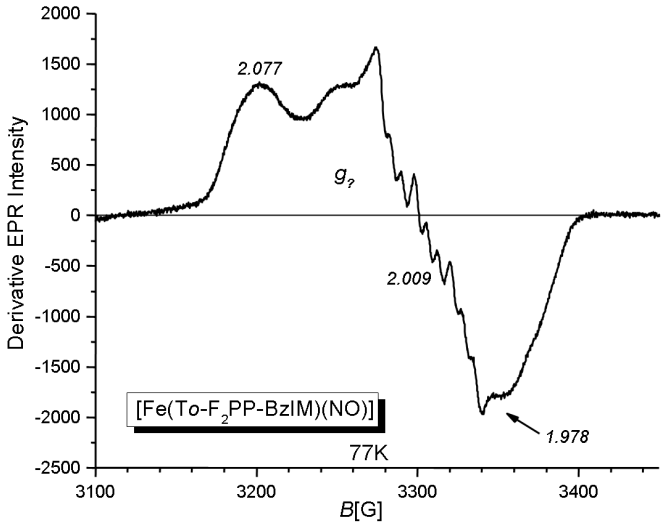

Figure 2.8. EPR spectrum of [Fe(T*o*-F_2PP-BzIM)(NO)] (**4**) in frozen DMSO at 77k (^{14}N hyperfine for g(mid) [MHz]: A(NO) = 62, A(IM) = 19). The additional signal $g_⊥$ is typically observed for 6C ferrous heme nitrosyls in both proteins and model complexes. See text for a detailed explanation and relevant references.

direct correlation of the Fe-NO and N-O bond strengths and vibrational frequencies where binding of the axial N-donor ligand in fact weakens both of these bonds.[15c, d, 23, 32] In this way, binding of an axial N-donor ligand lowers the N-O stretching frequency, giving rise to the observed inverse correlation between ν(N-O) and the Fe-N(N-donor) bond strength. In the case of complexes **1-4** presented here, the energy of ν(N-O) can also be seen to vary significantly based on the tether employed and the specific N-donor ligand used. The IR results in Table 2.3 show the range of ν(N-O) energies observed based on ligand choice. Importantly, the ν(N-O) stretching frequency of **4** is observed at 1644 cm^{-1} in solution at room temperature as shown in Figure 2.9, which further confirms that **4** corresponds to a 6C species even in solution. Interestingly, this frequency is somewhat higher in energy compared to [Fe(T*o*-F_2PP)(MI)(NO)] (1624 cm^{-1}) and [Fe(TPP)(MI)(NO)] (1630 cm^{-1}) with bound free MI. Therefore, the IR studies show that the covalently attached benzyl-IM linker still cannot bind as strongly to the Fe(II)-NO unit as free 1-methylimidazole (MI), but that **4** forms a stable 6C complex in solution at room temperature *without the requirement for the presence of excess axial ligand*. In this regard, the N-O stretching frequency also seems to be the most sensitive probe for the strength of the Fe-IM interaction.

Table 2.3. Properties of 5C and 6C ferrous heme model complexes.

Complex	Soret [nm]	ν(N-O) [cm^{-1}] [a]	EPR g values [b]
[Fe(TPP)(NO)][c]	405	1697	2.102/2.064/2.010(*)
[Fe(TPP)(MI)(NO)] [c]	425	1630	2.079/2.004(*)/1.972
[Fe(T*o*-F_2PP)(NO)] [c]	403	not det.	not det.
[Fe(T*o*-F_2PP)(MI)(NO)] [c]	425	1624	not det.
[Fe(TMP-*m*Py)(NO)] [d]	406	1694	2.099/2.040/2.012(*)
[Fe(T*o*-F_2PP-C_3Im)(NO)] [d]	417	~1686	2.087/2.002(*)/1.982
[Fe(T*o*-F_2PP-C_4Im)(NO)][d]	415	not det.	2.073/1.991(*)/1.971
[Fe(T*o*-F_2PP-BzIm)(NO)] [d]	427	1644(s)	2.077/2.009(*)/1.978
[Fe(TpivPP-IM)(NO)] [f]	415	1635(?)	2.072/2.002(*)/1.976

[a] Measured at room temperature in a KBr disk. Solution data are indicated by (s). [b] Measured at lq. nitrogen temperature. The asterisk indicates the g value that shows well resolved hyperfine lines in the spectrum. [c] Reference 15c,d. [d] This work. [f] Reference 34. The conditions for the IR measurements are not provided.

One problem that remains is whether **4** shows intramolecular binding of the tether as desired, or intermolecular coordination of the tether to a different complex, potentially forming dimers or large aggregates in solution. Such

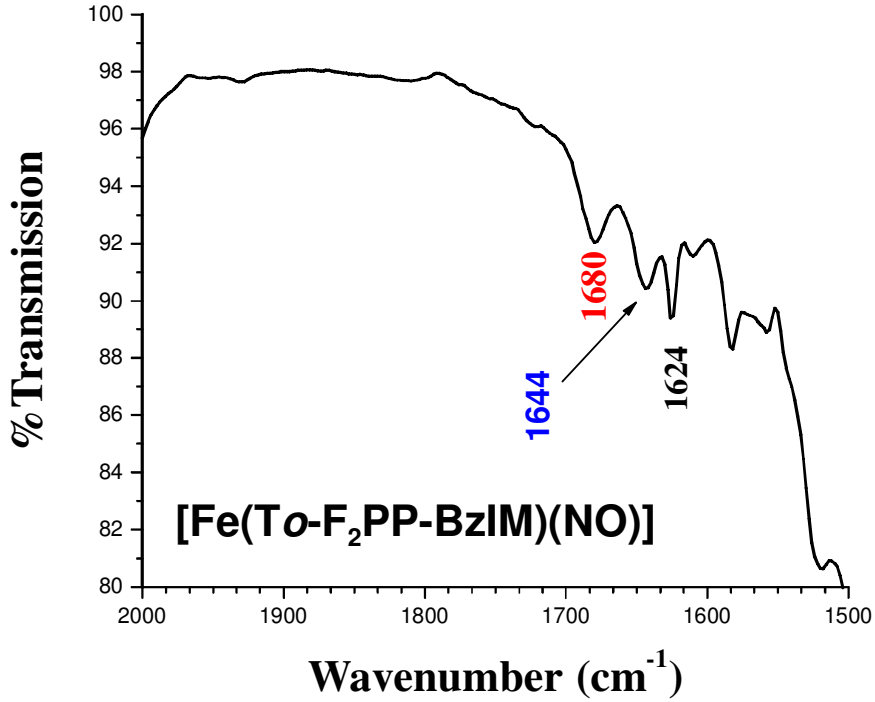

Figure 2.9. Solution IR spectrum of [Fe(T*o*-F_2PP-BzIM)(NO)] (**4**) showing the ν(N-O) stretching frequency at 1644 cm^{-1}. This value is slightly higher than that observed for [Fe(T*o*-F_2PP)(MI)(NO)] with free MI (1624 cm^{-1}).

intermolecular coordination has been previously suggested by Momenteau for heme protein analogues in which tethers were attached to the β-pyrrole positions of the porphyrin.[9] In this case, the linkers corresponded to floppy alkyl chains. Additionally, tethers at the β-pyrrole positions should be more susceptible to intermolecular coordination due to their orientation relative to the porphyrin plane. A tether employed at the *ortho*-phenyl position of a tetraphenylporphyrin derivative is oriented toward the heme center and thus is less likely to show intermolecular coordination due to the close proximity of the tethered N-donor ligand to the Fe center of the same complex. Increasing the rigidity of the tether will further hinder this undesirable coordination. The crystal structure of the zinc complex of **L4** presented above provides further evidence that intermolecular coordination is most likely not occurring in complex **4**. To further address this issue, UV-Vis dilution experiments were performed. The concentration of [Fe(T*o*-F_2PP-BzIM)(NO)] was systematically decreased until the spectra merged with the baseline, and the Soret position was determined for each concentration. As described above, the Soret band position is diagnostic for the coordination mode of the heme nitrosyl. In these experiments the Soret position remained constant. This result strongly

indicates that the tethered IM interacts with the iron center of the same complex. If intermolecular binding was occurring, lower concentrations should favor dissociation of the intermolecular complex and thus, a Soret shift would be observed upon concentration decrease.[9]

Our results presented above are also in agreement with recent findings of Collman and coworkers where a similarly rigid benzyl linker was used for the preparation of CcO and NorBC models, although the coordination number of the heme nitrosyls was not explicitly addressed.[12b, 19, 33] Nevertheless, room temperature UV-Vis data shown in their reports provide evidence that the similar benzyl linker, used in conjunction with a picket fence porphyrin, also generates a 6C ferrous heme nitrosyl complex in solution. Not suprisingly, low temperature data are also in agreement with this finding. While further room temperature characterization, in particular IR spectroscopy, of these compounds is lacking, the benzyl-linked complex does appear to fulfill all the necessary requirements to generate 6C ferrous heme nitrosyls in solution as defined in this work. Besides the presence of the benzyl-IM tether, the amide-substituted TPP derivative employed in this work provides the necessary, weakly electron-poor porphyrin ligand needed to enhance IM binding to the Fe-NO unit. Only one other example of a potentially 6C iron-porphyrin NO complex with a tethered axial IM ligand is known.[34] In this case, the alkyl chain linker is attached to the β-pyrrole carbon of a picket fence porphyrin. However, whereas the EPR spectrum of this complex clearly shows binding of the IM-linker to iron(II) at low temperature, the room temperature UV-Vis data exhibit the Soret band at 415 nm, which is more in agreement with the weak binding observed for **2** and **3**. A shoulder at 479 nm also indicates the presence of a distinct amount of 5C species at RT in solution. Finally, dilution experiments need to be performed in this case, since β-pyrrole tailed hemes tend to form intermolecular aggregates.[9]

Conclusions

As shown in this chapter, the design of a truly 6C ferrous heme nitrosyl complex in solution at room temperature depends on several factors. Application of a strongly binding ligand like IM, combined with a bulky benzyl linker, is crucial for the formation of these 6C complexes. In addition, a relatively electron poor porphyrin ligand seems to facilitate IM binding, and therefore, needs to be incorporated. This can be accomplished by the addition of either fluoro substituents or amide groups to the *meso* phenyl rings of a

tetraphenylporphyrin type ligand. These 6C model systems require a very specific design as compared to those employed for O_2 and CO binding studies because these diatomics do not show the strong σ-*trans* effect that is observed for NO. In this study it is demonstrated that a truly 6C ferrous heme nitrosyl can be generated in solution at room temperature in the presence of only one equivalent of the N-donor ligand, if all requirements specified above are fulfilled. The need for excess IM for the generation of 6C species, which leads to undesired side reactions including denitrosylation,[15c, 17a, 35] is now obsolete. Compound **4** is therefore ideally suited for reactivity studies on 6C Fe(II)-NO complexes which are currently in progress. In particular, the facile synthesis of **4** will be advantageous for application of this complex in NorBC model studies. Complex **4** is easy to prepare at relatively high total yields (2.5%) for a sophisticated porphyrin.

Interestingly, the strength of the Fe-(N-donor) bond in the benzyl-linked complex **4** is still slightly weaker than that observed for [Fe(T*o*-F_2PP)(MI)(NO)] with free MI, as evidenced by the higher ν(N-O) stretching frequency. Further studies should therefore be directed at forming even stronger Fe-(N-donor) bonds in 6C complexes as well as investigating other tethers which could potentially facilitate the formation of truly 6C ferrous heme nitrosyls in solution. This knowledge will allow for the improved synthesis of NorBC model complexes which can more effectively mimic the structure and function of the active site of this enzyme.

Experimental

In general, reactions were performed applying inert Schlenk techniques. Preparation and handling of air sensitive materials was carried out under an argon atmosphere in an MBraun glovebox equipped with a circulating purifier (O_2, H_2O < 0.1 ppm). Infrared spectra were obtained from KBr disks or in chloroform solution on a Perkin-Elmer BX spectrometer. Proton magnetic resonance spectra were recorded on a Varian Inova 400 MHz and a Varian Mercury 300 MHz instrument. Electronic absorption spectra were measured using an Analytical Jena Specord 600 instrument. MALDI-TOF mass spectra were obtained on a Micromass TofSpec-2E mass spectrometer whereas LCT-ESI mass specta were obtained on Micromass LCT Time-of-Flight mass spectrometer. Electron paramagnetic resonance spectra were recorded on a Bruker X-band EMX spectrometer equipped with an Oxford Instruments liquid nitrogen or liquid helium cryostat. EPR spectra were typically obtained on frozen solutions using

~20 mW microwave power and 100 kHz field modulation with the amplitude set to 1 G. Sample concentrations employed were ~1 mM.

Crystal structure determination was carried out using a Bruker SMART APEX CCD-based X-ray diffractometer equipped with a low temperature device and a fine focus Mo-target X-ray tube (wavelength = 0.71073 Å) operated at 1500 W power (50 kV, 30 mA). Measurements were taken at 85 K and the detector was placed 5.055 cm from the crystal. The data was processed with SADABS and corrected for absorption. The structure was solved and refined with the Bruker SHELXTL (ver. 2008/3) software package (cf. Table 2.1).[36]

Materials

All solvents and reagents were purchased and used as supplied except as follows. Toluene was distilled from sodium under argon. Dried and air free THF and n-hexane were obtained after passing through an MBraun solvent purification system. 1-Methylimidazole was vacuum distilled from KOH and degassed via five freeze-pump-thaw cycles. Nitric oxide (Airgas, USA) was purified by first passing through an ascarite II column (NaOH on silica gel) and then through a cold trap at –80°C to exclude higher nitrogen oxide impurities. The free base porphyrin ligands H_2TMP-*m*Py and H_2T*o*-F_2PP-C_3IM (ligands **L1** and **L2**, respectively) were synthesized following reported procedures[12e, 37] with some modifications as described in the following. The precursor porphyrins 5,10,15-Tris-(2,4,6-trimethyl-phenyl)-20-(2-amino-phenyl)-porphyrin [$H_2(NH_2)$TMPP] and 5,10,15-Tris-(2,6-difluoro-phenyl)-20-(2-amino-phenyl)-porphyrin [$H_2F_6(NH_2)$TPP] were prepared using reported procedures.[37a]

H_2TMP*m*-Py (ligand L1). The aminoporphyrin $H_2(NH_2)$TMPP (0.25 g, 0.33 mmol) was dissolved in 6 mL of DMF. To this, 1 mL of *N*,*N*-diethylaniline was added, followed by the addition of a solution of 3-(3'-pyridyl)propionic acid chloride in 3mL of DMF [prepared in situ by reacting 0.2 g of 3-(3'-pyridyl)propionic acid with 3 mL of $SOCl_2$], and then stirred for 4 hours at room temperature. The excess $SOCl_2$ and the solvent were removed under vacuum. The residue obtained was dissolved in CH_2Cl_2 and washed several times with deionized water. The solution was then dried with Na_2SO_4 and the solvent was removed using a rotary evaporator. The desired product was purified using column chromatography (silica, CH_2Cl_2/CH_3OH = 99:1). Yield: 0.20 g, 68 %
UV-Vis [nm] in CH_2Cl_2: 418, 514, 545, 590 and 646.

^{1}H NMR (400MHz, $CDCl_3$): 8.69-8.64 (m, 9H, β-pyrrole (8H) and aminophenyl(1H)); 8.13 (m, 1H, pyridyl); 8.0-7.97 (m, 2H, pyridyl); 7.8 (m, 1H, aminophenyl); 7.48 (m, 1H, pyridyl); 7.26 (s, 6H, mesitylphenyl); 6.9 (m, 1H, aminophenyl); 6.85 (s, 1H, NH-C=O); 6.78 (m, 1H, aminophenyl); 2.61 (s, 6H, *para* $-CH_3$); 2.47 (t, 2H, $-CH_2$-Pyridly); 1.84-1.80 (m, 18H, *ortho* $-CH_3$); 1.61 (t, 2H, -**CH_2**-CH_2-Pyridyl); -2.55 (s, 2H, NH pyrrole). MS (MALDI) for $C_{61}H_{56}N_6O$: Calculated: 889, found: 889.

Further control experiment: The column purified ligand **L1** was reacted with $Zn(OAc)_2 \cdot 2H_2O$ to yield [Zn(TMP-*m*Py)] in CH_2Cl_2/CH_3OH solution. After shaking with H_2O to remove the unreacted $Zn(OAc)_2$, the solvent was removed under reduced pressure and UV-Vis spectra were recorded. The UV-Vis spectrum of the product in CH_2Cl_2 shows the Soret band at 430 nm, which corresponds to a five-coordinate Zinc(II)-porphyrin complex.[31] This further proves the presences of the pyridyl linker in ligand **L1**.

[Fe(TMP-*m*Py)(Cl)]. 0.15 g (0.17 mmol) of H_2TMP-*m*Py (**L1**) was stirred in 10 mL of dry and air free THF. Anhydrous $FeCl_2$ (0.21 g, 1.7 mmol) was then added and the resulting reaction mixture was refluxed at 60 °C under an argon atmosphere for 1 hour. The reaction was then stopped and the solvent was removed under reduced pressure. The obtained residue was chromatographed on silica gel using 0.5% methanol in CH_2Cl_2. The metallated porphyrin fraction was collected and the solvent was then removed using a rotary evaporator. The obtained product was dried; yield: 0.11 g, 66 %. UV-Vis [nm] in CH_2Cl_2: 376, 418, 509, 576, 655 and 692. ^{1}H NMR ($CDCl_3$, 400 MHz): 80 (m, 8H, β-pyrrole).

[Fe(TMP-*m*Py)(NO)] (1). 0.05 g (0.05 mmol) of [Fe(TMP-*m*Py)(Cl)] were placed in a 100 mL Schlenk flask and freshly distilled $CHCl_3$ (8 mL) and CH_3OH (0.5 mL) were added. NO gas was then passed through this solution, and the resulting solution was stirred for one hour. *n*- hexane (10 mL) was slowly added to the reaction mixture, which was then stored in a freezer (-22°C) for 3 days. The resulting precipitate was filtered off using a fine pore Schlenk filter funnel. The yield of the product obtain was very low, 11 mg (22 %), and contained some impurities. FT-IR [cm^{-1}]: ν(NO) = 1694.

H_2T*o*-F_2PP-C_3IM (ligand L2). 4-(*N*-imidazolyl)butyric acid hydrobromide[37a] (0.18 g, 0.4 mmol) was ground to a fine powder and stirred in 5 mL of dry and air free CH_2Cl_2. The solution was brought to reflux under argon and 35 mg (0.3 mmol) $SOCl_2$ was then added. The solution was stirred at reflux under an argon atmosphere. After 30 minutes, the excess $SOCl_2$ and CH_2Cl_2 were removed under vacuum and a solution of $H_2F_6(NH_2)$TPP (0.1 g, 0.135 mmol) in 5 mL of CH_2Cl_2 was

added and the resulting green solution was stirred for 1 hour under argon at room temperature. The reaction was then stopped by pouring the solution into 20 mL of CH_2Cl_2 and successive washing with 2 x 20 mL of Na_2CO_3, and 3 x 20 mL of water, and then drying over Na_2SO_4. The solvent was removed under reduced pressure and the residue obtained was column purified on silica gel (CH_2Cl_2/CH_3OH= 95:5) to give the desired C_3 imidazole linked porphyrin ligand H_2T*o*-F_2PP-C_3IM. Yield: 0.045 g, 38 %.

^{1}H NMR (300 MHz, *d*-acetone): 9.15-8.80 (m, 8H, β-pyrrole); 8.55 (d, 1H, aminophenyl); 8.44 (s, 1H, amide); 8.11 (dd, 1H, aminophenyl); 8.05-7.95 (m, 3H, *para* fluorophenyl); 7.86 (t, 1H, aminophenyl); 7.65-7.45 (m, 7H, *meta* fluorophenyl (6H) and aminophenyl (1H)); 7.02 (s, 1H, imidazole); 6.44 (s, 1H, imidazole); 6.42 (s, 1H, imidazole); 3.45 (t, 2H, C_3H_6 tether); 1.58 (t, 2H, C_3H_6 tether); 0.90 (m, 2H, C_3H_6 tether); -2.69 (s, 2H, pyrrole NH).

UV-Vis [nm] in CH_2Cl_2: 415, 509, 543, 587, and 642. MS (LCT-ESI) for $C_{51}H_{33}N_7F_6O$: Calculated: 873.8, found: 874.

Further control experiment: the column purified ligand **L2** was reacted with $Zn(OAc)_2 \cdot 2H_2O$ to yield [Zn(T*o*-F_2PP-C_3IM)] in a CH_2Cl_2/CH_3OH solution. After shaking with H_2O to remove the unreacted $Zn(OAc)_2$, the solvent was removed under reduced pressure and UV-Vis spectra were recorded. The UV-Vis spectrum of the product in CH_2Cl_2 shows the Soret band at 427 nm, which is in accordance with similar values observed for five-coordinate Zinc(II)-porphyrin complexes[31] (substituted tetraphenylporphyrins with electron withdrawing or donating groups attached to the phenyl rings). This further proves the presence of the imidazolyl linker in ligand **L2**.

MS (LCT-ESI) for $ZnC_{51}H_{31}N_7F_6O$: Calculated: 935.1, found: 936.1. ^{1}H NMR spectra of the zinc metallated complex [Zn(T*o*-F_2PP-C_3IM)] reveal a shift of the imidazole proton peaks into the porphyrin aromatic region. This is most likely due to an exposure of the imidazole unit to the aromatic porphyrin ring current upon binding to the zinc center.

[Fe(T*o*-F_2PP-C_3IM)(Cl)]. 0.03 g (0.034 mmol) of H_2T*o*-F_2PP-C_3Im were stirred in 8 mL of dry and air free THF. Anhydrous $FeCl_2$ (0.043g, 0.34 mmol) was then added and the resulting reaction mixture was refluxed under an argon atmosphere for 1 hour. The reaction was then stopped and the solvent was removed under reduced pressure. The obtained residue was chromatographed on silica gel using 3% methanol in CH_2Cl_2. The metallated porphyrin fraction was collected, and the solvent was then removed using a rotary evaporator. Yield: 0.023 g, 70 %.

UV-Vis [nm] in CH_2Cl_2: 350, 415, 510, 557, and 642. FT-IR in KBr [cm^{-1}]: $\nu_{C=O}$ = 1700.

[Fe(T*o*-F_2PP-C_3IM)(NO)] (2). To a solution of [Fe(T*o*-F_2PP-C_3IM)(Cl)] (0.02 g, 0.02 mmol) in 10 mL of freshly distilled $CHCl_3$ and 0.5 mL of CH_3OH, excess nitric oxide was added and the resulting solution was stirred for one hour. *n*-hexane (15 mL) was slowly added to the reaction mixture, which was then stored in a freezer (-20°C) for 1 day. The resulting precipitate was filtered off and the obtained compound was stored inside a glove box. The IR spectrum shows the NO stretching band at 1686 cm^{-1}, indicative of the formation of **2**.

Yield: 0.010 g, 52 %: FT-IR in KBr [cm^{-1}]: ν(NO) = 1686.

In order to test whether complex **2** is really a monomer, we performed dilution experiments where the concentration was lowered to an intensity of 0.2 absorbance units. No shift of the Soret band was observed, indicating that the complex does not correspond to a dimer (oligomer) where two complexes (or more) share linkers.

N-(3-methoxycarbonyl)benzylimidazole. Imidazole (3.8g, 55.8 mmol) and methyl 3-bromomethyl-benzoate (3.1g, 13.5 mmol) were combined in 4 mL of DMF. The resulting faint yellow solution was stirred at room temperature for 20 hours. Upon completion, the reaction was diluted with 60 mL of water and extracted 3x with a total of 120 mL CH_2Cl_2. The organic layer was collected and extracted 3x with a total of 150 mL of a 10% HCl solution. The acidic solution was then alkalized with triethylamine to pH = 10, extracted 3x with a total of 210 mL ethyl acetate followed by drying over Na_2SO_4. Rotary evaporation of the solvent yielded a faint yellow oil in quantitative amounts. ^{1}H NMR (300 MHz, $CDCl_3$): 7.99 (d, 1H), 7.88 (s, 1H), 7.56 (s, 1H), 7.41 (t, 1H), 7.32 (d, 1H), 7.01 (s, 1H), 6.89 (s, 1H), 5.16 (s, 2H), 3.91 (s, 3H)

α-imidazolyl-*m*-toluic acid hydrochloride. N-(3-methoxycarbonyl)benzylimidazole (3.0g, 13.9 mmol) was dissolved in 27 mL of conc. HCl and brought to reflux while stirring for 2 hours. The HCl was then removed on a vacuum line and the resulting off-white solid was dried under vacuum overnight. The next day, the product was washed with hot acetonitrile and filtered to remove a yellow colored impurity. The resulting white solid was again dried under vacuum. Yield: 2.0g, 61%. ^{1}H NMR (300 MHz, CD_3OD): 9.13 (s, 1H), 8.06 (s, 1H), 8.05 (s, 1H), 7.66 (d, 1H), 7.60 (s, 1H), 7.57 (m, 2H), 5.56 (s, 2H)

H_2T*o*-F_2PP-BzIM (ligand L4) (Adapted from reference [38]). *α*-imidazolyl-*m*-toluic acid hydrochloride (0.1 g, 0.42 mmol) and an excess thionyl chloride (0.1 mL, freshly distilled under Ar) in methylene chloride (2 mL) were refluxed under

an argon atmosphere. After 1 hour the solution became clear. The excess $SOCl_2$ and CH_2Cl_2 were removed in vacuo to yield crude □-imidazolyl-*m*-toluic acid chloride as an off-white solid. In a separate flask, a solution of the porphyrin $H_2F_6(NH_2)TPP$ (0.088 g, 0.119 mmol) in 15 mL dry and air-free CH_2Cl_2 was stirred. To this stirred solution a suspension of □-imidazolyl-*m*-toluic acid chloride (from above) in CH_2Cl_2 (4 mL) was slowly added in small portions under an argon atmosphere at room temperature (color changed to green). The reaction was monitored by TLC (silica, CH_2Cl_2) until the only visible porphyrin remained at the baseline. The solution was diluted with 100 mL CH_2Cl_2 and shaken with 40 mL saturated $NaHCO_3$, washed 3x with 50 mL water, and dried with sodium sulfate. Rotary evaporation of the solvent yielded a purple solid. The product was purified on silica gel using column chromatography with 5% MeOH in CH_2Cl_2 as eluent. Yield: 100 mg, 92%.

UV-Vis [nm] in CH_2Cl_2: 416, 509, 542, 586 and 640. ^{1}H NMR (300MHz, CD_2Cl_2): 9.0-9.85 (m, 9H, □-pyrrole (8H) and aminophenyl (1H)); 8.22 (dd, 1H, benzyl); 7.95-7.80 (m, 4H, *para* fluorophenyl (3H) and aminopheyl (1H)); 7.65 (m, 1H, aminophenyl); 7.50-7.37 (m, 8H, *meta* fluorophenyl (6H) and benzyl (2H)); 6.78 (s, 1H, NH-C=O); 6.47-6.38 (m, 2H, benzyl (1H) and aminophenyl (1H)); 6.33 (m, 1H, imidazolyl); 6.19 (s, 1H, imidazolyl); 6.07 (d, 6H, imidazolyl); 3.88 (s, 2H, -CH_2-benzyl); -2.75 (s, 2H, NH pyrrole). MS (MALDI) for $C_{54}H_{34}N_7F_6O$; Calculated: 922, found: 922.

[Fe(T*o*-F_2PP-BzIM)(Cl)]. 0.03 g of H_2T*o*-F_2PP-BzIM were stirred in 10 mL of dry and air free THF. Anhydrous $FeCl_2$ (0.039g) was then added, and the resulting reaction mixture was refluxed under an argon atmosphere for 1 hour. The reaction was then stopped and the solvent was removed under reduced pressure. The obtained residue was chromatographed on silica gel using 5% methanol in CH_2Cl_2. The metallated porphyrin fraction (slowest moving) was collected, and the solvent was removed using a rotary evaporator. The product obtained was finally dried. Yield: 27 mg, 82%. UV-Vis [nm] in CH_2Cl_2: 337, 413, 577, and 650. FT-IR in KBr [cm^{-1}]: $\nu_{C=O}$ = 1684. MS (LCT-ESI) calculated: 975 (M-Cl), found: 975.

[Zn(T*o*-F_2PP-BzBr)]. The same procedure as for [Zn(T*o*-F_2PP-BzIM)] was used except that T*o*-F_2PP-BzBr was synthesized with an acid chloride made from $SOCl_2$ and methyl 3-bromomethyl-benzoate to yield T*o*-F_2PP-BzBr where the imidazole is lacking to prevent binding of the linker to zinc. UV-vis (nm) in CH_2Cl_2: 416, 510, 543, 585

[Zn(T*o*-F_2PP-BzIM)]. 0.026 g of H_2T*o*-F_2PP-BzIM were stirred in 10 mL of dry and air free CH_2Cl_2. $Zn(OAc)_2$ dihydrate (0.250 g) was then added along with 1 mL MeOH, and the resulting reaction mixture was stirred at room temperature for 1.5 hours. The color of the solution changed from deep red to magenta. The reaction was washed 3x with water, and dried with sodium sulfate. Rotary evaporation of the solvent yielded a magenta colored solid. Purification on a silica column eluted with CH_2Cl_2 yielded a pure magenta solid (23.8 mg, 84%). UV-Vis (nm) in CH_2Cl_2: 427, 559, 598

Further control for IM binding: The UV-Vis spectrum of the product in CH_2Cl_2 shows the Soret band at 427 nm, which is in accordance with similar values observed for five-coordinate Zinc(II)-porphyrin complexes.[31] In comparison, the analogous complex [Zn(T*o*-F_2PP-BzBr)] which lacks the IM ligand shows the Soret band at 416 nm. See Section A.4.

Crystalization of [Zn(T*o*-F_2PP-BzIM)]. [Zn(T*o*-F_2PP-BzIM)] (18mg) was disolved in 2 mL of 10% chlorobenzene in CH_2Cl_2 in a Schlenk tube which was cooled to 4°C. This tube was then connected via glass joints to a Schlenk flask with *n*-hexane stirred at 35°C. After four days in the dark, enough n-hexane had diffused over to obtain crystals suitable for crystallographic analysis.

[Fe(T*o*-F_2PP-BzIM)(NO)] (4). To a solution of the iron(III)-porphyrin, [Fe(T*o*-F_2PP-BzIM)(Cl)] (0.02 g, 0.02 mmol) in 10 mL of freshly distilled $CHCl_3$ and CH_3OH (0.5 mL), excess nitric oxide was added, and the resulting solution was stirred for one hour under an NO atmosphere. *n*- hexane (15 mL) was slowly added to the reaction mixture, which was then stored in a freezer (-20 °C) for 1 day. The resulting precipitate was filtered off using a fine pore Schlenk filter funnel, and the obtained compound was stored inside a glove box. The IR spectrum shows the NO stretching band at 1644 cm^{-1}, indicative of the formation of **4**. Yield: 14 mg, 70 %.

H_2T*o*-F_2PP-C_4IM (L3), [Fe(T*o*-F_2PP-C_4IM)(Cl)], and [Fe(T*o*-F_2PP-C_4IM)(NO)] (3).
The preparation of H_2T*o*-F_2PP-C_4IM was performed by the same method as described for H_2T*o*-F_2PP-BzIM, but using 5-bromopentanoic acid in place of □-bromotoluic acid to build the alkyl chain. ^{1}H NMR (300 MHz, *d*-acetone): 9.10-8.80 (m, 8H, β-pyrrole); 8.54 (d, 1H, aminophenyl); 8.41 (s, 1H, amide); 8.09 (dd, 1H, aminophenyl); 8.05-7.90 (m, 3H, *para* fluorophenyl); 7.86 (t, 1H, aminophenyl); 7.65-7.45 (m, 7H, *meta* fluorophenyl (6H) and aminophenyl (1H)); 7.04 (s, 1H, imidazole); 6.52 (s, 1H, imidazole); 6.44 (s, 1H, imidazole); 3.30 (t, 2H, C_4H_8 tether); 1.44 (t, 2H, C_4H_8 tether); 1.08 (m, 2H, C_4H_8 tether); 0.90 (m, 2H, C_4H_8 tether); -2.72 (s, 2H, pyrrole NH). UV-Vis [nm] in CH_2Cl_2: 414, 510, 541, 586,

and 641. MS (LCT-ESI) for $C_{52}H_{35}N_7F_6O$: Calculated: 887.9, found: 888.

Iron insertion into H_2To-F_2PP-C_4IM and the synthesis of [Fe(T*o*-F_2PP-C_4IM)(NO)] (**3**) also followed the same procedures as described for **4**.

[Fe(T*o*-F_2PP-C_4IM)(Cl)]: UV-Vis [nm] in CH_2Cl_2: 342, 414, 503, 574, and 650. FT-IR in KBr [cm^{-1}]: $\nu_{C=O}$ = 1719.

References

(1) Ghosh, A., *The Smallest Biomolecules: Diatomics and their Interactions with Heme Proteins*. Elsevier: Amsterdam, 2008.

(2) (a) Garbers, D. L.; Lowe, D. G., *J. Biol. Chem.* **1996,** *269*; (b) Hersleth, H. P.; Varnier, A.; Harbitz, E.; Rohr, A. K.; Schmidt, P. P.; Sorlie, M.; Cederkvist, F. H.; Marchal, S.; Gorren, A. C. F.; Mayer, B.; Uchida, T.; Schunemann, V.; Kitagawa, T.; Trautwein, A. X.; Shimizu, T.; Lange, R.; Gorbitz, C. H.; Anderson, K. K., *Inorg. Chim. Acta* **2008,** *361*; (c) Riggs, A. F., *Curr. Opin. Struct. Biol.* **1991,** *1*; (d) Waldman, S. A.; Murad, F., *Pharmacol.* **1987,** *39*.

(3) Moenne-Loccoz, P.; De Vries, S., *J. Am. Chem. Soc.* **1998,** *120*, 5147.

(4) (a) Collman, J. P.; Boulatov, R.; Sunderland, C. J.; Fu, L., *Chem. Rev.* **2004,** *104*; (b) Kim, E.; Chufan, E. E.; Kamaraj, K.; Karlin, K. D., *Chem. Rev.* **2004,** *104*; (c) Traylor, T. G., *Acc. Chem. Res.* **1981,** *14*; (d) Walker, F. A.; Simonis, U., Iron Porphyrin Chemistry. In *Encyclopedia of Inorganic Chemistry, Second Edition*, King, R. B., Ed. John Wiley & Sons, Ltd.: Chichester, 2005; Vol. IV, p 2390.

(5) Traylor, T. G.; Diekmann, H.; Chang, C. K., *J. Am. Chem. Soc.* **1971,** *93*.

(6) (a) Chang, C. K.; Traylor, T. G., *Proc. Natl. Acad. Sci. U.S.A.* **1973,** *70*; (b) Chang, C. K.; Traylor, T. G., *J. Am. Chem. Soc.* **1973,** *95*; (c) Traylor, T. G.; Chang, C. K.; Geibel, J.; Berzinis, A.; Mincey, T.; Cannon, J., *J. Am. Chem. Soc.* **1979,** *101*; (d) Traylor, T. G., *Pure & Appl. Chem.* **1991,** *63*.

(7) Schwarz, F. P.; Gouternam, M.; Muljiani, Z.; Dolphin, D. H., *Bioinorg. Chem.* **1972,** *2*.

(8) Paine III, J. B.; Dolphin, D. H., *Can. J. Chem.* **1978,** *56*.

(9) Momenteau, M.; Rougee, M.; Loock, B., *Eur. J. Biochem.* **1976,** *71*.

(10) (a) Collman, J. P.; Gagne, R. R.; Halbert, T. R.; Marchon, J. C.; Redd, C. A., *J. Am. Chem. Soc.* **1973,** *95*; (b) Collman, J. P.; Gagne, R. R.; Reed, C. A., *J. Am. Chem. Soc.* **1974,** *96*; (c) Gerothanassis, I. P.; Momenteau, M.; Barrie, P. J.; Kalodimos, C. G.; Hawkes, G. E., *Inorg. Chem.* **1996,** *35*.

(11) (a) Safo, M. K.; Gupta, G. P.; Walker, F. A.; Scheidt, W. R., *J. Am. Chem. Soc.* **1991,** *113*; (b) Walker, F. A.; Reis, D.; Balke, V. L., *J. Am. Chem. Soc.* **1984,** *106*.

(12) (a) Collman, J. P.; Devaraj, N. K.; Decreau, R. A.; Yang, Y.; Yan, Y.-L.; Ebina, W.; Eberspacher, T. A.; Chidsey, C. E. D., *Science* **2007,** *315*; (b) Collman, J. P.; Dey, A.; Decreau, R. A.; Yang, Y.; Hosseini, A.; Solomon, E. I.; Eberspacher, T. A., *Proc. Natl. Acad. Sci. U.S.A.* **2008,** *105*; (c) Collman, J. P.; Fu, L.; Herrmann, P. C.; Zhang, X., *Science* **1997,** *275*; (d) Collman, J. P.; Ghosh, S.; Dey, A.; Decreau, R. A.; Yang, Y., *J. Am. Chem. Soc.* **2009,** *131*; (e) Kim, E.; Shearer, J.; Lu, S.; Moenne-Loccoz, P.; Helton, M. E.; Kaderli, S.; Zuberbhler, A. D.; Karlin, K. D., *J. Am. Chem. Soc.* **1004,** *126*; (f) Kopf, M. A.; Karlin, K. D., *Inorg. Chem.* **1999,** *38*; (g) Liu, J.-G.; Naruta, Y.; Tani, F., *Angew. Chem.* **2005,** *117*.

(13) Zumft, W. G., *J. Inorg. Biochem.* **2005,** *99*, 194.

(14) Butland, G.; Spiro, S.; Watmough, N. J.; Richardson, D. J., *J. Bacteriol.* **2001,** *183*.

(15) (a) Lehnert, N.; Praneeth, V. K. K.; Paulat, F., *J. Comp. Chem.* **2006,** *27*; (b) Praneeth, V. K. K.; Haupt, E.; Lehnert, N., *Inorg. Chem.* **2005,** *99*; (c) Praneeth, V. K. K.; Näther, C.; Peters, G.; Lehnert, N., *Inorg. Chem.* **2006,** *45*; (d) Praneeth, V. K. K.; Neese, F.; Lehnert, N., *Inorg. Chem.* **2005,** *44*, 2570.

(16) Lim, M. D.; Lorkovic, I. M.; Ford, P. C., *J. Inorg. Biochem.* **2005,** *99*.
(17) (a) Bohle, D. S.; Hung, C.-H., *J. Am. Chem. Soc.* **1995,** *117*; (b) Choi, I.-K.; Ryan, M. D., *Inorg. Chim. Acta* **1988,** *153*; (c) Liu, Y.; DeSilva, C.; Ryan, M. D., *Inorg. Chim. Acta* **1997,** *258*.
(18) Cullotti, M.; Santagostini, L.; Monzani, E.; Casella, L., *Inorg. Chem.* **2007,** *46*.
(19) Collman, J. P.; Yang, Y.; Dey, A.; Decreau, R. A.; Ghosh, S.; Ohta, T.; Solomon, E. I., *Proc. Natl. Acad. Sci. U.S.A.* **2008,** *105*.
(20) Wasser, I. M.; Huang, H.; Moenne-Loccoz, P.; Karlin, K. D., *J. Am. Chem. Soc.* **2005,** *127*.
(21) Scheidt, W. R.; Ellison, M. K., *Acc. Chem. Res.* **1999,** *32*.
(22) (a) Hoshino, M.; Ozawa, K.; Seki, H.; Ford, P. C., *J. Am. Chem. Soc.* **1993,** *115*; (b) Traylor, T. G.; Sharma, V. S., *Biochemistry* **1992,** *31*.
(23) Wyllie, G. R. A.; Schulz, C. E.; Scheidt, W. R., *Inorg. Chem.* **2003,** *42*.
(24) (a) Kon, H.; Kataoka, N., *Biochemistry* **1969,** *8*; (b) Wayland, B. B.; Olson, L. W., *J. Am. Chem. Soc.* **1974,** *96*.
(25) (a) Huttermann, J.; Burgand, C.; Kappl, R., *J. Chem. Soc. Faraday Trans.* **1994,** *90*; (b) Morse, R. H.; Chan, S. I., *J. Biol. Chem.* **1980,** *255*; (c) Tyryshkin, A. M.; Dikanov, S. A.; Reijerse, E. J.; Burgard, C.; Huttermann, J., *J. Am. Chem. Soc.* **1999,** *121*.
(26) (a) Silvernail, N. J.; Barabanschikov, A.; Sage, J. T.; Noll, B. C.; Scheidt, W. R., *J. Am. Chem. Soc.* **2009,** *131*; (b) Silvernail, N. J.; Pavlik, J. W.; Noll, B. C.; Schulz, C. E.; Scheidt, W. R., *Inorg. Chem.* **2008,** *47*.
(27) Walker, F. A.; Benson, M., *J. Am. Chem. Soc.* **1980,** *102*.
(28) Cormode, D. P.; Drew, M. G. B.; Jagessar, R.; Beer, P. D., *Dalton Trans.* **2008,** *47*.
(29) Terazono, Y.; Patrick, B. O.; Dolphin, D. H., *Inorg. Chem.* **2002,** *41*.
(30) Kojima, T.; Nakanishi, T.; Honda, T.; Harada, R.; Shiro, M.; Fukuzumi, S., *Eur. J. Inorg. Chem.* **2009**.
(31) Lin, C.-L.; Fang, M.-Y.; Cheng, S.-H., *J. Electroanal. Chem.* **2002,** *531*.
(32) Paulat, F.; Berto, T. C.; DeBeer George, S.; Goodrich, L. E.; Praneeth, V. K. K.; Sulok, C. D.; Lehnert, N., *Inorg. Chem.* **2008,** *47*.
(33) Collman, J. P.; Dey, A.; Yang, Y.; Decreau, R. A.; Ohta, T.; Solomon, E. I., *J. Am. Chem. Soc.* **2008,** *130*.
(34) Komatsu, T.; Matsukawa, Y.; Tsuchida, E., *Chem. Letts.* **2000**.
(35) Lancuon, D.; Kadish, K. M., *J. Am. Chem. Soc.* **1983,** *105*.
(36) (a) Sheldrick, G.M. SHELXTL, v. 2008/3; Bruker Analytical X-ray, Madison, WI, 2008. (b) Sheldrick, G.M. SADABS, v. 2008/1. Program for Empirical Absorption Correction of Area Detector Data, University of Gottingen: Gottingen, Germany, 2008. (c) Saint Plus, v. 7.53a, Bruker Analytical X-ray, Madison, WI, 2008.
(37) (a) Collman, J. P.; Brauman, J. I.; Doxee, K. M.; Halbert, T. R.; Bunnenberg, E.; Linder, R. E.; LaMar, G. N.; Gaudio, J. D.; Lang, G.; Spartalin, K., *J. Am. Chem. Soc.* **1980,** *102*; (b) Collman, J. P.; Zhong, M.; Wang, Z.; Rapta, M., *Org. Lett.* **1999,** *1*.
(38) Young, R.; Chang, C. K., *J. Am. Chem. Soc.* **1985,** *107* (898-909).

Chapter 3

Synthetic Models for the Non-Heme Fe_B Site of NorBC

A clear mechanistic picture of how the heme/non-heme active site of NorBC activates NO is lacking, mostly due to insufficient knowledge about the properties of the non-heme iron(II)-NO adduct. Here, the first biomimetic model complexes for this species that closely resemble the coordination environment found in the protein are presented; using the ligands BMPA-Pr and TPA. The systematic investigation of these compounds allows for key insights into the geometric and electronic-structural properties of high-spin non-heme iron(II)-NO adducts. In particular, it is shown that small changes in the ligand environment of iron could be used by NorBC to greatly modulate the properties, and hence, reactivity of this species. Section 3.1 is adapted with permission from Berto, T. C., Hoffman, M. B.; Murata, Y.; Landenberger, K. B.; Alp, E. E.; Zhao, J.; Lehnert, N. *J. Am. Chem. Soc.* **2011**, *133*, 16714-16717.

In addition to the [Fe(BMPA-Pr)(NO)]X non-heme iron nitrosyl model complexes detailed above, several alternative models have also been synthesized based on derivatives of the BMPA-Pr ligand. Here, the ligands N-propanoate-N,N-bis-(2-pyridylethyl)amine (BEPA-Pr), N-(2-methyl-(2-chloromethyl-6-methylphenolate)-N,N-bis-(2-pyridylmethyl)amine (BMPA-PhO), and 2,6-di-(*ortho*-N-pyridyl-amine)pyridine (TPDA) are used to generate the corresponding non-heme iron complexes $[Fe(BEPA\text{-}Pr)]^+$, $[Fe(BMPA\text{-}PhO)]^+$, and $[Fe(TPDA)]^{2+}$. The interaction of these complexes with nitric oxide is also investigated.

3.1. [Fe(BMPA)(NO)]X Non-Heme Iron Nitrosyls

As discussed in Chapter 1, nitric oxide (NO) is an important biomolecule that serves as a signaling and immune defense agent in the human body, and an intermediate in denitrification. Importantly, since NO is acutely toxic to cells,[1] efficient mechanisms for detoxification of NO must be in place to

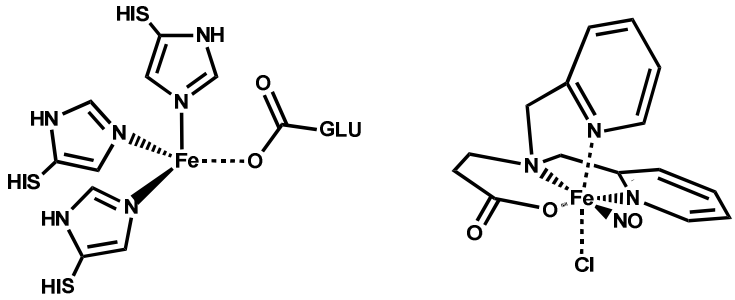

Scheme 3.1. Structural comparison of the Fe_B site within NorBC (left) and the model complex **1-Cl** (right).

avoid cellular damage. One viable pathway is the reduction of NO to less toxic N_2O, as observed in denitrifying bacteria.[2-3] To elucidate the biological pathways of controlling NO levels in cells, much research has been aimed at understanding one key enzyme, bacterial NO reductase (NorBC).[4-8] This protein contains a dinuclear active site with both a heme and a non-heme (Fe_B) center in close proximity. In the first step of catalysis, each ferrous iron center binds one molecule of NO,[2] but the following steps remain elusive. The basic properties of the ferrous heme-nitrosyl component of the active site are now well understood.[9-19] To advance our knowledge of the mechanism of NorBC, it is

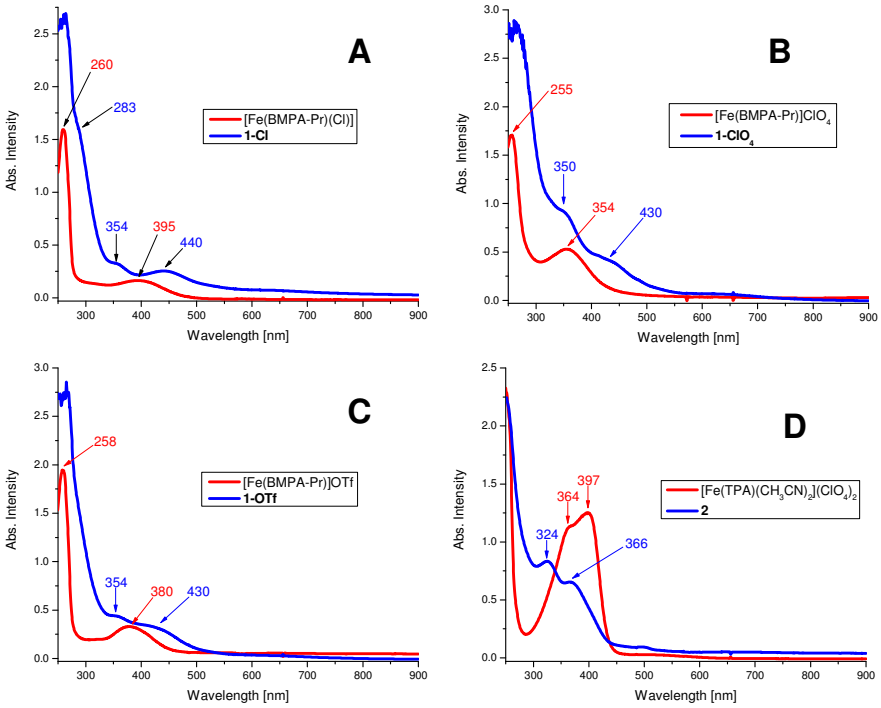

Figure 3.1. UV-Visible absorption spectra of **1** and **2** along with their corresponding ferrous precursor complexes.

of critical importance to develop a better understanding of the properties of the Fe_B(II)-NO adduct. A recent crystal structure of NorBC clarifies the coordination environment of the Fe_B site (Scheme 3.1) and provides the basis for moving forward in this direction.[20] Here, we report the first close spectroscopic and structural model complexes for the Fe_B(II)-NO center of NorBC, and systematically elucidate the factors that control the electronic structure, and hence, reactivity of this species.

Model complexes aimed at non-heme iron enzymes frequently employ derivatives of the ligand tris(2-pyridylmethyl)amine (TPA).[21-22] This ligand, however, does not accurately model the coordination environment of the Fe_B center of NorBC. We therefore substituted one of the methylpyridyl arms of TPA for a carboxylate group, yielding the biomimetic ligand BMPA-Pr. As shown in the following, non-heme iron(II)-NO complexes with BMPA-Pr and TPA show an amazing versatility in both complex geometry and the properties of the bound NO unit as a function of small alterations in the counter-ion and co-ligand. Synthesis of the ligand N-propanoate-N,N-bis-(2-pyridylmethyl)amine (BMPA-Pr) was carried out via previously published procedures.[23] Metal insertion by reaction with ferrous salts gave yellow-orange complexes [Fe(BMPA-Pr)]X (X = Cl^-, ClO_4^-, I^-, or $CF_3SO_3^-$ = OTf^-) with characteristic absorption bands in the 300 – 450 nm region (see Figure 3.1). The isolated iron complexes are EPR silent in accordance with their Fe(II) oxidation states. Upon addition of NO gas, brown [Fe(BMPA-Pr)(NO)]X (**1-X)** complexes are generated and show EPR activity (S=3/2). $[Fe(TPA)(CH_3CN)_2](ClO_4)_2$ was synthesized similarly to published procedures,[24] and exposure to NO gas then yielded $[Fe(TPA)(CH_3CN)(NO)](ClO_4)_2$ (**2**). Interestingly, the ferrous BMPA-Pr precursor complexes show

Table 3.1. Relevant redox potentials[a] for [Fe(BMPA-Pr)]X and select nitrosyls (vs. SHE).

Iron Complex		Fe(II)/Fe(III)
[Fe(BMPA-Pr)]Cl		203/508
$[Fe(BMPA\text{-}Pr)]ClO_4$		200/497
[Fe(BMPA-Pr)]OTf		242/513
$[Fe(TPA)(CH_3CN)_2](ClO_4)_2$[b]		860/—
Nitrosyl Derivative	**Fe—NO oxidation[c]**	**Fe—NO reduction**
1-OTf	589/1292	−290/−366
1-ClO_4	609/1323	−296/−386

[a] As the oxidation of **1-OTf** and **1-ClO_4** are non-reversible, only the oxidation peak is shown.

Fe(II)/Fe(III) redox potentials of about 200 – 250 mV vs. SHE in CH_3CN, which is very close to the value of 320 mV reported for the Fe_B center of NorBC.[3] In contrast, the redox potential of the ferrous TPA complex is 860 mV in CH_3CN,[24] indicating that the carboxylate of BMPA-Pr is able to greatly influence the properties of the resulting ferrous complexes. When measured in aqueous media, the Fe(II)/Fe(III) couple for [Fe(BMPA-Pr)]X complexes shifts to potentials around 500 mV vs. SHE (see Table 3.1). Besides the general effect of the solvent dielectric, we believe that this shift is also related to hydrogen bonding interactions of water with the carboxylate group, which result in a less anionic BMPA-Pr ligand and thus a more cationic Fe center (shifting the potential closer to that seen for Fe(TPA) derivatives). The nitrosyl complexes **1-OTf** and **1-ClO_4** show clear semi-reversible Fe-NO reductions and a non-reversible oxidation peak. Data obtained for **1-Cl** and **2** show multiple non-reversible redox processes in both acetonitrile and water. As such these complexes require further study and may not be suitable for reduction to the corresponding nitroxyl species, as discussed further in Chapter 4.

Elucidation of the exact coordination environment of the **1-X** complexes (X = Cl^-, OTf^-, and ClO_4^-) was carried out by X-ray crystallography. Excitingly, the refined structure of **1-Cl** reveals a geometry which is very similar to that of the non-heme Fe_B center of NorBC[20] (Scheme 3.1, left), in the case of which the three histidine ligands makeup a trigonal face and a carboxylate residue occupies a position *trans* to one of the histidine rings. The model **1-Cl** shows

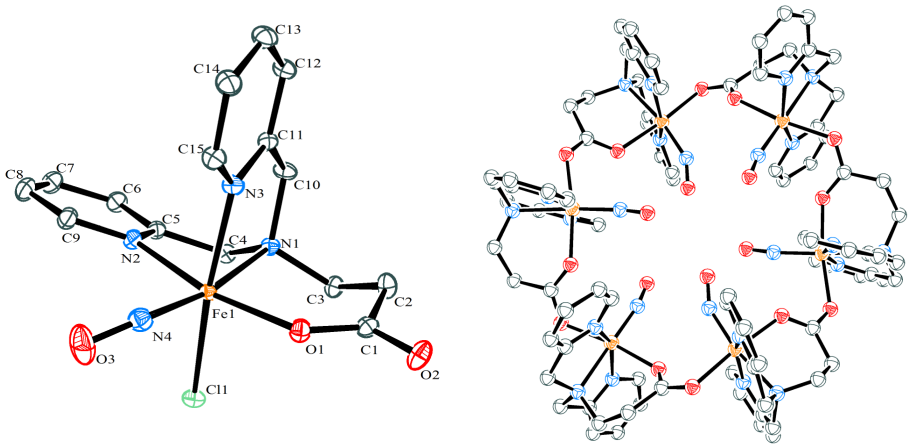

Figure 3.2. (left) Crystal structure of **1-Cl** showing a ligand arrangement very close to that seen in the Fe_B-NO adduct of NorBC. (right) Crystal structure of **1-ClO_4** showing an unexpected metallacrown hexamer. All solvent molecules and H atoms have been omitted for clarity.

a nearly identical coordination environment with pyridine ligands in the place of histidine. NO and chloride ligands then complete an octahedral geometry (Figure 3.2, left). Complex **1-Cl** shows a bent Fe-N-O unit with an angle of 152°, and Fe-NO and N-O distances of 1.783 and 1.154 Å, respectively. The strongly coordinating Cl^- counter-ion remains bound upon NO addition, and prevents coordination of solvent to the iron center.

In comparison, crystals of both **1-ClO$_4$** and **1-OTf** show a surprising propensity for the formation of unique metallacrown[25] hexamers (Figure 3.2, right) similar to the "ferric wheel" synthesized by Lippard and coworkers. Here, the open coordination site left by the non-coordinating counter-ion is not occupied by a solvent molecule. Rather, the carboxylate group of each unit

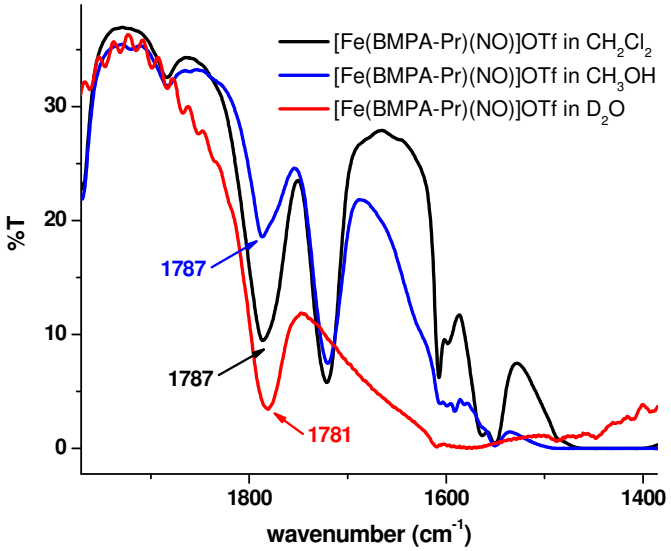

Figure 3.3. Solution IR spectra of **1-OTf** in CH_2Cl_2, CH_3OH, and D_2O. The shift observed in the presence of D_2O indicates a loss of the hexameric structure.

bridges between two adjacent iron centers, giving ring structures where all six NO moieties point toward the center of the ring. The oxygen atoms of the six NO ligands form an empty octahedron (volume ~ 20 Å^3). The geometries of the individual {Fe(BMPA-Pr)(NO)} units also differ from that seen in **1-Cl**. Whereas **1-Cl** shows a trigonal-facial arrangement of the N-donor groups of BMPA-Pr, **1-OTf** and **1-ClO$_4$** show the alternative meridional binding mode (cf. Figure 3.2). From DFT calculations on the facial and meridional isomers of **1-Cl**, the difference in total energy between these structures is only about 3 kcal/mol, indicating that the BMPA-Pr ligand easily reorients its binding mode. The hexameric metallacrowns **1-ClO$_4$** and **1-OTf** show average Fe-NO and N-O bond distances of 1.72 (1.76) Å and 1.18 (1.17) Å, respectively, and an average Fe-N-O angle of 152° (149°) (**1-OTf** values in parentheses).

Interestingly, the bridging carboxylate groups in the hexameric structures show equivalent Fe-O distances of ~2.07 Å to both iron centers, which is slightly longer than the 2.02 Å Fe-O bond observed for **1-Cl**. This strong Fe-OCO-Fe linkage causes the hexameric structures to be quite robust. Our current data indicate that the metallacrown is even maintained in solution based on solution IR and EPR spectra recorded in a variety of solvents (see Figures 3.3 and 3.4). Spectra recorded in H_2O/D_2O show features consistent with breakdown of the hexameric structure into separate H_2O-bound monomers. This claim is addressed further in regards to the effect on redox potential in Chapter 4.

EPR spectra were recorded for all nitrosyls **1-X** and **2**. Both **1-Cl** and **2** show typical S = 3/2 signals at liquid He temperatures with effective g values of approximately 4 and 2. These data are in accordance with the well established electronic structure of non-heme ferrous nitrosyls which show Fe(III)-NO^- electronic structures where the high-spin (hs) Fe(III) and NO^- (S=1) are antiferromagnetically coupled.[26] Interestingly, the hexameric complexes **1-OTf** and **1-ClO_4** show solution EPR spectra indicative of weak electronic coupling between the {Fe(BMPA-Pr)(NO)} units (see Figure 3.4). These data provide further indication that these hexamers remain intact in solution.

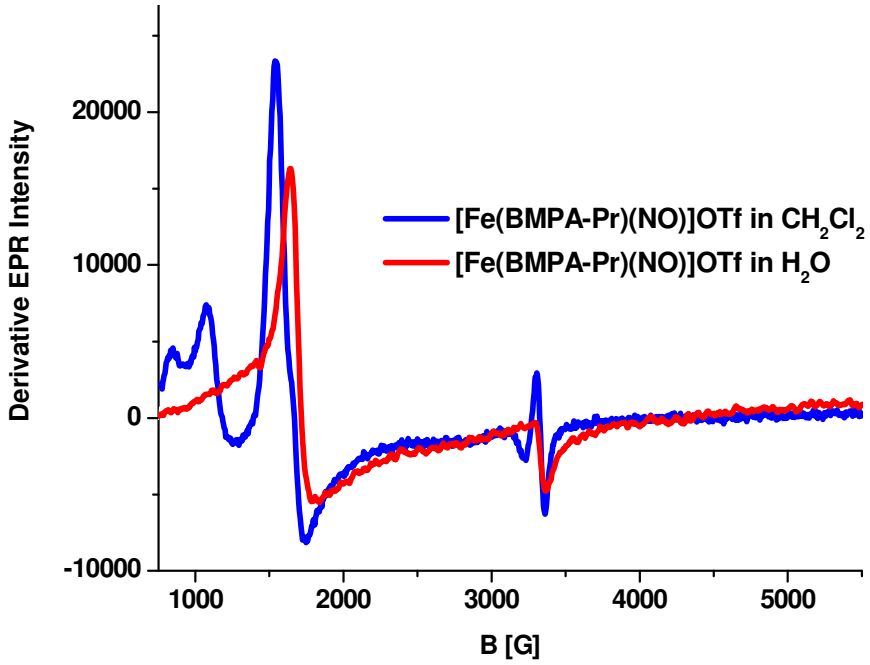

Figure 3.4. EPR spectrum of **1-OTf** showing coupling of the iron centers in CH_2Cl_2, indicating a hexameric structure. In H_2O, a typical monomeric S = 3/2 signal is seen.

A more detailed picture of the optical transitions of **1-OTf** and **1-Cl** was obtained with MCD spectroscopy. Here, the different selection rules which apply to MCD as compared to UV-visible absorption spectroscopy result in significantly more intense d-d and LMCT transitions. More specifically, the

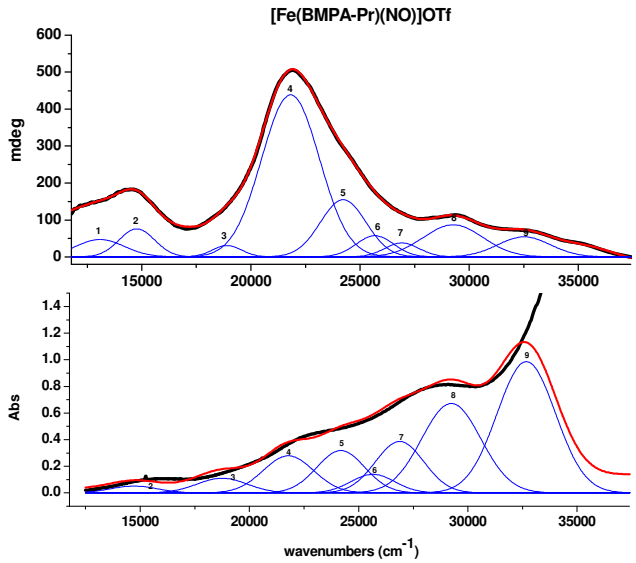

Figure 3.5. Overlay of MCD (top) and absorbance (bottom) spectra for **1-OTf**.

large spin-orbit coupling constants associated with metal-based d-d transitions lead to increased intensity for these transitions in the MCD spectra. For **1-OTf** and **1-Cl** samples were prepared as thin polystyrene films embedded with the corresponding non-heme iron nitrosyl and measured under variable temperature and magnetic field. The resulting data, shown in Figure 3.5, have been fit to individual Gaussian transitions which correspond to transitions within the Fe-NO unit. Here, the data for **1-OTf** have also been overlaid with the corresponding UV-visible absorption spectrum. Variable temperature, variable field (VTVH) magnetic saturation plots generated for the individual Gaussian features results in characteristic splitting patterns based on the polarizations of the individual transition. The VTVH curves display nearly identical splitting patterns across the measurement window (250 to 800 nm), indicating that the transitions are similarly polarized within the molecule (i.e. along the Fe-NO axis). This assignment is based on previously reported literature on synthetic and enzymatic non-heme iron nitrosyl complexes.[27] Figure 3.6 shows VTVH curves generated for the individual **1-OTf** transitions located at 20790 and 29070 cm^{-1}.

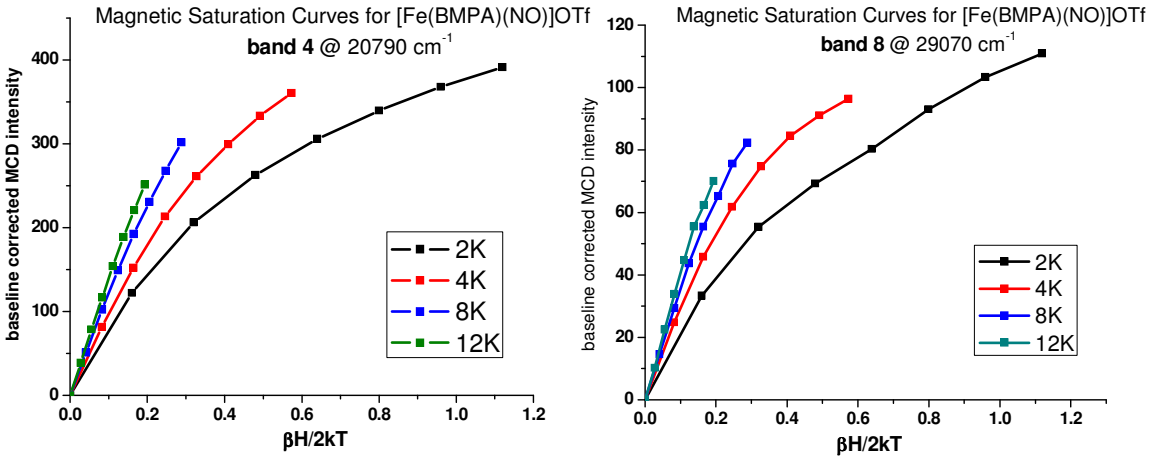

Figure 3.6. VTVH saturation curves generated for bands 4 and 8 from a Gaussian fit of the MCD data for **1-OTf** shown in Figure 3.5.

Vibrational spectroscopy was used to further characterize the nature of the Fe-N-O unit in **1-X** and **2**. Importantly, IR spectra of the **1-X** complexes show N-O stretching frequencies which are significantly effected by small changes in the coordination sphere. **1-Cl** has the lowest energy N-O stretch, ν(N-O), at 1726 cm^{-1} (in the single crystal). Exchange of chloride for iodide shifts ν(N-O) to 1769 cm^{-1}. Non-coordinating counter-ions such as ClO_4^- and OTf^- further shift ν(N-O) to 1777 and 1784 cm^{-1}, respectively. The N-O stretch of **1-I** is somewhat intermediate, which could either be due to iodide being a weaker donor than chloride, or the formation of a metallacrown structure. Finally, replacing the carboxylate in **1-X** with another pyridine, as in **2**, leads to an

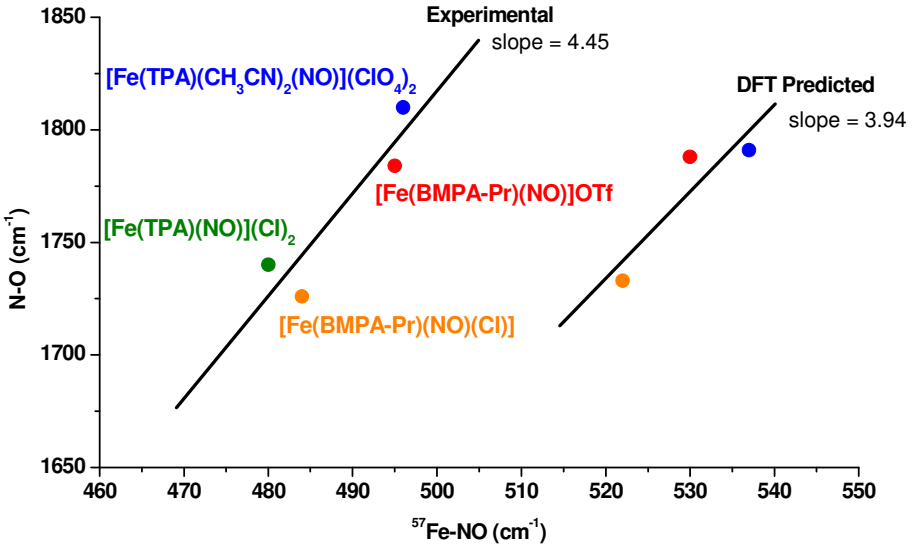

Figure 3.7. Correlation plot of ν(Fe-NO) versus ν(N-O) for **1-X**, **2**, and the chloride analog of **2**. The experimental (left) and DFT predicted (right) trends are shown.

N-O stretching frequency of 1810 cm^{-1}. An important hallmark of ferrous non-heme nitrosyls is therefore the dramatic tunability of the N-O bond strength,an impressive 84 cm^{-1} difference in ν(N-O) between **2** (1810 cm^{-1}) and **1-Cl** (1726 cm^{-1}) is observed here.[28] Consequently, the carboxylate ligand present in the Fe_B site of NorBC seems to play an important role in tuning the reactivity of the Fe_B-NO complex, and not simply provide a stable coordination sphere for iron as previously proposed.[8] Determination of the Fe-NO stretching modes is challenging as these vibrations are IR silent and the complexes show decomposition upon laser irradiation. To probe the iron-centered vibrations, Nuclear Resonance Vibrational Spectroscopy (NRVS) was therefore employed.[29] NRVS is ideally suited for this purpose, as the spectral intensity of a vibration is proportional to its amount of ^{57}Fe motion in this technique. Using $^{15}N^{18}O$ isotope labeling, the ^{57}Fe-NO stretching vibrations in **1-Cl**, **1-OTf**, and **2** were identified at 484, 495, and 496 cm^{-1}, respectively. While analysis of the

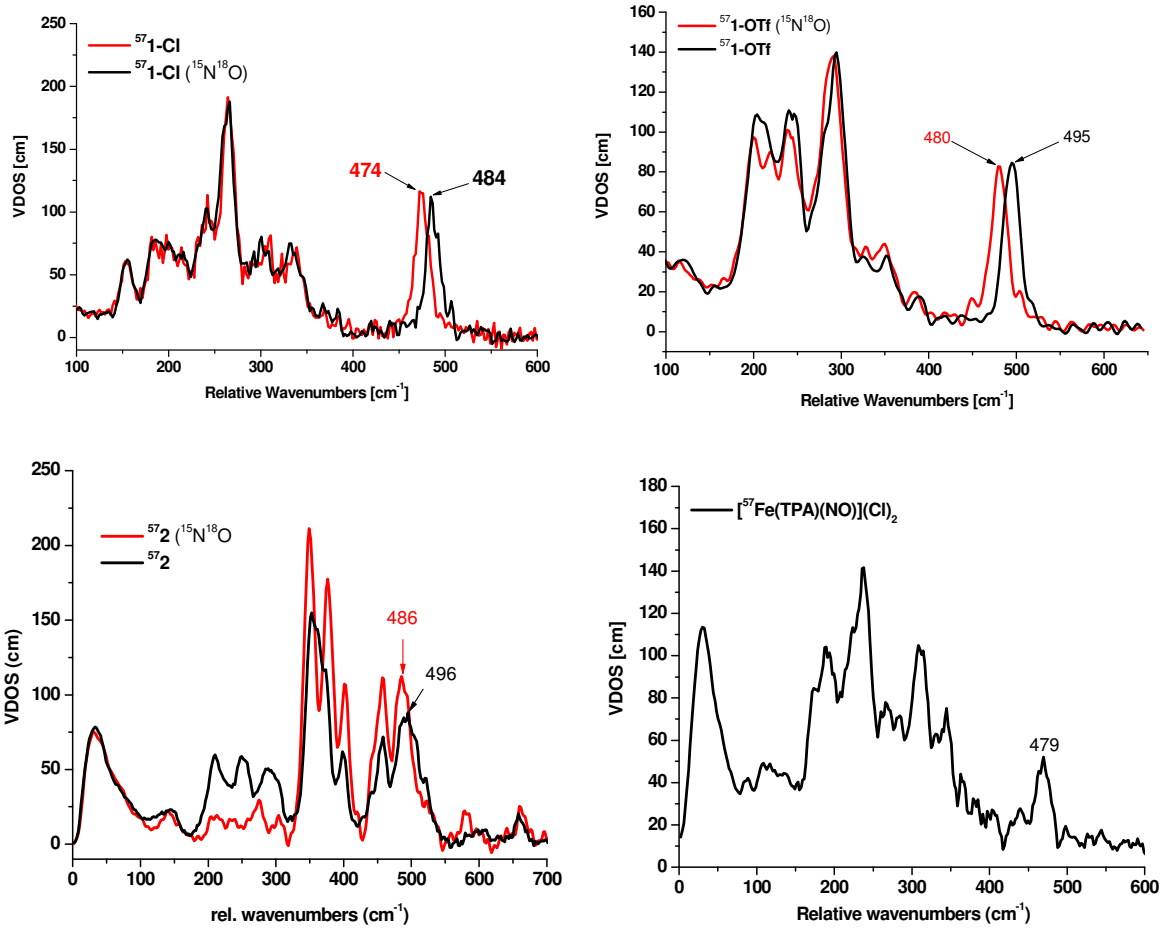

Figure 3.8. NRVS spectra of **1-Cl**, **1-OTf**, **2**, and $[Fe(TPA)(NO)](Cl)_2$ along with $^{15}N^{18}O$ isotope data where available. The prominent Fe-NO vibration is labeled in all cases.

NRVS data for both ^{57}**1-Cl** and ^{57}**1-OTf** is straightforward, ^{57}**2** shows a split feature in the ^{57}Fe-NO stretching region at 496 and 457 cm^{-1}. However, isotope substitution is only sensitive to the 496 cm^{-1} feature, clarifying this as the true ^{57}Fe-NO strech. Figure 3.7 shows a correlation plot of ν(Fe-NO) versus ν(N-O) for all these complexes along with [^{57}Fe(TPA)(NO)](Cl)$_2$. Importantly, the observed correlation between ν(Fe-NO) and ν(N-O) is <u>not</u> inverse, as would be expected for a change in Fe-NO backbonding along this series. In fact, a clear direct correlation is observed.

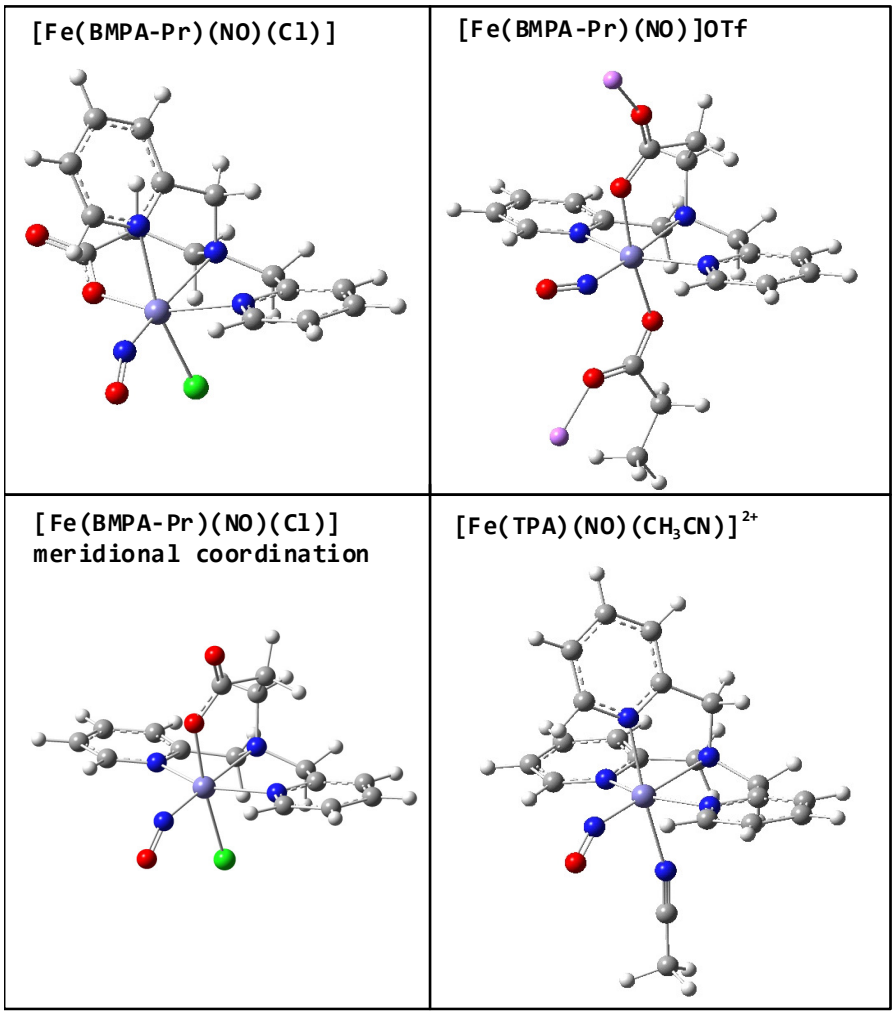

Figure 3.9. DFT optimized structures of **1-Cl**, a simplified model of **1-OTf**, and **2**. All structures were optimized at the BP86/TZVP level and show structural properties in agreement with experiment. See text for a more detailed description.

To better understand the nature of the Fe-NO bond and the observed trends in Fe-NO and N-O bond strengths (frequencies), DFT calculations were employed. The BP86/TZVP optimized structure of **1-Cl** shows excellent agreement with experiment; for example, the Fe-NO distance and Fe-N-O angle are obtained at

1.74 Å and 153°, respectively. The calculated N-O stretching frequency at 1733 cm^{-1} is close to the experimental value of 1726 cm^{-1}. The Fe-NO stretch is overestimated at 522 cm^{-1} compared to experiment (484 cm^{-1}), which is not unusual as gradient-corrected functionals commonly overestimate metal-ligand covalencies, and hence, bond strengths.[30] For the hexameric complexes **1-OTf** and **1-ClO_4**, a single {Fe(BMPA-Pr)(NO)} unit was constructed by terminating the carboxylate bridges with Li^+ ions. This model again reproduces the experimental geometry well and produces ν(Fe-NO) and ν(N-O) values of 530 and 1788 cm^{-1}, respectively. Finally, the vibrational properties of $[Fe(TPA)(CH_3CN)(NO)]^{2+}$ were calculated, predicting ν(Fe-NO) and ν(N-O) at 537 and 1791 cm^{-1}, respectively. Thus, the DFT results replicate the experimental vibrational frequencies of **1-X** and **2** well, and in particular, reproduce the direct correlation between ν(Fe-NO) and ν(N-O) (see Figure 3.7).

Because of the close agreement between experiment and DFT, the computational results based on *in silico* models (see Figure 3.9) can be used to gain insight into the electronic-structural reasons for the observed vibrational correlation. Analysis of the MO diagram of **1-Cl** reveals an electronic structure description that is in agreement with the hs Fe(III)-NO^- bonding scheme previously proposed.[26] Correspondingly, in the α-MO diagram, all iron d-orbitals are found singly occupied. In the applied coordinate system (Fe-NO vector corresponds to the z axis), the d_{xz} and d_{yz} orbitals form backbonds with the two unoccupied α-π* orbitals of NO, π^*_v and π^*_h. This interaction is quite weak, as evident from the corresponding antibonding MO's, α102 (72% π^*_v), α103 (33% π^*_h), and α104 (48% π^*_h), which only have small iron d-orbital contributions (see Figure 3.10). Note that the bending of the Fe-N-O unit also allows for weak backbonding of π^*_h with d_z2, as can be seen from the occupied MO α100 (41% d_z2, 19% π^*_h). In the β-spin MO diagram, all iron d-orbitals are empty, whereas the β-π* orbitals of NO are now occupied, in accordance with the NO^- (S=1) description of the NO ligand. The occupied β-π* orbitals of NO are ideally suited to donate into the empty β-spin d_{xz} and d_{yz} orbitals of iron. The strength of this interaction is again estimated best from the corresponding antibonding combinations, β100 (58% $d_{yz/z}2$, 30% π^*_h) and β102 (30% d_{xz}, 24% π^*_v), which show significant iron d-orbital and NO π* character (see Figure 3.10). As a result, the π donation from NO^- into the iron β-d_{xz} and β-d_{yz} orbitals is significant. In summary, *NO^- acts as a weak π-acceptor (α-spin) and a strong π-donor (β-spin) ligand in these complexes*. The calculated spin density distribution is in agreement with this description,

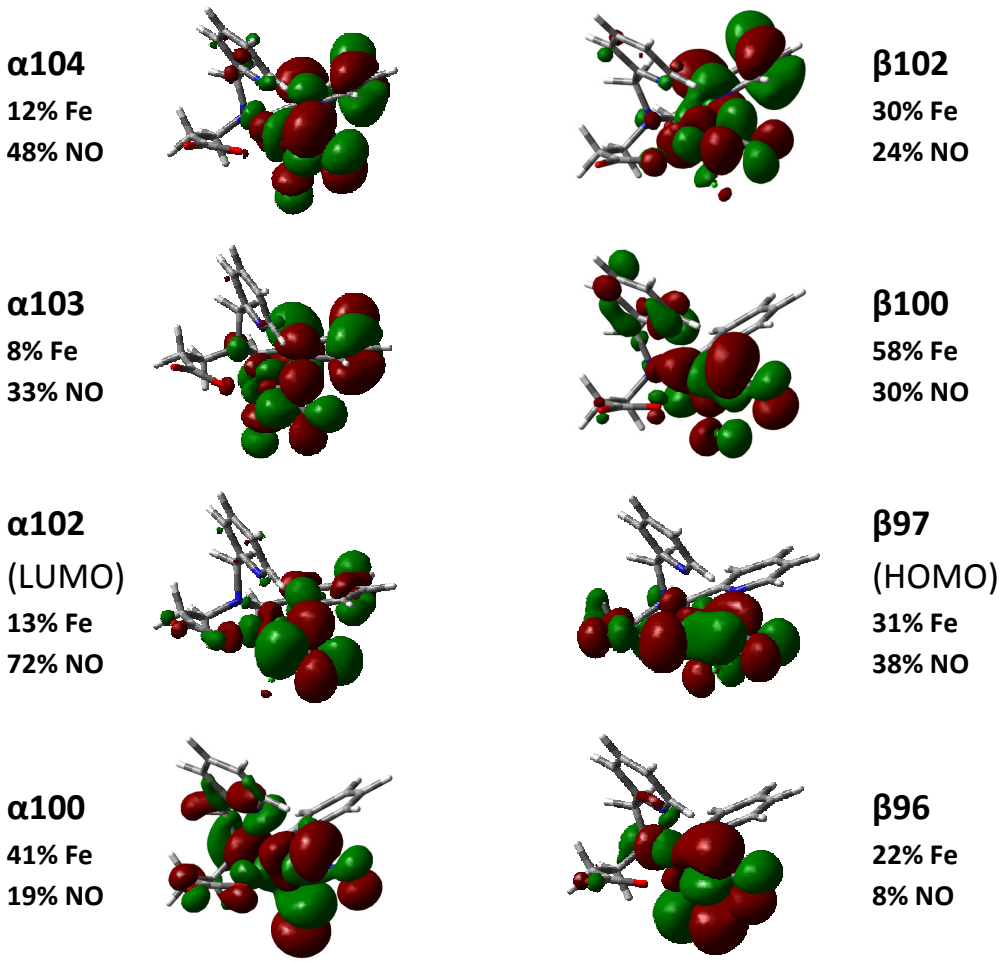

Figure 3.10. Isodensity surface plots of selected α-spin and β-spin MO's showing the interaction of Fe^{III} and NO^- in [Fe(BMPA-Pr)(NO)]Cl. In particular, β96 and β97 represent the π-donation of NO^- into the d_{xz} and d_{yz} orbitals of iron. Calculated at the BP86/TZVP theory level.

delivering values of +3.19 and -0.64 for Fe and NO, respectively. These values reflect the strong donation of negative (β) spin density from NO to iron, and the weak backdonation of positive (α) spin density from iron to NO. Importantly, the direct correlation between the Fe-NO and N-O bond strengths and vibrational frequencies can therefore be explained by variations in the amount of π-donation from the NO^- ligand to the iron center. Since this donation originates from N-O antibonding (π*) orbitals, a strengthening of this interaction (i.e. an increase in donation) results in the strengthening of both the Fe-NO and N-O bonds simultaneously, and hence, an increase in both ν(Fe-NO) and ν(N-O). *Interestingly, the observed trend in Figure 3.7 correlates with the number of anionic ligands bound to the iron center;* which is two for **1-Cl**, one (on average) for **1-OTf**,[31] and none for **2**. Hence, this effect seems to correlate with the effective nuclear charge of iron, where a

more negative iron center is less likely to accept electron donation from bound NO^-. Consequently, TPA complexes should exhibit the highest N-O stretching frequencies due to the lack of an anionic donor. The data support this trend as **2** shows ν(N-O) at 1810 cm^{-1}, and the related benzoylformate (BF, a delocalized weak anionic ligand) complex $[Fe(TPA)(BF)(NO)]ClO_4$ shows ν(N-O) at 1794 cm^{-1}.[32]

To conclude, structural, spectroscopic, and theoretical data on the first biomimetic model complexes for the non-heme Fe_B(II)-NO adduct of NorBC have been presented. The results have uncovered a surprising tunability of the properties of the Fe-NO bond in these systems based on the number of anionic donors bound to the iron center.[28] This tunability is synthetically easy to access as simple changes in co-ligand and counter ion lead to dramatic effects on the Fe-NO unit, as evidenced by a shift of 84 cm^{-1} in ν(N-O) between **1-Cl** and **2**. Note that the observed shift does not relate to the difference in BMPA-Pr binding mode. Further vibrational studies show that this tunability in the Fe-NO bond manifests itself as a direct correlation between Fe-NO and N-O bond strengths (frequencies). Specifically, changes in π-donation from the bound NO^- (S=1) ligand to hs Fe(III) are responsible for the observed correlation. These results have important consequences for NorBC catalysis, as our data suggest that the protein has the ability to control the properties of the Fe_B(II)-NO center in a similar fashion; i.e. by adjusting the number and donor strengths (via hydrogen bonding) of anionic ligands bound to the Fe_B center. Unfortunately, ν(N-O) of the Fe_B-NO complex is not known, so comparison with our model systems cannot be made. Considering redox potentials, the Fe_B center is only slightly more oxidizing than our BMPA-Pr model systems (in CH_3CN), which indicates (a) that glutamate remains bound to the Fe_B center upon reduction to the ferrous form, and (b) that hydrogen bonds to the bound glutamate are likely present, responsible for the increase in redox potential. Considering this scenario, we predict that the Fe_B-NO complex of NorBC has similar properties as the Fe-NO units in **1-OTf** and **1-ClO_4**. This aspect requires further study.

Initial reactivity studies with five-coordinate [Fe(Porph)(NO)] ($Porph^{2-}$ = TPP^{2-}, T*o*-F_2PP^{2-}) and six-coordinate [Fe(T*o*-F_2PP-BzIM)(NO)] complexes[4] show no reactivity upon simple mixing of the heme- and non-heme iron-nitrosyls in organic solvents. Considering that these complexes by themselves are also unreactive towards additional NO gas, the frequently cited radical type N-N coupling mechanism of NorBC is unlikely (compare. ref. [30]). Current studies

focus on adjusting redox potentials in the heme- and non-heme iron-nitrosyl complexes to investigate the possibility of (proton-assisted) reductive coupling between the two NO ligands. This work is detailed in Chapter 4.

3.2 Alternative Non-Heme Iron Nitrosyl Models

Alternative non-heme ligand scaffolds offer the opportunity to design more accurate structural models of the non-heme Fe_B site of NorBC. In particular, (BMPA-PhO) have been investigated with the aim of limiting the coordination

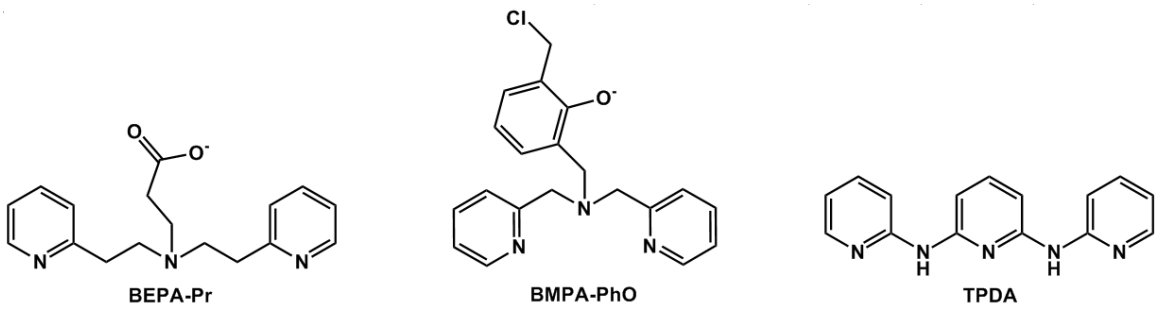

Scheme 3.2. Schematic representation of alternative non-heme ligands discussed in this chapter.

number of iron and preventing the formation of bridging metallacrowns, respectively. Additionally, the rigid tripyridyl-diamine ligand 2,6-di-(*ortho*-N-pyridylamine)pyridine (TPDA) has been employed.

Compared to BMPA-Pr, the ligand BEPA-Pr contains an extra methylene carbon in the pyridylalkyl units. In the corresponding iron complex $[Fe(BEPA\text{-}Pr)]^+$, this added length can be envisioned to wrap more completely around the iron center and thus sterically hinder formation of a six-coordinate species. In order to investigate this possibility the BEPA-Pr ligand was synthesized in a manner similar to that of BMPA-Pr employing N,N-bis-pyridylethylamine in the place of di-(2-picolyl)amine. Reaction with the desired ferrous salt (FeX_2) under anaerobic conditions then yields [Fe(BEPA-Pr)]X (X = ClO_4^- or I). These complexes show typical Fe(II) to pyridine charge transfer transitions at ~365 nm in the UV-visible absorbance spectrum along with a C=O stretching vibration at ~1600 cm^{-1} in the infrared spectrum.

Several attempts were made to crystallize [Fe(BEPA-Pr)]X with various counter-ions in order to determine the coordination number of the iron center. However, these trials only yield an oil product. It is therefore likely that the complex is not monomeric, but that the longer pyridylethyl arms allow for intermolecular coordination leading to the formation of oligimers. Similar results have been observed for copper adducts of the BEPA-Pr ligand.[33]

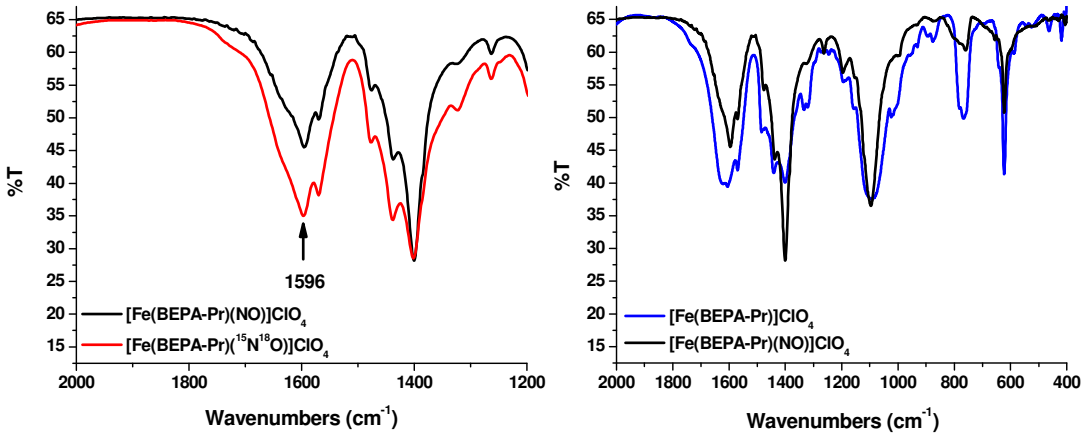

Figure 3.11. FT-IR spectra of $[Fe(BEPA\text{-}Pr)]ClO_4$ and $[Fe(BEPA\text{-}Pr)(NO)]ClO_4$ (right) along with $[Fe(BEPA\text{-}Pr)(NO)]ClO_4$ and the corresponding $^{15}N^{18}O$ derivative (left). Despite addition of NO gas, no observable shifts are seen in the infrared spectra.

Interaction of these complexes with NO gas results in an immediate color change to yellow/brown, presumably indicating formation of a ferrous nitrosyl complex. However, precipitation of the resulting compound followed by FT-IR analysis shows no ν(N-O) vibration (see Figure 3.11). This result points to two possible scenarios; 1) the Fe-NO bond is highly labile and NO is lost upon precipitation of the complex, or 2) the [Fe(BEPA-Pr)]X complex reacts with NO to generate some NO_x product.

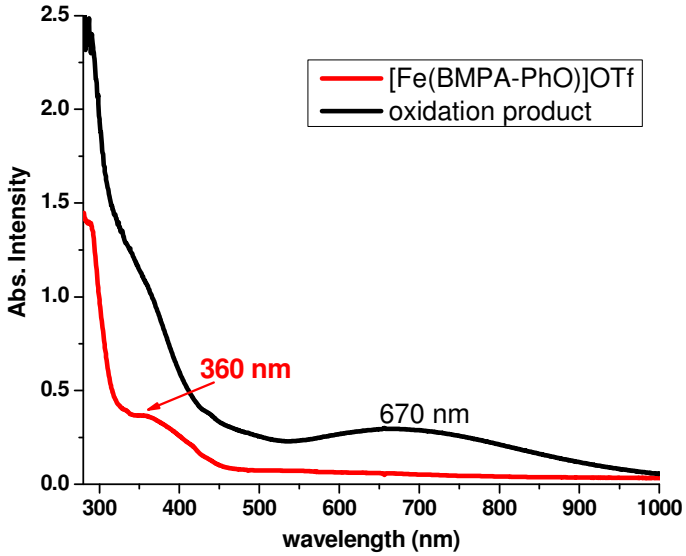

Figure 3.12. Absorption spectra of [Fe(BMPA-PhO)]OTf and the corresponding oxidation product.

In order to investigate the mechanism of NO loss, FT-IR gas headspace analysis was performed to analyze for N_2O (formed as a product of NO reduction). Here, N_2O formation is plausible as the color change to

yellow/brown upon NO addition indicates oxidation of the Fe(II) center, concomitant with NO reduction. Unfortunately, these attempts did not show N_2O in the reaction headspace. Nevertheless, the observed color change indicates reaction with NO leading to a new [Fe(BEPA-Pr)]-based product. The identity of this species has yet to be identified. One potential outcome is that the coordination of NO leads to a reorganization of the BEPA-Pr coordination-geometry, resulting in new iron to ligand optical transitions which give rise to the observed change in color.

Another potential route to accessing low coordination number non-heme iron complexes, similar to that observed in NorBC, is to prevent oligimerization through bridging ligand moieties. As seen in Section 3.1, the complexes [Fe(BMPA-Pr)(NO)]OTf and [Fe(BMPA-Pr)(NO)]ClO_4 are capable of forming hexameric metallacrown species through bridging of the carboxylate functionality on the BMPA-Pr ligand. The introduction of a phenolate moiety in place of this carboxylate yields the ligand BMPA-PhO which is less likely to oligimerize in solution. The BMPA-PhO ligand is obtained by the condensation of di-(2-picolyl)amine with one equivalent of 4-methyl-2,6-dichloromethyl phenol. This is followed by metallation with $Fe(OTf)_2$ to give [Fe(BMPA-PhO)](OTf) as a yellow solid. UV-visible absorption spectroscopy shows charge transfer transitions at 360 nm, consistent with the formation of a ferrous coordination complex. Due to the limited coordination environment, [Fe(BMPA-PhO)](OTf) is highly sensitive to oxidation, resulting in the formation of the corresponding blue ferric species which shows more intense Fe(III)-based transitions at ~340 nm along with a characteristic broad feature at 670 nm which is responsible for the observed blue color (see Figure 3.12).

Excitingly, addition of NO gas to [Fe(BMPA-PhO)](OTf) forms the nitrosyl complex [Fe(BMPA-PhO)(NO)](OTf) which is stable in the absence of dioxygen (see Figure 3.13). This material displays a ν(N-O) stretching vibration at 1785 cm^{-1} and a ^{57}Fe-N(O) vibration at 498 cm^{-1} as determined by FT-IR and NRVS spectroscopy, respectively. The correlation between these two vibrational properties lies to the right of the trend predicted in Figure 3.7, likely due to **3** being a five-coordinate species.

Alternatively, preliminary work has been completed using the rigid tripyridyl-diamine ligand TPDA. Here, metallation with iron(II) acetate yields [Fe(TPDA)]$(OAc)_2$ as an orange solid. Absorption measurements recorded on this material show a prominent feature at 335 nm along with a broad shoulder at ~430 nm. More importantly, introduction of NO gas to a stirred methanol

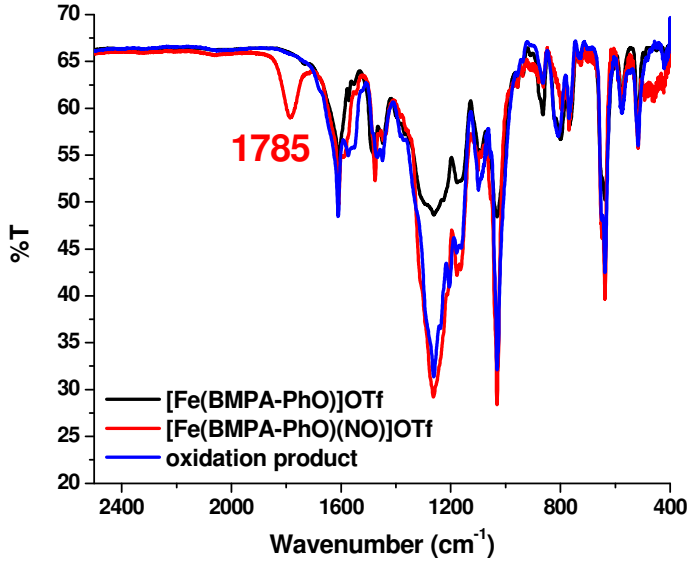

Figure 3.13. Infrared spectra of [Fe(BMPA-PhO)]OTf and the corresponding nitrosyl adduct. Oxidation of [Fe(BMPA-PhO)(NO)]OTf leads to loss of NO.

solution of $[Fe(TPDA)](OAc)_2$ results in the immediate formation of a nitrosyl complex which is accompanied by a color change to dark orange. Upon NO addition, the absorption features associated with the NO-free ferrous precursor change only slightly with the loss of the 430 nm shoulder and a slight shift in the 335 nm feature to 332 nm. This change is fully reversible upon argon purge, indicating reversible NO binding (see Figure 3.14). Additionally, infrared spectroscopy reveals two potential ν(N-O) stretching features at 1777 and 1709 cm^{-1}. Both the absorbance and infrared data suggest an atypical non-

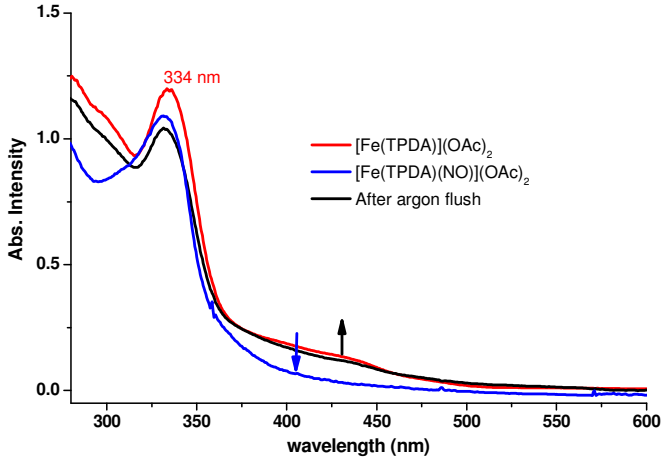

Figure 3.14. Absorbance spectra of $[Fe(TPDA)](OAc)_2$ and the corresponding nitrosyl adduct. An argon flush of the solution returns absorbance features in accordance with the starting complex $[Fe(TPDA)](OAc)_2$.

heme iron nitrosyl complex due to the relative lack of absorbance features and multitude of vibrational features present in the typical ν(N-O) region of the infrared spectrum. The observed spitting pattern in the IR spectra is also in line with formation of a dinitrosyl iron complex (DNIC) with an $\{Fe(NO)_2\}^9$ electronic structure;[34] using the classic Enemark and Feltham notation.[35] However, the EPR spectrum recorded at 4 K, as shown in Figure 3.15, indicates at least two non-integer spin species. The ratio of the peak at approximately g = 4 compared to that at g = 2 is too low to be a single S = 3/2 species. This data most likely corresponds to a mixture of both an S = 3/2 and S = 1/2 species in solution. At least two potential scenarios may lead to the observed data: 1) partial DNIC formation along with formation of a high-spin non-heme iron nitrosyl, or 2) formation of both low-spin and high-spin non-heme iron nitrosyls; either as separate species or as a spin-admixture. However, based on the sharp g = 2 feature in the EPR spectrum along with the additional g = 4 signal, DNIC formation is unlikely. A more likely scenario is simply the formation of two separate non-heme iron nitrosyl complexes leading to the observed split spectroscopic features.

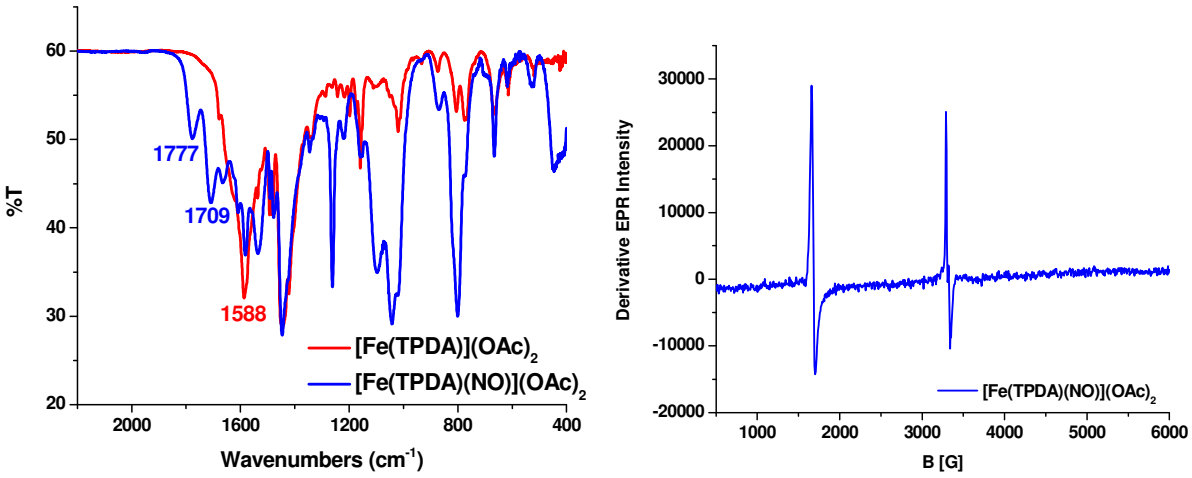

Figure 3.15. EPR spectrum of the nitrosyl product of $[Fe(TPDA)](OAc)_2$ taken at 4 K in a frozen methanol solution (right). IR spectra of $[Fe(TPDA)](OAc)_2$ and the corresponding NO adduct (left).

In an effort to generate a ligand which is more biomimetic and does not suffer from the tendency to form multiple iron nitrosyl derivatives, attempts have been made to covalently link a carboxylate moiety to the TPDA ligand framework. These trials include deprotonation of the TPDA ligand in dry DMSO with 1 equivalent of KOH and excess DIEA followed by the introduction of t-butyl chloroacetate with KI. Twenty four hour reflux afforded an impure oil

product which contains some fraction of the desired product (LCT-MS: m/z = 322, mass – t-butyl). Further trials included the replacement of NaH for KOH and the use of methyl 3-bromomethyl propionate in place of t-butyl chloroacetate without any noticeable success.

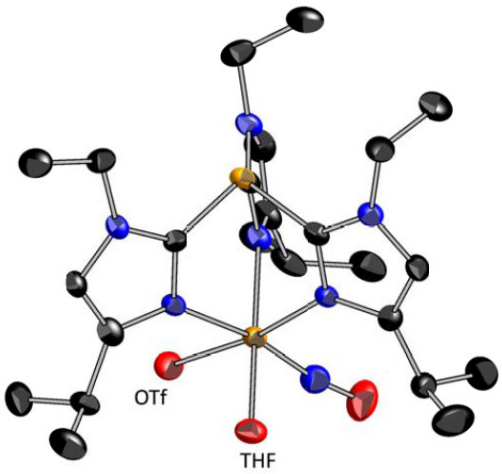

Figure 3.16. X-Ray crystal structure of [Fe(TlEt$_4$iPrlP)(OTf)(THF)(NO)]OTf. Determined by Dr. Chavez and coworkers at Oakland University.

Finally, the model complex [Fe(TlEt$_4$iPrlP)(OTf)(THF)(NO)]OTf (**3**) (shown in Figure 3.16) has been examined in collaboration with Dr. Ferman Chavez of Oakland University. Synthetic efforts and crystallographic analysis was carried out in Dr. Chavez's laboratory while spectroscopic analysis was performed in our laboratory. Infrared spectroscopy shows the ν(N-O) stretching frequency at 1831 cm^{-1} when **3** is ground in a KBr disc. This frequency shifts to 1842 cm^{-1} in CH_2Cl_2 solution. Importantly, no change in the ν(N-O) feature is

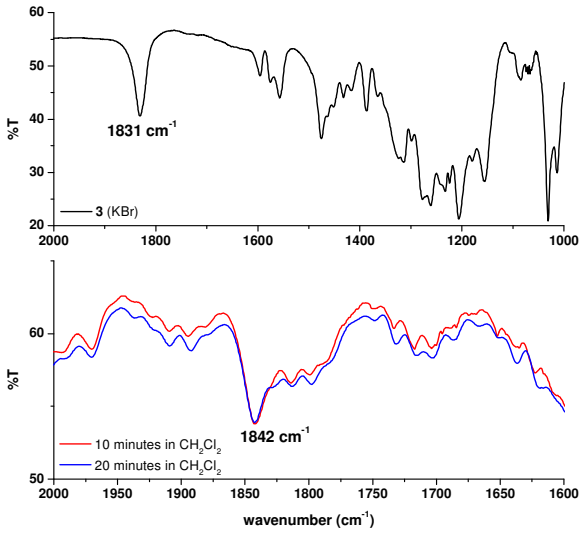

Figure 3.17. IR spectra of **3** recorded in KBr disc (top) and CH_2Cl_2 (bottom).

seen after 20 minutes in solution, indicating solution stability of the 1842 cm^{-1} species over this timeframe (see Figure 3.17). Interestingly, it is not yet clear if **3** maintains the same conformation in solution and in a KBr matrix. The 11 cm^{-1} shift observed upon dissolving **3** in CH_2Cl_2 may be indicative of structural rearrangement in solution; this issue is further discussed below.

In an effort to identify the Fe-NO stretching frequency, FT-raman spectroscopy was employed. As shown in Figure 3.18, these data show two potential Fe-NO features at 439 and 575 cm^{-1}. Due to the inconclusive nature of the FT-raman data, NRVS spectroscopy was performed. Here, ^{57}Fe-doped **3** shows a potential Fe-NO stretching feature at 447 cm^{-1} (see Figure 3.19). However, this feature does not display isotope sensitivity upon ^{15}NO labeling. Confident assignment of the Fe-NO stretch in **3** therefore remains inconclusive.

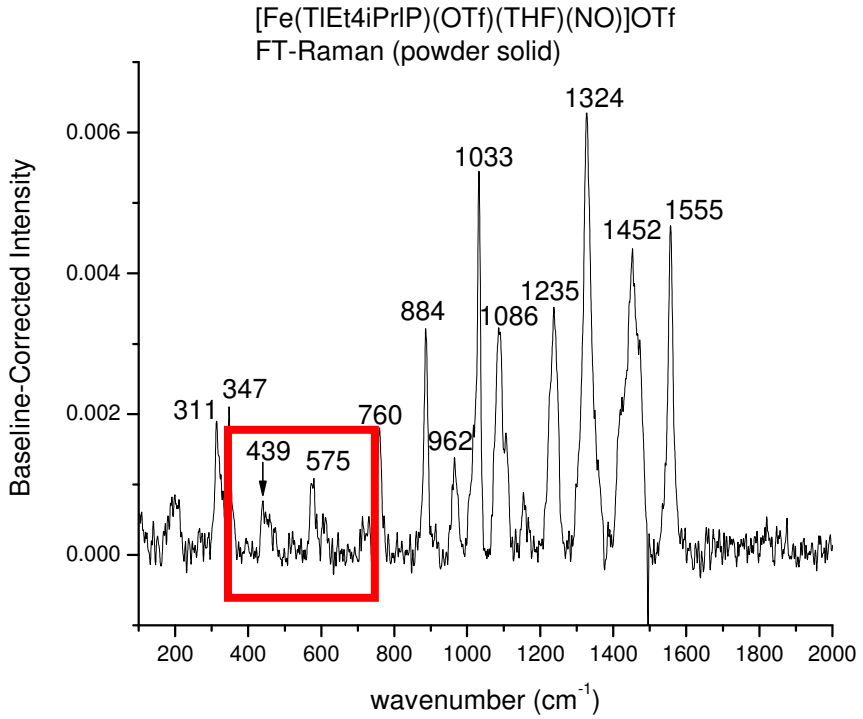

Figure 3.18. FT-raman spectra of **3** showing potential Fe-NO stretching features at 439 and 575 cm^{-1}.

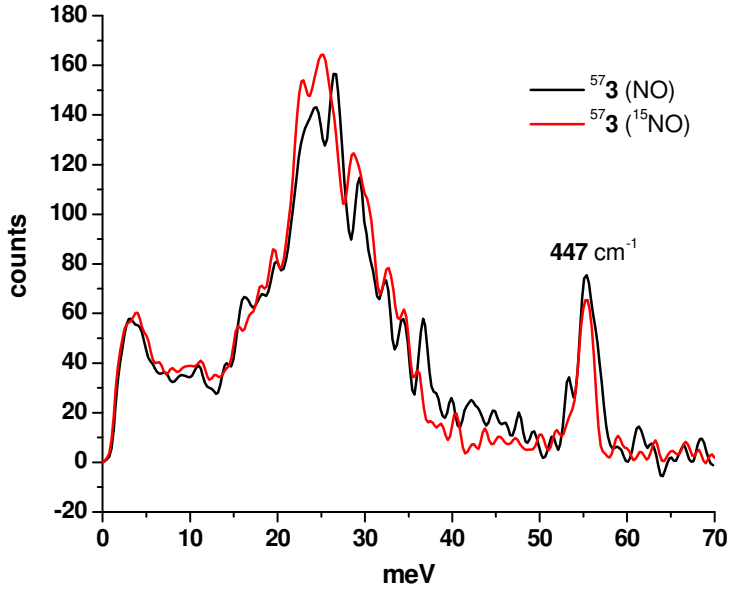

Figure 3.19. NRVS spectra of **3** showing potential Fe-NO stretch at 447 cm^{-1}. Interestingly, this feature does not appear to be isotope sensitive.

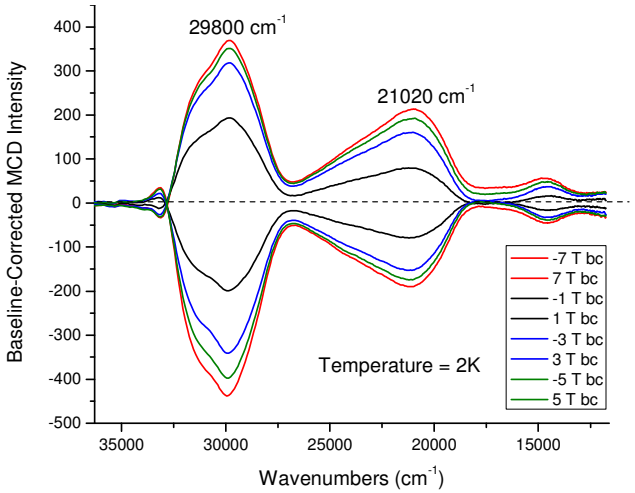

Figure 3.20. MCD spectra of **3** recorded at 2 K between 1 – 7 T. These features are consistent with reported high-spin non-heme iron nitrosyls.

Absorbance spectroscopy was used to further characterize **3**. MCD measurements were performed at low temperature between 0 – 7 T (see Figure 3.20). These data show typical high-spin non-heme iron nitrosyl features similar to those reported for **1-X** in section 3.1 of this chapter. Interestingly, UV-visible absorbance spectroscopy has been used to characterize the reactivity of **3** and the ferrous heme nitrosyl [Fe(*To*-

F_2PP)(NO)] under acidic conditions. Figure 3.21 shows the observed shift in the absorbance spectra upon addition of an acidic solution of [Fe(T*o*-F_2PP)(NO)] to solid **3**. These features are indicative of formation of ferric [Fe(T*o*-F_2PP)]Cl, indicating a reaction involving the nitrosyl unit. Somewhat

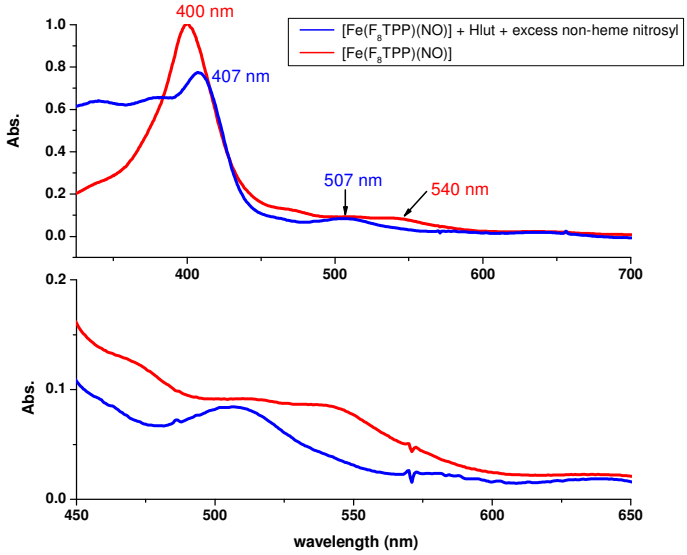

Figure 3.21. Absorbance spectra showing the reaction of **3** with [Fe(T*o*-F_2PP)(NO)] under acidic conditions. The resulting product (blue) displays features consistent with [Fe(T*o*-F_2PP)]Cl.

unexpectedly, this same reactivity is not observed when **3** is dissolved in solution prior to addition of the heme nitrosyl. This observation points to the potential isomerization of **3** in solution; leading to a less-reactive conformation. Headspace analysis using gas IR spectroscopy did not indicate N_2O formation during any of the reactivity experiments between **3** and [Fe(T*o*-F_2PP)(NO)].

Experimental

In general, reactions were performed applying inert gas (Schlenk) techniques. Preparation and handling of air sensitive materials was carried out under an argon atmosphere in an MBraun glovebox equipped with a circulating purifier (O_2, H_2O < 0.1 ppm). Infrared spectra were obtained from KBr disks on a Perkin-Elmer BX spectrometer. Proton magnetic resonance spectra were recorded on a Varian Inova 400 MHz and a Varian Mercury 300 MHz instrument. Electronic absorption spectra were measured using an Analytical Jena Specord 600 instrument. Electron paramagnetic resonance spectra were recorded on a Bruker X-band EMX spectrometer equipped with an Oxford

Instruments liquid nitrogen or liquid helium cryostat. EPR spectra were typically obtained on frozen solutions using ~20 mW microwave power and 100 kHz field modulation with the amplitude set to 1 G. Sample concentrations employed were ~1 mM.

CAUTION: Although no hazards were observed in this study, perchlorate salts are potentially explosive and should be handled with care.

Electrochemical studies were carried out with a CH instruments CHI660C electrochemical workstation. Cyclic voltammograms (CVs) were obtained using a three-component system, consisting of a platinum working electrode, a platinum auxiliary electrode, and a silver/silver chloride reference electrode. Spectra were recorded in either 0.1 M tetrabutylammonium perchlorate in CH_3CN or 0.1 M KCl in H_2O. Potentials were corrected to the SHE standard and the CH_3CN measurements were also corrected by measuring the ferrocenium/ferrocene couple under the same conditions (+624 mV vs. SHE).

Crystal structure determination was carried out using a Bruker SMART APEX CCD-based X-ray diffractometer equipped with a low temperature device and a fine focus Mo-target X-ray tube (wavelength: 0.71073 Å) operated at 1500 W power (50 kV, 30 mA). Measurements were taken at 85 K and the detector was placed ~5 cm from the crystal. The data were processed with SADABS and corrected for absorption. The structures were solved and refined with the Bruker SHELXTL (ver. 2008/3) software package.[36]

N-methylpropanoate-N,N-bis-(2-pyridylmethyl)amine. Prepared via the method of Carvalho et. al.[23] A solution containing 30 ml of methanol, 4.2 g (0.021 mol) of di-(2-picolyl)amine, and 5.7 ml (0.063 mol) of methylacrylate was allowed to stir for one week at room temperature. Upon completion of the reaction the crude material was concentrated by rotary evaporation of the solvent. Purification was carried out via column chromatography using silica and methanol as eluant. Yield: 5.0 grams (90%). ^{1}H NMR (300 MHz, CD_3OD): 8.4 (d, 2H), 7.6 (d, 2H), 7.3 (t, 2H), 7.2 (t, 2H), 3.8 (s, 4H), 3.6 (s, 3H), 3.0 (t, 2H), 2.6 (t, 2H).

N-propanoate-N,N-bis-(2-pyridylmethyl)amine sodium salt (Na[BMPA-Pr]). The sodium salt of N-propanoate-N,N-bis-(2-pyridylmethyl)amine was prepared by dissolving 0.525 g (1.84 mmol) of N-methylpropanoate-N,N-bis-(2-pyridylmethyl)amine in 5 ml of THF. A solution of 0.073 g (1.84 mmol) NaOH in

2 ml H_2O was then added to the THF solution and the biphasic mixture was allowed to stir at reflux for 7 hours, after which the aqueous layer was collected and the solvent removed by rotary evaporation. The obtained product was used without further purification. Yield: 500 mg (93 %). ^{1}H NMR (300 MHz, CD_3OD): 8.43 (d, 2H), 7.75 (t, 2H), 7.58 (d, 2H), 7.24 (t, 2H), 3.78 (s, 4H), 2.85 (t, 2H), 2.43 (t, 2H).

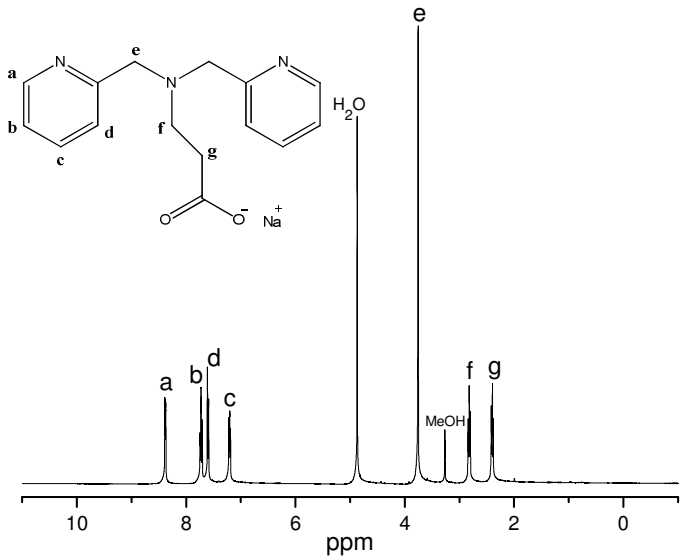

Figure 3.22. ^{1}H-NMR spectrum of Na[BMPA-Pr] taken in CD_3OD.

[Fe(BMPA-Pr)](X). A representative procedure for the metallation of the BMPA-Pr ligand is as follows. The ferrous salt can be exchanged for the desired counter ion without other modifications to the procedure. In the case of [Fe(BMPA-Pr)](Cl) the desired complex can be purified away from NaCl via Soxhlet extraction using $CHCl_3$. However, due to a strong tendency to trap solvents, complete drying of the product is not practical.

A small round bottom flask containing 0.33 g (1.13 mmol) of Na[BMPA-Pr] was purged of oxygen and placed under an argon atmosphere. To this, 3 ml of dry and air-free methanol (acetonitrile is used for the ClO_4^- analog) was added via syringe. Once the ligand was completely dissolved, a solution of 0.40 g (1.13 mmol) iron(II) triflate in 7 ml dry and air-free THF was added via syringe to the stirred ligand solution. The reaction solution immediately became yellow/orange in color and was allowed to stir for one hour before diethylether was added to precipitate the desired iron complex as a yellow solid. The material was dried under vacuum. Yield: 375 mg (70%) **[Fe(BMPA-Pr)]Cl.** Anal calcd for $C_{15}H_{16}N_3O_2ClFe \bullet CH_3OH \bullet C_4H_{10}O \bullet 0.95CHCl_3$: C, 43.30; H, 5.37; N, 7.23. Found: C, 43.16; H, 5.35; N, 7.47. **[Fe(BMPA-Pr)]ClO_4.** Anal

calcd for $C_{15}H_{16}N_3O_6ClFe$ • 0.25CH_3CN • 0.2 $C_4H_{10}O$: C, 43.44; H, 4.19; N, 10.10. Found: C, 43.32; H, 4.22; N, 10.10. **[Fe(BMPA-Pr)]OTf.** Anal calcd for $C_{16}H_{16}N_3O_5F_3SFe$: C, 40.44; H, 3.39; N, 8.84. Found: C, 40.06; H, 3.49; N, 8.86.

[Fe(BMPA-Pr)(NO)](X). A representative procedure for the nitrosylation of [Fe(BMPA-Pr)](X) is as follows.

A Schlenk flask was filled with 250 mg of [Fe(BMPA-Pr)](OTf) dissolved in 12 ml of dry and air-free CH_2Cl_2 (acetonitrile is used for the Cl^- and ClO_4^- analogs). The resulting yellow solution was exposed to NO gas while stirring for 10 minutes. Upon exposure to NO the solution becomes brown/black in color. Approximately 25 ml of pentane was added and the reaction was allowed to precipitate under a static NO atmosphere at -35°C overnight. Filtration yielded 270 mg of the desired nitrosylated complex in a near-quantitative yield. IR: **1-Cl**, ν(N-O) 1726 cm^{-1}; **1-ClO_4**, ν(N-O) 1777 cm^{-1}; **1-OTf**, ν(N-O) 1784 cm^{-1}; Anal calcd for $C_{16}H_{16}N_4O_6F_3SFe$ • 0.4CH_2Cl_2: C, 36.53; H, 3.14; N, 10.39. Found: C, 36.76; H, 3.14; N, 10.27. **1-I**, ν(N-O) 1769 cm^{-1}.

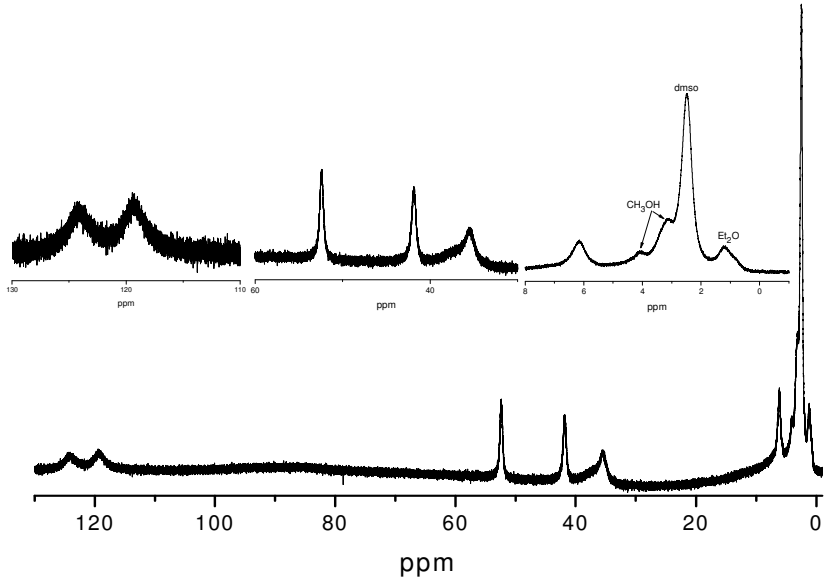

Figure 3.23. ^{1}H-NMR spectrum of [Fe(BMPA-Pr)]Cl taken in dmso-D_6 prior to Soxhlet extraction (see Materials and Methods). The proton shifts are in agreement with a high-spin ferrous complex with seven unique H positions.

Preparation of $^{57}FeCl_2$ for NRVS samples. A round bottom flask containing 507 mg of ^{57}Fe powder was fitted with a condenser and set under an argon atmosphere. To this flask was added 5 ml of concentrated HCl which had been freeze-pump-thawed to remove any O_2. The solution was allowed to stir at reflux overnight

until no more H_2 gas was evolved and all of the ^{57}Fe had dissolved. The resulting yellow/green solution was heated under vacuum to remove excess HCl and water. This resulted in 1.41 g of an off-white solid (125% Yield). This material is mostly $^{57}FeCl_2$ dihydrate (hence the > 100% yield). To obtain anhydrous material the solid was heated under vacuum to 240°C in the presence of P_2O_5 and $CaCl_2$ for 3 hours to yield a quantitative amount of $^{57}FeCl_2$. CAUTION: continued heating at these temperatures will result in loss of chloride and yield iron metal.

Preparation of $^{57}Fe(OTf)_2$ for NRVS samples. To a flask containing 191 mg of $^{57}FeCl_2$ dihydrate dissolved in 5 ml dry/ air-free THF was added a solution of 598 mg AgOTf (2 equivalents) in 3 ml of dry/ air-free THF. Immediate precipitation of AgCl occurred and the reaction was allowed to stir under argon for 30 minutes. The AgCl was then filtered off and the resulting $^{57}Fe(OTf)_2$ solution was used without further purification.

Crystallization of 1-X species. The desired [Fe(BMPA-Pr)(NO)](X) complex was dissolved in CH_3CN at a concentration of approximately 10 mg/ml. This solution was chilled to 10 °C and connected via glass adaptors to a flask of diethylether left at room temperature. After slow diffusion for 3-14 days crystals suitable for X-ray analysis were collected.

$[Fe(TPA)(CH_3CN)(NO)](ClO_4)_2$. Prepared via a modified procedure of Chiou et. al.[32] 150 mg of $[Fe(TPA)(CH_3CN)_2](ClO_4)_2$ was dissolved in 8 ml of dry and air-free CH_3CN. NO gas was then passed over the stirred solution for 20 minutes. The desired compound was precipitated as a brown solid with diethylether. Yield: 86%. As reported for analogous compounds in ref. [32], the facile loss of NO upon drying prevented the acquisition of an acceptable elemental analysis. IR: ν(N-O) 1810 cm^{-1}.

$[Fe(TPA)(NO)](Cl)_2$. Prepared analogously to $[Fe(TPA)(CH_3CN)(NO)](ClO_4)_2$ using $FeCl_2$ in place of $Fe(ClO_4)_2$ (hydrate) to generate the corresponding $[Fe(TPA)]^{2+}$ chloride salt (Yield: 55%). Addition of NO gas to a CH_3OH solution of $[Fe(TPA)](Cl)_2$ followed by diethylether precipitation yields a brown solid. Yield: 30%. IR: ν(N-O) = 1740 cm^{-1}.

bis-(2-pyridylethyl)amine. In a round bottom flask, 25.4 ml of 2-vinyl-pyridine was combined with 24.6 g of ammonium chloride and dissolved in 70 ml H_2O along with 10 ml CH_3OH. The reaction mixture was brought to reflux for 24

hours. After reflux, the reaction was cooled slowly to 0 °C in an ice bath. 60 ml of 30% NaOH was added and the solution took on an orange color. The product was extracted with six 20 ml portions of CH_3Cl and the organic layer was dried with Na_2SO_4, filtered, and evaporated under reduced pressure to yield a brown oil. Vacuum distillation at 60 mtorr yielded 2-pyridylethylamine at 120 °C followed by the desired product at 150 °C as a yellow oil. Yield: 22%. ^{1}H NMR (400 MHz, $CDCl_3$): 8.43 (d, 2H); 7.52 (t, 2H); 7.09 (d, 2H); 7.06 (t, 2H); 2.99 (t, 4H); 2.92 (t, 4H); 1.94 (s, 1H).

N-methylpropionic acid-N,N-bis-(2-pyridylethyl)amine. In a round bottom flask, 1.5 ml of bis-(2-pyridylethyl)amine was combined with 1.95 ml of methyl acrylate and dissolved in 6 ml CH_3OH. The reaction was stirred at room temperature for 1 week. Purification was achieved by loading the reaction solution directly onto a 25 x 3.5 cm silica column loaded and eluted with CH_3OH. Product obtained as a yellow oil. Yield: 90%. ^{1}H NMR (400 MHz, CD_3OD): 8.41 (d, 2H); 7.68 (t, 2H); 7.21 (m, 4H); 3.58 (s, 3H); 2.86 (m, 8H); 2.81 (t, 2H); 2.41 (t, 2H). LCT-MS: m/z = 314 (mass + H).

N-methylpropionate-N,N-bis-(2-pyridylethyl)amine. A suspension of 1.83 g N-methylpropionic acid-N,N-bis-(2-pyridylethyl)amine and 140 mg NaOH in 12 ml H_2O was brought to reflux for one hour. Over this time the solution became clear. Solvent was removed under reduced pressure and the resulting product was dried under vacuum to yield a tacky orange solid in quantitative yield. ^{1}H NMR (400 MHz, D_2O): 8.18 (d, 2H); 7.60 (t, 2H); 7.16 (d, 2H); 7.10 (t, 2H); 2.97 (m, 10H); 2.32 (t, 2H).

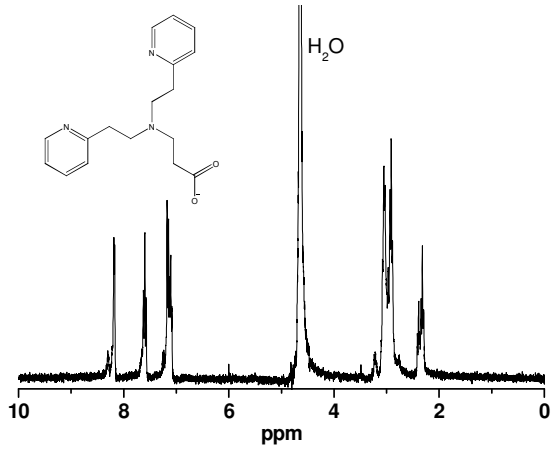

Figure 3.24. 1H-NMR spectrum of Na[BEPA-Pr] recorded in D2O.

[Fe(BEPA-Pr)]X. The ferrous BEPA-Pr complexes were prepared in an analogous procedure to [Fe(BMPA-Pr)](X) as detailed above. The BEPA-Pr ligand was used in place of BMPA-Pr.

N-(2-methyl-(2-chloromethyl-6-methylphenolate)-N,N-bis-(2-pyridylmethyl)amine. To a stirred solution to 150 mg 4-methyl-2,6-dichloromethyl phenol in 8 ml CH_3OH was slowly added 150 mg of di-(2-picolyl)amine in 2 ml CH_3OH. The resulting yellow solution was allowed to stir overnight. A yellow oil was obtained by removal of the solvent under reduced pressure and this oil was purified by silica column chromatography using 10% CH_3OH in CH_2Cl_2 as eluant collecting the first yellow band. Yield: 23%. LCT-MS: m/z = 371 (mass + 3). ^{1}H NMR (400 MHz, $CDCl_3$): 8.55 (d, 2H); 7.60 (t, 2H); 7.30 (d, 2H); 7.13 (t, 2H); 7.05 (s, 1H); 6.78 (s, 1H); 4.55 (s, 2H); 3.83 (s, 4H); 3.74 (s, 2H); 2.21 (s, 3H).

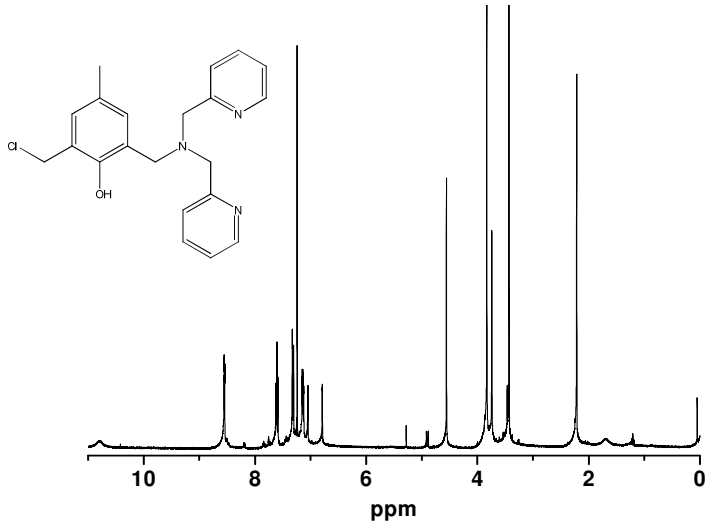

Figure 3.25. ^{1}H-NMR spectrum of the BMPA-PhO ligand recorded in $CDCl_3$.

[Fe(BMPA-PhO)]OTf. To a suspension of 64 mg N-(2-methyl-(2-chloromethyl-6-methylphenolate)-N,N-bis-(2-pyridylmethyl)amine in 5 ml dry/air-free CH_3OH was added 12 mg KOMe. The solution was briefly stirred and 68 mg of iron(II) triflate was added as a solution in 2 ml CH_3OH. The resulting red/orange solution was allowed to stir for 5 minutes before 18 ml diethyl ether was added in an attempt to precipitate the product. As no precipitation was observed after 19 hours, the solvent was removed under reduced pressure and the resulting red/brown product was used without further purification.

[Fe(BMPA-PhO)(NO)]OTf. Under inert atmosphere, 10 mg [Fe(BMPA-PhO)]OTf was dissolved in 1 ml CH_2Cl_2 and exposed to excess NO gas. The solution became immediately brown in color and after 5 minutes 10 ml of hexane was added to precipitate the product complex. Once precipitation was complete, excess NO was removed via argon flush and the solution was filtered under inert atmosphere to give a brown solid. Yield: <10 mg. IR: ν(NO) = 1785 cm^{-1}. NOTE: product is extremely air-sensitive yielding a deep blue solid upon oxidation.

2,6-di-(*ortho*-N-pyridylamine)pyridine. Under an argon atmosphere, 2.18 g of 2,6-diaminopyridine was dissolved in 30 ml of dry/air-free THF. A suspension of 1.51 g NaH in 30 ml THF was added and the resulting opaque solution was allowed to stir for 30 minutes at room temperature. At this time 5.85 g of 2-bromopyridine in 60 ml THF was added and the reaction was brought to reflux under an argon atmosphere. The reaction was allowed to reflux for 36 hours during which time the color became red/brown. After the reflux the solution was allowed to cool to room temperature before filtration and removal of the solvent under reduced pressure. The residue was then washed aqueous ammonium chloride followed by CH_2Cl_2 to yield a light brown product. The material was then brought to reflux in ~20 ml propanol and subsequently allowed to stand at room temperature overnight before filtration to yield a light tan solid which was dried under vacuum. Yield: 42 %. ^{1}H NMR (300 MHz, $(CD_3)_2SO$): 8.19 (s_{broad}, 2H); 7.80 (d, 2H); 7.60 (t, 2H); 7.48 (t, 1H); 7.13 (d, 2H); 6.82 (t, 2H). LCT-MS: m/z = 264 (mass + H).

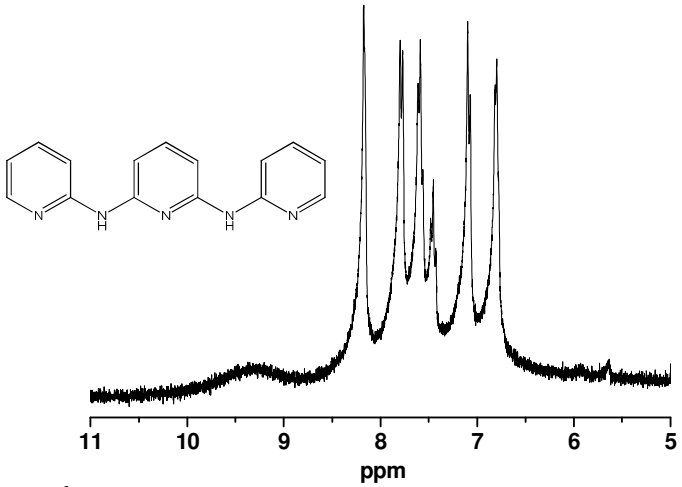

Figure 3.26. ^{1}H-NMR spectrum of the aromatic proton response for the TPDA ligand recorded in dmso-D_6.

[Fe(TPDA)](OAc)$_2$. Under an inert atmosphere 18 mg 2,6-di-(*ortho*-N-pyridylamine)pyridine was combined with a suspension of 18 mg $Fe(OAc)_2$ in 1 ml of CH_3OH. The mixture was stirred until all solid had dissolved. The desired product was precipitated with 4 ml diethylether. Yield: 22 mg.

References

(1) Burney, S.; Tamir, S.; Gal, A.; Tannenbaum, S. R., *Nitric Oxide* **1997,** *1*.
(2) Kumita, H.; Matsuura, K.; Hino, T.; Takahashi, S.; Hori, H.; Fukumori, Y.; Morishima, I.; Shiro, Y., *J. Biol. Chem.* **2004,** *279*, 55247.
(3) Zumft, W. G., *J. Inorg. Biochem.* **2005,** *99*, 194.
(4) Berto, T. C.; Praneeth, V. K. K.; Goodrich, L. E.; Lehnert, N., *J. Am. Chem. Soc.* **2009,** *131*, 17116.
(5) Collman, J. P.; Yang, Y.; Dey, A.; Decreau, R. A.; Ghosh, S.; Ohta, T.; Solomon, E. I., *Proc. Natl. Acad. Sci. USA* **2008,** *105*, 15660.
(6) Schopfer, M. P.; Wang, J.; Karlin, K. D., *Inorg. Chem.* **2010,** *49*.
(7) Xu, N.; Campbell, A. L. O.; Powell, D. R.; Khandogin, J.; Richter-Addo, G. B., *J. Am. Chem. Soc.* **2009,** *131*.
(8) Yeung, N.; Lin, Y.-W.; Gao, Y.-G.; Zhao, X.; Russell, B. S.; Lei, L.; Miner, K. D.; Robinson, H.; Lu, Y., *Nature* **2009,** *462*, 1079.
(9) Coyle, C. M.; Vogel, K. M.; Rush, T. S.; Kozlowski, P. M.; Williams, R.; Spiro, T. G.; Dou, Y.; Ikeda-Saito, M.; Olson, J. S.; Zgierski, M. Z., *Biochemistry* **2003,** *42*.
(10) Ford, P. C.; Laverman, L. E., *Coord. Chem. Rev.* **2005,** *249*.
(11) Lehnert, N.; Galinato, M. G. I.; Paulat, F.; Richter-Addo, G. B.; Sturhahn, W.; Xu, N.; Zhao, J., *Inorg. Chem.* **2010,** *49*.
(12) Lehnert, N.; Sage, J. T.; Silvernail, N. J.; Scheidt, W. R.; Alp, E. E.; Sturhahn, W.; Zhao, J., *Inorg. Chem.* **2010,** *49*.
(13) Patchkovskii, S.; Ziegler, T., *Inorg. Chem.* **2000,** *39*.
(14) Praneeth, V. K. K.; Nather, C.; Peters, G.; Lehnert, N., *Inorg. Chem.* **2006,** *45*, 2795.
(15) Silvernail, N. J.; Barabanschikov, A.; Sage, J. T.; Noll, B. C.; Scheidt, W. R., *J. Am. Chem. Soc.* **2009,** *131*.
(16) Silvernail, N. J.; Olmstead, M. M.; Noll, B. C.; Scheidt, W. R., *Inorg. Chem.* **2009,** *48*, 971.
(17) Wyllie, G. R. A.; Scheidt, W. R., *Chem. Rev.* **2002,** *102*, 1067.
(18) Wyllie, G. R. A.; Schultz, C. E.; Scheidt, W. R., *Inorg. Chem.* **2003,** *42*.
(19) Zhang, Y.; Gossman, W.; Oldfield, E., *J. Am. Chem. Soc.* **2003,** *125*.
(20) Hino, T.; Matsumoto, Y.; Nagano, S.; Sugimoto, H.; Fukumori, Y.; Murata, T.; Iwata, S.; Shiro, Y., *Science* **2010,** *330*, 1666.
(21) Friedle, S.; Reisner, E.; Lippard, S. J., *Chem. Soc. Rev.* **2010,** *39*.
(22) Que, L., Jr., *Acc. Chem. Res.* **2005,** *40*.
(23) Carvalho, N. M. F.; Horn, A., Jr.; Bortoluzzi, A. J.; Drago, V.; Antunes, O. A. C., *Inorg. Chim. Acta* **2006,** *359*.
(24) Zang, Y.; Kim, J.; Dong, Y.; Wilkinson, E. C.; Appelman, E. H.; Que, L., Jr., *J. Am. Chem. Soc.* **1997,** *119*, 4197.
(25) Lah, S. M.; Pecoraro, V. L., *J. Am. Chem. Soc.* **1989,** *111*.
(26) Brown, C. A.; Pavlosky, M. A.; Westre, T. E.; Zhang, Y.; Hedman, B.; Hodgson, K. O.; Solomon, E. I., *J. Am. Chem. Soc.* **1995,** *117*, 715.
(27) Jackson, T. A.; Yikilmaz, E.; Miller, A.-F.; Brunold, T. C., *J. Am. Chem. Soc.* **2003,** *125* (8348-8363).
(28) In *As the non-coordinating counter-ions are not bound directly to the iron center, their presence indirectly affects the coordination sphere of iron by limiting the number of anionic ligands bound to the iron center.*
(29) Scheidt, W. R.; Durbin, S. M.; Sage, J. T., *J. Inorg. Biochem.* **2005,** *99*, 60.
(30) Goodrich, L. E.; Paulat, F.; Praneeth, V. K. K.; Lehnert, N., *Inorg. Chem.* **2010,** *49*.

(31) In *As the carboxylate groups are equally bridged between two iron centers in **1-OTf**, the net anionic effect is comparable to having approximately one single unshared carboxylate ligand bound to the iron center.*
(32) Chiou, Y.-M.; Que, L., Jr., *Inorg. Chem.* **1995,** *34*, 3270.
(33) Zhang, Y.; Liang, H.-C.; Zakharov, L. N.; Das, S. K.; Hetu, M. M.; Rheingold, A. L., *Inorg. Chim. Acta* **2007,** *360*, 1691.
(34) Hung, M.-C.; Tsai, M.-C.; Lee, G.-H.; Liaw, W.-F., *Inorg. Chem.* **2006,** *45*, 6041.
(35) Enemark, J. H.; Feltham, R. D., *Coord. Chem. Rev.* **1974,** *13*, 339.
(36) In *(a) Sheldrick, G. M. SHELXTL, V. 2008/3; Bruker Analytical X-ray: Madison, WI, 2008. (b) Sheldrick, G. M. SADABS, V. 2008/1, Program for Empirical Absorption Correction of Area Detector Data; University of Goettingen: Goettingen, Germany, 2008. (c) Saint Plus, V. 7.53a; Bruker Analytical X-ray: Madison, WI, 2008.*

Chapter 4

Reactivity of Heme and Non-Heme Iron Nitrosyls

The reactivity between heme and non-heme iron nitrosyls can be tested under a variety of conditions. In theory, highly reactive components can simply be mixed in homogeneous solution which relies on molecular collisions to bring the desired nitrosyl moieties into close proximity.[1] However, alternative research in our lab on non-heme diiron dinitrosyl complexes has shown NOR activity *only* when the two Fe-NO moieties are covalently linked. Functional diiron heme/non-heme model complexes present in the literature also exhibit covalently linked structures.[2] The mononuclear heme and non-heme iron nitrosyls presented in this thesis have been tested for NOR activity as independent molecules and preliminary steps towards the development of covalently linked heme/non-heme diiron constructs have been completed.

4.1. Reactivity and Mechanistic Insight

As discussed in Chapter 1, the reduction of NO by NorBC requires a new N-N bond to be formed between two NO molecules.[3] This process is likely facilitated by the formation of both a heme and non-heme iron nitrosyl species within the NorBC active site.[4-5] Here, we have employed synthetic heme and non-heme iron nitrosyl complexes along with a series of radical species to mimic the proposed reductive N-N coupling of bacterial NORs. The key questions to be addressed are 1) What is the mechanism of N-N bond formation? and 2) What is the electronic structure of the heme and non-heme iron sites that allows for this coupling?

Reactivity of Ferrous Heme Nitrosyls with Soluble Radical Species

One proposed mechanism of N-N bond formation is through a radical-radical coupling of two coordinated NO· species.[4] Here, the unpaired electrons which are localized on the N-atoms of two nitric oxide molecules can combine to generate a new N-N bond. Six-coordinate ferrous heme nitrosyls as models for the heme b_3 site of NorBC should be ideally suited to probe this reaction due

to their Fe(II)-NO· electronic structure. However, radical-based N-N coupling is suspect as ferrous heme nitrosyls do not react with either free NO or intermolecularly in homogenous solution; potentially due to the strength of the Fe-NO bond. If a radical coupling mechanism were feasible, these types of complexes with a high degree of radical character on NO would be expected to facilitate such a reaction. In order to better gauge the reactivity of these nitrosyl complexes, [Fe(T*o*-F_2PP)(NO)] was exposed to a variety of radicals such as superoxide (O_2^{2-}), (2,2,6,6-Tetramethylpiperidin-1-yl)oxyl (TEMPO), solublized nitric oxide, and other Fe(II)-NO· species.

Of the above listed radical species, only superoxide shows reactivity with the ferrous heme nitrosyl [Fe(T*o*-F_2PP)(NO)]. It is not that surprising that TEMPO fails to react due to its relatively stable nature. However, if a radical-based NO/NO coupling mechanism is plausible, it would be expected that high radical character nitrosyl species perform this coupling. It is now well known that ferrous heme nitrosyls retain a substantial amount of radical character on the bound NO molecule.[6] As an example, DFT calculations at the B3LYP/LANL2DZ* theory level predict the five-coordinate ferrous heme nitrosyl [Fe(P)(NO)] (P = porphine) to have a spin density of 0.50 on NO compared to 0.49 on iron. Due to a sharing of the d_{z^2} orbital on iron, six-coordinate ferrous heme nitrosyls display an even larger radical character on NO in the presence of an axial donor ligand *trans* to NO.[7-9] With this in mind, the fact that even six-coordinate ferrous heme nitrosyls are unreactive towards themselves and excess NO gas provides strong evidence that factors other than radical character contribute to the NO/NO coupling mechanism performed by NorBC (see Chapter 5). In fact, this evidence substantiates a case against a radical-based *trans* mechanism even being possible for NorBC.

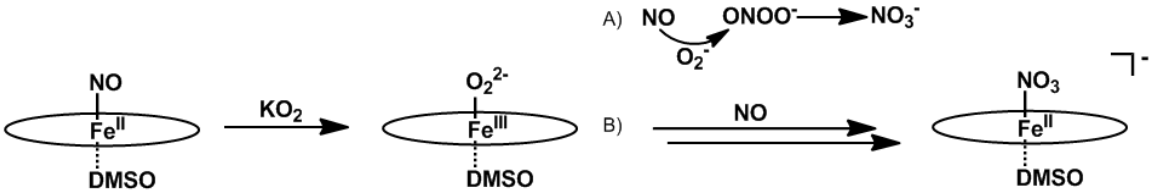

Scheme 4.1. Proposed mechanistic schemes for the reaction of superoxide with [Fe(TPP)(NO)] in DMSO. Pathway A) shows free NO attack on excess O_2^- while B) shows NO attack on bound peroxide O_2^{2-}.

Unlike the data presented above, superoxide displays rapid reactivity with 0.1 equivalents of [Fe(TPP)(NO)] to generate a new product. As observed by UV-visible absorption spectroscopy, this new species displays absorption features

at 428, 545, 571, and 625 nm in DMSO solution (see Figure 4.1). The observed reaction proceeds via a short-lived intermediate which shows a distinct Soret absorption at 437 nm. Based on previously reported [Fe(TPP)] reactivity with superoxide, this 437 nm intermediate has been characterized as [Fe^{III}(TPP)(O_2^{2-})].[10] As the observed intermediate generated from the reaction of superoxide with [Fe(TPP)(NO)] is identical to that observed when [Fe(TPP)] is substituted for the analogous nitrosyl, it is most likely that the initial reaction of simple ferrous heme nitrosyls with superoxide involves the displacement of NO by O_2^-. The reactivity observed is therefore not between bound NO and O_2^-, but rather between O_2^- and the iron center of [Fe(TPP)(NO)]. Upon NO displacement, binding of O_2^- results in oxidation of [Fe(TPP)] leading to a formally Fe(III)-O_2^{2-} complex (blue trace in Figure 4.1).

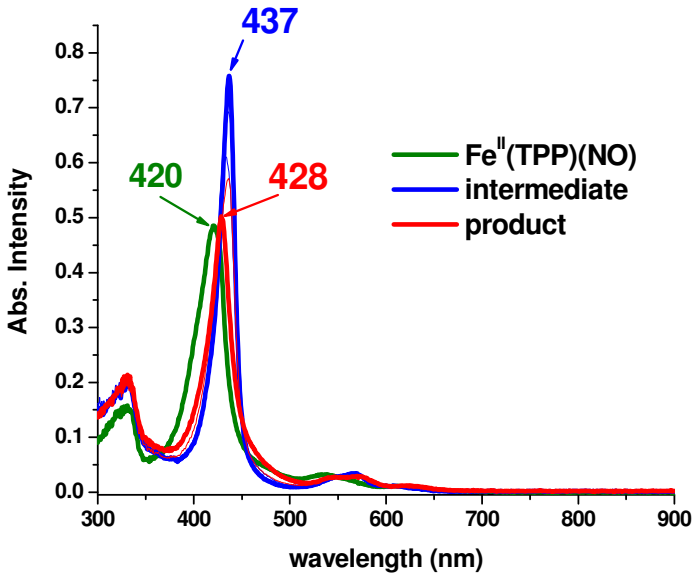

Figure 4.1. Absorbance spectra showing the reaction of [Fe(TPP)(NO)] with superoxide in DMSO.

Once free NO has been released into solution, two potential mechanistic pathways exist; the rapid reaction (~10^{10} M^{-1} s^{-1}) between NO and free O_2^- or attack of NO on the intermediate [Fe^{III}(TPP)(O_2^{2-})].[11-12] This results in the transient formation of peroxynitrite which rapidly isomerizes to nitrate. This scenario will either lead to [Fe^{II}(TPP)(DMSO)(NO_3)]$^-$ in the case of NO attack on [Fe^{III}(TPP)(O_2^{2-})], or result in free nitrate in solution with [Fe^{III}(TPP)(O_2^{2-})]. It is important to note that the formation of free NO_3^- requires the presence of excess superoxide to facilitate peroxynitrite, and ultimately nitrate, formation away from the heme center. The final 428 nm product which

is observed is thus likely due to an interaction of NO with [Fe^{III}(TPP)(O_2^{2-})] to form [Fe^{II}(TPP)(DMSO)(NO_3)]$^-$ as proposed in Scheme 4.1.[13] Comparison to literature values strongly favors formation of a ferrous heme as the ferric variety displays a notably different Soret position in the presence of nitrate.[12]

Reactivity between Uncoupled Heme and Non-Heme Iron Nitrosyls

Non-heme iron nitrosyls [Fe(BMPA-Pr)(NO)]X have been exposed to separate heme and non-heme nitrosyl complexes such as [Fe(BzIM)(NO)] and [Fe(T*o*-F_2PP)(NO)] under neutral and acidic conditions in an effort to induce NOR activity. In theory, the two electrons necessary for NO reduction can be supplied by oxidation of both iron centers to yield the di-ferric product and N_2O. Additionally, the presence of a proton source can supply additional thermodynamic driving force through the formation of H_2O. Several common adaptations of this general mechanistic picture are shown in Scheme 1.1 in Chapter 1.

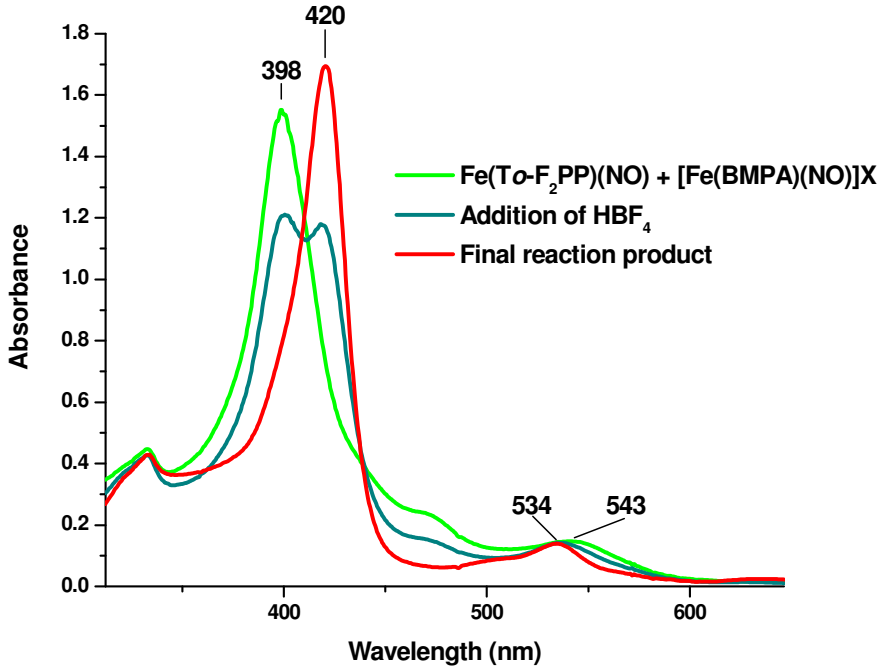

Figure 4.2. Absorbance spectra recorded during the interaction of [Fe(T*o*-F_2PP)(NO)] and [Fe(BMPA-Pr)(NO)]X in the presence of HBF_4. The decomposition of the non-heme unit leads to non-productive reactivity with [Fe(T*o*-F_2PP)(NO)] to generate the observed product.

Unfortunately, as with the radical reactivity above, no reactivity is observed between [Fe(BMPA-Pr)(NO)]X or [Fe(TPA)(NO)(CH_3CN)](ClO_4)$_2$ with a

variety of five- and six-coordinate heme nitrosyls; including [Fe(TPP)(NO)], [Fe(T*o*-F_2PP)(NO)], and [Fe(BzIM)(NO)]. Under weakly acidic conditions there remains no reactivity. However, under strongly acidic conditions, such as in the presence of HBF_4, a new heme species is generated in solution (see Figure 4.2). Further analysis has revealed that this reactivity is a result of decomposition of the non-heme species under acidic conditions. The BMPA-Pr ligand is susceptible to protonation at both the carboxylate and pyridine positions, resulting in either the release of free iron or the formation of a reactive low-coordinate iron center. Additionally, headspace gas analysis does not indicate N_2O formation, ruling out NO reduction even under highly acidic conditions. All attempts to isolate the new heme product have been unsuccessful.

In light of these results, it is likely that the electronic structure of ferrous heme nitrosyls and S = 3/2 high-spin non-heme iron nitrosyls are not conducive to NO/NO coupling. Even though the ground state electronic structure of S = 3/2 non-heme iron nitrosyls is best described as high-spin Fe(III) antiferromagnetically coupled to triplet NO^-,[14-15] strong π-donation from NO^- back to the non-heme iron leads to depletion of spin-density on the NO ligand; resulting in vibrational properties more similar to Fe(II)-NO●. This is also evidenced by our results which show that the Fe(III)-NO^- electronic structure of high-spin non-heme iron nitrosyls still does not promote NO reduction under the conditions detailed within this chapter. This is true at least in the case of non-covalently linked heme/non-heme iron nitrosyls in solution.

One intriguing mechanistic possibility involves the formation of a reduced $\{FeNO\}^8$ non-heme iron nitrosyl, which potentially gains an extra electron from the low redox potential heme b_3 within the active site of NorBC.[16] The classic Enemark-Feltham notation $\{FeNO\}^n$ is used here to denoted the electron occupancy of the Fe-NO unit where n = the total number of iron d and NO π* electrons.[17] Generation of a reduced non-heme center means that both electrons needed for the reduction of two equivalents of NO to N_2O are contained at the non-heme Fe_B site. The heme site would then act as an electron transfer center and may potentially still bind NO leading to a *trans*-type mechanism in which non-heme Fe(II)-NO^- and heme Fe(III)-NO undergo redox-type coupling. In an alternative scenario, an $\{FeNO\}^8$ non-heme iron nitrosyl could be envisioned as an intermediate in a *cis* Fe_B-type mechanism. Here, the heme b_3 center acts only as an electron transfer site facilitating formation of a non-heme Fe(II)-NO^- complex. This non-heme nitroxyl intermediate then interacts directly with a

second equivalent of NO forming a transient hyponitrite species which decomposes to yield N_2O and the di-ferric oxo-bridged resting state of the enzyme. Initial work on the exploration of these scenarios through the use of model complexes is presented below.

Reduction of Non-Heme Iron Nitrosyls in an Effort to Produce N_2O

Based on the observations outlined above, it seems unlikely that NorBC achieves NO reduction through the coupling of $\{FeNO\}^7$ heme and non-heme iron nitrosyls. Therefore, initial attempts have been made to determine the reactivity of one electron reduced $\{FeNO\}^8$ non-heme iron nitroxyls. These reduced non-heme iron nitrosyls may play an important role in the conversion of NO into N_2O by NorBC. Here, formation of a $\{Fe\text{-}NO\}^8$ species (formally $Fe^{II}\text{-}NO^-$), which is primed with both electrons necessary for the two electron reduction of NO, could be mediated by reduction of a proposed Fe_B-NO intermediate. The formation of such a non-heme Fe_B nitroxyl intermediate could be facilitated by electron transfer from the nearby ferrous heme b_3 center within the NorBC active site. It is possible that the heme site could facilitate electron transfer to a catalytically active Fe_B center as the redox potential of the heme b_3 center has been proposed to be ~ 250 mV below that of the Fe_B site.[16] Recent EPR studies on NorBC purified from *Pseudomonas nautica* also indicate that the heme b_3 center may in fact be low-spin in both the ferric and ferrous states, and thus promote binding of the initial NO molecule at the non-heme Fe_B site.[18] Upon generation of a non-heme $\{Fe_B\text{-}NO\}^8$ species, a second molecule of NO is required to form the necessary N-N bond for the production of N_2O, leaving behind a diferric oxo-bridged active site after N_2O release. This second NO molecule could be supplied as free NO entering the catalytic cycle in a *cis*-type mechanism or in the form of a ferric heme b_3 nitrosyl in accordance with a modified *trans* mechanism. Formation of a non-heme $\{Fe\text{-}NO\}^8$ species is therefore consistent with both the *cis* and *trans* mechanisms proposed for NorBC. As the basic properties and reactivity of high-spin $\{Fe\text{-}NO\}^8$ non-heme iron nitroxyls have not yet been established in the literature, these potentially important complexes garner further investigation.[19]

In order to probe the potential stability of the product of one-electron reduction of **1-X**, cyclic voltammograms were recorded on the [Fe(BMPA-Pr)(NO)]X series of complexes. These data show limited reversibility when X = Cl or ClO_4 for one-electron reduction. However, [Fe(BMPA-Pr)(NO)]OTf (**1-OTf)** displays a

quasi-reversible cyclic voltammogram which indicates potential stability of the $\{FeNO\}^8$ analog (see Figure 4.3). The lack of reversible features when X = Cl or ClO_4 likely indicates instability of the reduced form, resulting in rapid decomposition. All CV measurements were taken in organic and aqueous

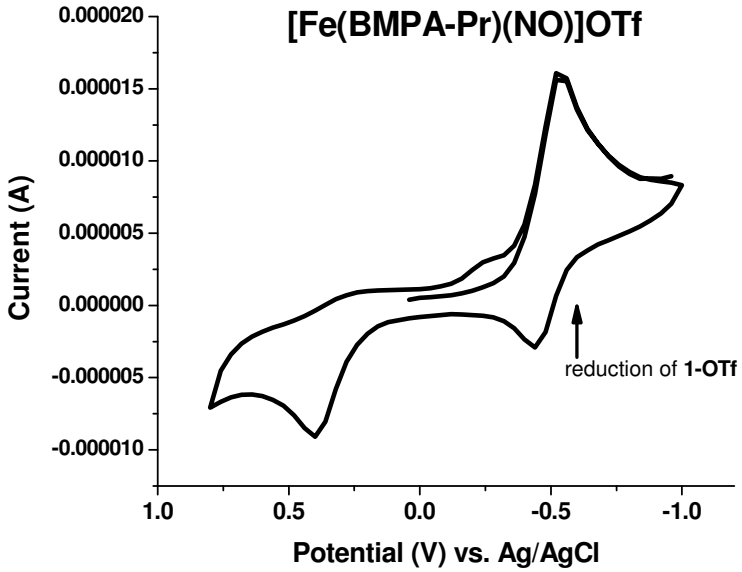

Figure 4.3. CV of **1-OTf** recorded in CH_3CN. A quasi-reversible feature is observed near -500 mV vs. Ag/AgCl and potentially represents formation of a $\{FeNO\}^8$ non-heme iron nitrosyl.

media. Table 3.1 (in Chapter 3) shows the relevant redox processes observed. Most notably, **1-OTf** and **1-ClO_4** reduce at -290 and -296 mV in CH_3CN compared to -565 and -585 mV in H_2O, respectively versus SHE. However, only **1-OTf** displays quasi-reversible redox properties.

It is of interest to note that dissolving [Fe(BMPA-Pr)(NO)]X in water likely results in the same $[Fe(BMPA\text{-}Pr)(NO)(H_2O)]^+$ species regardless of the counter ion. Solution IR and CV data indicate nearly identical spectroscopic features for these compounds which is indicative of H_2O binding in place of the counter ion when X = Cl. For the hexameric complexes where X = ClO_4 or OTf, hydrogen bonding between water molecules and the carboxylate moiety of BMPA-Pr likely disrupts bridging of this moiety resulting in monomeric water-bound species in solution. As shown in Figure 4.4, a common 1781 cm^{-1} ν(N-O) stretching frequency is observed for **1-X** in D_2O solution. EPR data presented in Chapter 3 also show disruption of intramolecular coupling effects related to the metallacrown hexamers **1-OTf** and **1-ClO_4** in aqueous solution; indicative of a monomeric $\{FeNO\}^7$ species.

The one electron reduced form of **1-OTf** has been studied by both absorption and infrared spectroscopy. Chemical reduction with KC_8 results in majority conversion to a new species showing a predominant 395 nm feature in the absorption spectrum (see Figure 4.5). The spectral changes are not consistent with known low-spin $\{FeNO\}^8$ complexes which typically show new absorbance features between 450 – 650 nm.[20-21] Comparison to high-spin non-heme $\{Fe\text{-}NO\}^8$ cannot be made as characterization of these species is currently lacking in the literature. More insight can be gained from infrared spectroscopy where reduction of **1-OTf** with KC_8 leads to the appearance of two ν(N-O) stretching features. Spectra recorded for both chemical (KC_8) and electrochemical reduced products show similar features with $^{15}N^{18}O$-sensitive bands at 1693 and 1636 cm^{-1} (see Figure 4.6). These vibrational properties argue again what is predicted for a non-heme $\{Fe\text{-}NO\}^8$ species. Here, DFT calculations (BP86/TZVP) predict an iron-centered reduction leading to a relatively high ν(N-O) frequency for the DFT model $[Fe(BMPA\text{-}Pr)(NO)(Cl)]^-$ at 1599 cm^{-1} (*vide infra*).

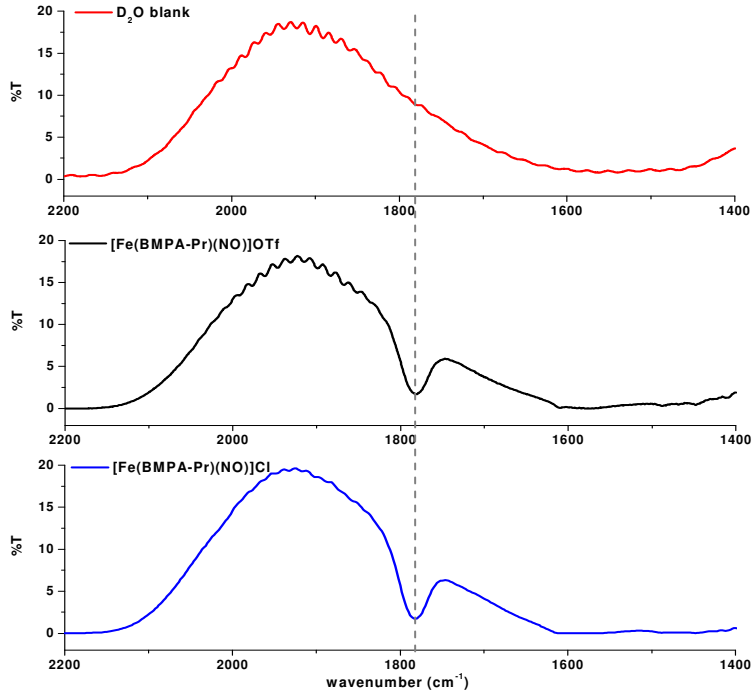

Figure 4.4. Solution IR spectra of **1-Cl** and **1-OTf** taken in D_2O. In aqueous media all **1-X** species show identical ν(N-O) stretching features, indicating formation of a common monomeric water-bound complex.

Interestingly, the observed spectroscopic data can be rationalized by formation of a $\{Fe(NO)_2\}^{10}$ dinitrosyliron complex (DNIC) rather than the desired $\{FeNO\}^8$ mononitrosyl adduct.[22-23] Similar $\{Fe(NO)_2\}^{10}$ complexes with overall neutral charge have been reported in the literature and typically

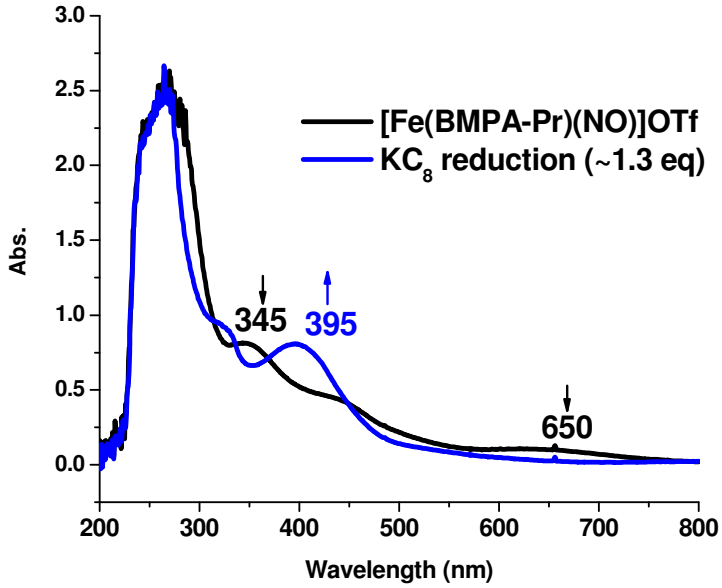

Figure 4.5. Absorbance overlay of **1-OTf** and its reduction product taken in CH_2Cl_2. Similar features are observed upon electrochemical reduction.

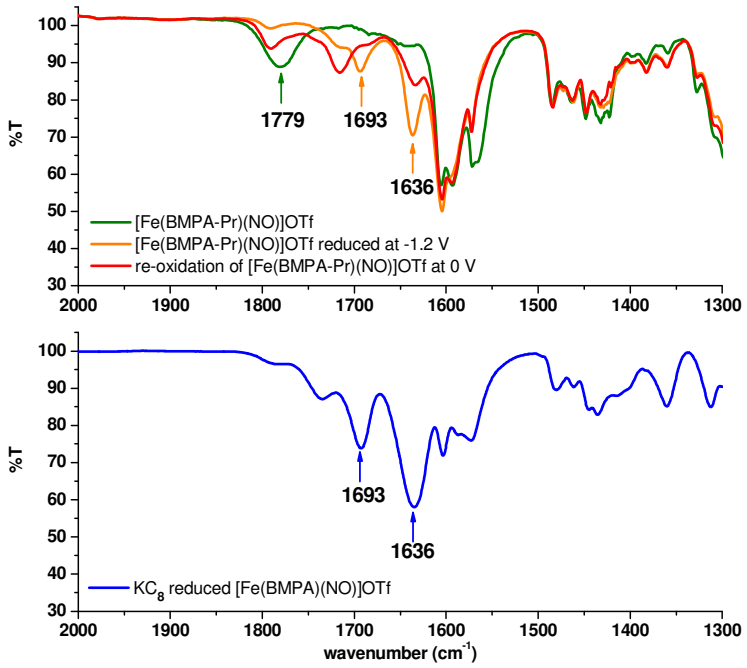

Figure 4.6. Spectroelectrochemical reduction of [Fe(BMPA-Pr)(NO)]OTf in CH_2Cl_2 monitored by IR spectroscopy (top). The reduction of [Fe(BMPA-Pr)(NO)]OTf with KC_8 is shown for comparison (bottom).

display split ν(N-O) bands at 1673-1724 and 1616-1678 cm^{-1}.[23] The anionic $\{Fe(NO)_2\}^{10}$ complex $[Fe(NO)_2(Ar\text{-}nacnac)]^-$ reported by Lippard and coworkers displays lower ν(N-O) features at 1627 and 1569 cm^{-1}.[24] Therefore, reduction of **1-OTf** leads to formation of a DNIC with properties more similar to neutral $\{Fe(NO)_2\}^{10}$ complexes. This correlation can potentially be rationalized by dissociation of the carboxylate moiety in BMPA-Pr, leading to a neutral $Fe(NO)_2$ unit. Such a scenario is also consistent with the propensity of dinitrosyliron complexes to adopt a (pseudo)tetrahedral geometry about the iron center.[23-25] Further spectroscopic analysis is needed to confirm this possibility.

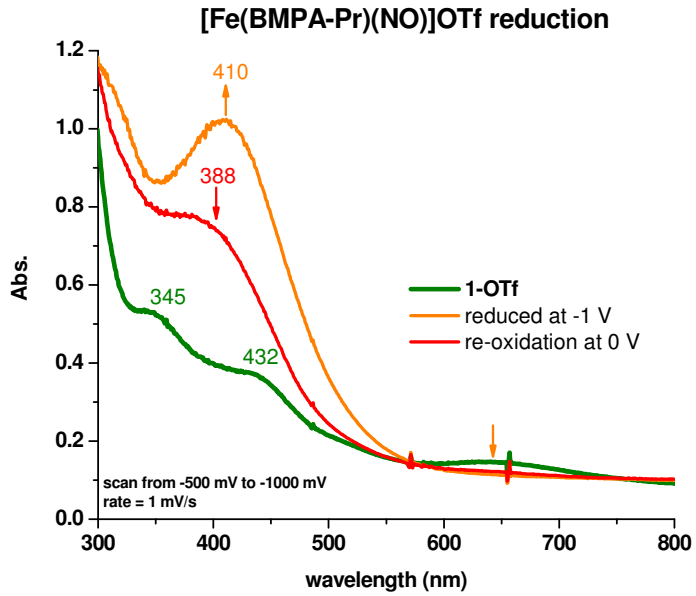

Figure 4.7. Spectroelectrochemical reduction of **1-OTf** in CH_3CN monitored by UV-visible absorption spectroscopy.

Re-oxidation of the obtained $\{Fe(NO)_2\}^{10}$ species at 0 V results in a shift of the two isotope-sensitive bands to 1791 and 1717 cm^{-1}, indicating oxidation of the DNIC species to $\{Fe(NO)_2\}^9$. The observed ν(N-O) frequencies fit well with reported vibrational properties of both cationic and neutral $\{Fe(NO)_2\}^9$ complexes which typically display ν(N-O) at 1734-1786 and 1695-1746 cm^{-1}.[23-24] As a final confirmation, NRVS spectroscopy was performed on the reduced ^{57}Fe-enriched analog of **1-OTf**. Here, two separate Fe-NO stretching vibrations are visible at 561 and 515 cm^{-1}, which is again consistent with DNIC formation based on comparison to vibrational parameters reported in the literature.[26] Additionally, EPR spectra recorded upon KC_8 reduction of **1-OTf** show a loss of the broad S = 3/2 signals at approximately g = 4 concomitant with partial

formation of a new g = 2 signal. This is consistent with the formation of an $\{Fe(NO)_2\}^9$ DNIC species which can be generated from the oxidation of EPR-silent $\{Fe(NO)_2\}^{10}$ analogs by atmospheric dioxygen.[23, 27]

Spectroelectrochemical absorption spectroscopy in which a solution **1-OTf** was reduced at -1 V was also employed. Here, reduction results in the appearance of a 410 nm feature which is stable during applied potential (see Figure 4.7). Importantly, reoxidation at 0 V does not return **1-OTf** but rather results in spectral features similar to that observed during KC_8 reduction. It is likely that the final KC_8-reduced product observed by UV-visible absorbance spectroscopy is a result of oxidation of an initially reduced (410 nm) species. Due to the low concentrations used in absorbance measurements, the presence of very small amounts of dioxygen can result in undesired oxidation. This is supported by our IR results (see above) where solutions of higher concentration do not suffer from oxidation by extraneous O_2, *vide infra*.

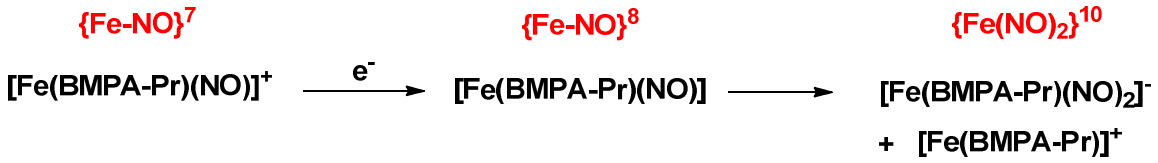

Scheme 4.2. Mechanistic scheme for the formation of a dinitrosyliron complex upon reduction of **1-X**.

Interestingly, no N_2O is detected upon reduction in the presence of an acid source. The mechanism of DNIC formation thus cannot involve loss of HNO during binding of the second NO equivalent, as has been proposed for biological systems in aqueous environments.[27] It is therefore likely that these complexes form via disproportionation of a transiently formed $\{FeNO\}^8$ species; resulting in an $\{Fe(NO)_2\}^{10}$ dinitrosyl and denitrosylated Fe(II) side product as shown in Scheme 4.2. A similar reaction has been reported using β-diketiminate ligated non-heme iron nitrosyls.[24] As an alternative mechanistic pathway, $\{Fe\text{-}NO\}^8$ can react with remaining $\{Fe\text{-}NO\}^7$ to generate a transient $\{Fe(NO)_2\}^9$ species along with an Fe(II) side product. Further reduction of this DNIC then yields the observed $\{Fe(NO)_2\}^{10}$ species. This scenario, however, is unlikely as reduction of **1-OTf** with low-equivalents of KC_8 yields vibrational features of the afore mentioned $\{Fe(NO)_2\}^{10}$ product (see Figure 4.6) and signals consistent with $\{Fe(NO)_2\}^9$ are only seen upon re-oxidation. In terms of NO reduction, the results detailed above point to the need for a more sterically hindered non-heme iron nitrosyl in order to stabilize the $\{FeNO\}^8$

state and prevent disproportionation, leading to DNIC formation. Sterically bulky ligands which inhibit binding of a second NO molecule could thus be envisioned to limit NO^- transfer which is a requirement for DNIC formation.

DFT Analysis of the Non-Heme {FeNO}^{8} Electronic Structure

Despite the fact that our non-heme iron nitrosyl model complexes tend towards DNIC formation following the reduction to the corresponding {FeNO}^{8} species, DFT calculations still allow for the prediction of experimental properties of high-spin {FeNO}^{8} non-heme iron nitrosyls. Here, *in silico* addition of a single electron to [Fe(BMPA-Pr)(NO)(Cl)] (**1-Cl**) resulting in $[Fe(BMPA\text{-}Pr)(NO)(Cl)]^-$ (**2-Cl**) has been probed using DFT calculations at the BP86/TZVP theory level. Comparison of the fully optimized geometries shows a shorter Fe-N(O) bond length and a slightly smaller Fe-N-O angle in **2-Cl** as compared to **1-Cl**. Table 4.1 lists all relevant bond lengths and angles for **1-Cl** and **2-Cl**. Frequency calculations performed on these model systems predict the ν(N-O) stretch at 1733 and 1599 cm^{-1} for **1-Cl** and **2-Cl**, respectively.

Table 4.1. DFT predicted geometric properties for **1-Cl** and **2-Cl**.

	1-Cl	**2-Cl**
DFT Predicted Parameters [Å, °]		
Fe-N(O)	1.74	1.72
Fe-N(pyridine)$_1$	2.28	2.23
Fe-N(pyridine)$_2$	2.30	2.08
Fe-N(amine)	2.33	2.33
Fe-O	1.98	2.14
Fe-Cl	2.32	2.48
Fe-N-O	153	149

The electronic structure of **1-Cl**, and high-spin non-heme iron nitrosyls in general, is best described as high-spin iron(III) antiferromagnetically coupled to NO^- (see Chapter 3). As a result, the one-electron reduction to give **2-Cl** would be expected to be iron-centered. Interestingly, DFT predicts a ν(N-O) stretching frequency which is intermediate between NO● and NO^-. In the case of **1-Cl**, it is known that strong π-donation from the singly-occupied π* orbitals of NO^- back to iron results in ν(N-O) features which more closely resemble NO● than NO^-. It is possible that a similar effect remains in the case of **2-Cl**. However, due to the increased electron density on iron, π* donation is reduced in **2-Cl** which results in an increase of electron density in the π* orbitals of NO, and correspondingly, a weaker N-O bond, and thus lower ν(N-O) frequency. Analysis of isodensity surface plots obtained from BP86/TZVP frequency calculations on **2-Cl** are in agreement with this

hypothesis. Firstly, the extra electron present in **2-Cl** occupies the d_{xy} orbital of iron, which now shows significant α and β electron density (see Figure 4.8, MO's α94 and β99). The decreased effective nuclear charge of iron in **2-Cl** limits β-spin donation from NO^-, as seen in a comparison of MO's β96 and β97 for **1-Cl** versus **2-Cl** (see Figure 4.8). For **2-Cl** both β96 and β97 display a comparatively higher percentage of NO π* character than iron d character. This results in increased occupation of the antibonding π* orbitals of NO, leading to a lower ν(N-O) frequency despite the fact that the reduction is in fact iron-centered.

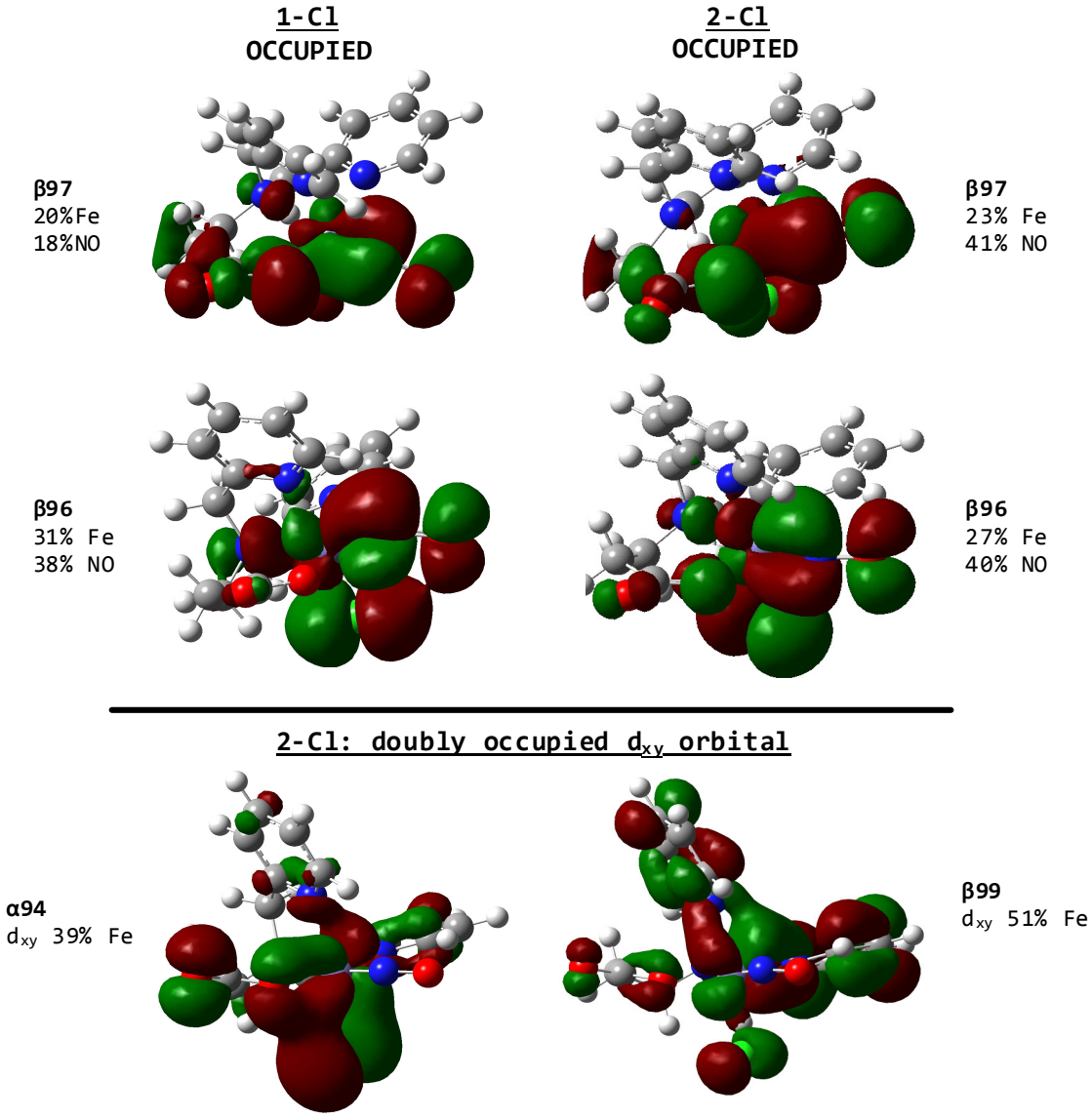

Figure 4.8. Isodensity surface plots of selected α-spin and β-spin MO's showing the interaction of Fe and NO^- in **1-Cl** and **2-Cl** (top). The α and β components of the doubly occupied iron d_{xy} orbital are shown (bottom). Calculated at the BP86/TZVP theory level.

4.2. Covalently Linked Heme/Non-Heme Models

The synthesis of a single covalently linked dinuclear iron complex which encompasses both heme and non-heme centers would represent a truly biomimetic framework for which to study the mechanism of NO reduction by NorBC. This strategy has been successfully employed in the case of cytochrome *c* oxidase (C*c*O) model complexes which contain both heme and copper coordination sites.[28-31] Additionally, a small number of complexes have also been synthesized as models for the NorBC active site.[2, 32-34] First and foremost, Collman and coworkers have developed a functional model complex, LFe^{II}/Fe^{II}, based on C*c*O model complexes in which the copper site has been substituted with iron.[34] As such, the coordination environment of the non-heme site contains only neutral N-donor ligands; where it is now known that the Fe_B site in NorBC is in fact ligated by a glutamate.[35] Although no crystal structure is available, spectroscopic analysis of this model system supports a *trans*-type mechanism in that NO appears to bind at both the heme and non-heme iron centers before reduction to N_2O.[36] While this represents a significant achievement, it is difficult to draw substantial mechanistic conclusions from these model studies as no crystal structure of this complex is available and the overall very low yield of the complex limits the ability to perform mechanistic studies. Interestingly, other synthetic heme/non-heme diiron models, such as the non-heme carboxylate containing models from Collman and coworkers as well as other diiron models from Karlin and coworkers, show no reactivity with respect to the reduction of NO gas.[32, 37-38] It is therefore our intention to develop a high-yield synthesis for a functional covalently-linked diiron heme/non-heme model complex which closely mimics the coordination environment of NorBC in order to probe the mechanism of NO reduction. Presented herein are the preliminary synthetic efforts directed at this aim.

The porphyrin moiety employed in all of the proposed heme/non-heme complexes is the hexafluorinated tri-(2,6-difluorophenyl)-(*ortho*-X-phenyl)porphyrin, where X represents the site of non-heme attachment. Two potential methods of non-heme attachment have been explored. The first strategy focuses on formation of an amide linkage off the *meta* position of one of the pyridine rings present in BMPA-Pr (see Chapter 3). This strategy is analogous to that employed for the imidazole-tethered complex BzIM, presented in Chapter 2.[9] An alternative, and more robust, approach utilizes an ether linkage in place of the amide presented above. Here, coupling of a hydroxylated BMPA-Pr ligand with an *ortho*-brominated phenyl ring of the

porphyrin ligand via the method of Williamson et. al. yields a highly stable ether linkage.[39] These general approaches could be applied to a variety of substituted heme ligands and numerous other pyridine-containing non-heme scaffolds. One enticing possibility is the covalent linkage of a non-heme moiety to an imidazole-tethered heme ligand, such as BzIM, to generate a biomimetic heme/non-heme complex which also incorporates the axial histidine found in NorBC.

Amide-Coupled Heme/Non-Heme Model Complexes

A general strategy for the synthesis of amide-coupled heme/non-heme complexes is outlined in Scheme 4.3. Current work in our laboratory has focused on the attachment of the carboxylate-containing non-heme ligand BMPA-Pr to a hexafluorinated porphyrin moiety, as shown in Scheme 4.3. Synthesis of the base porphyrin tri-(2,6-difluorophenyl)-(2-aminophenyl)porphyrin (**6**) has been previously reported.[40]

Beginning with the commercially available starting material pyridine-2,5-dicarboxylic acid (**1**), the chlorinated pyridine derivative (2-chloromethyl-5-carboxylic acid chloride)pyridine (**5**) can be synthesized in four steps. Esterification of **1** via *p*-toluenesulfonic acid yields the dimethylester dimethyl-pyridine-2,5-carboxylate (**2**) in 70% yield. The *para* methyl ester of **2** is susceptible to selective reduction by $NaBH_4$ at 0 °C to give the primary alcohol methyl-2-hydroxymethyl nicotinamide (**3**) in 70% yield. Installation of a halide in place of the alcohol can be accomplished via bromination (with PBr_3 or CBr_4) or chlorination (with $SOCl_2$) to yield methyl-2-halomethyl nicotinamide. However, these compounds suffer from lack of stability and readily convert to a bright red decomposition product. A more stable alternative route proceeds via NaOH de-esterification of the methyl ester to yield 6-hydroxymethyl nicotinic acid (**4**) in near quantitative yield. This species can then be efficiently di-chlorinated via reflux in $SOCl_2$ under inert atmosphere to give **5**. While **5** remains susceptible to decomposition, the installation of an acyl chloride moiety allows for rapid reaction with the amino-porphyrin **6**. Under anhydrous conditions, **6** readily couples with the acyl chloride on **5** to produce the 2-chloromethyl pyridine-substituted porphyrin **7** along with one equivalent of HCl. Due to protonation of the porphyrin core, no additional base is required for this reaction and the amide bond remains intact.

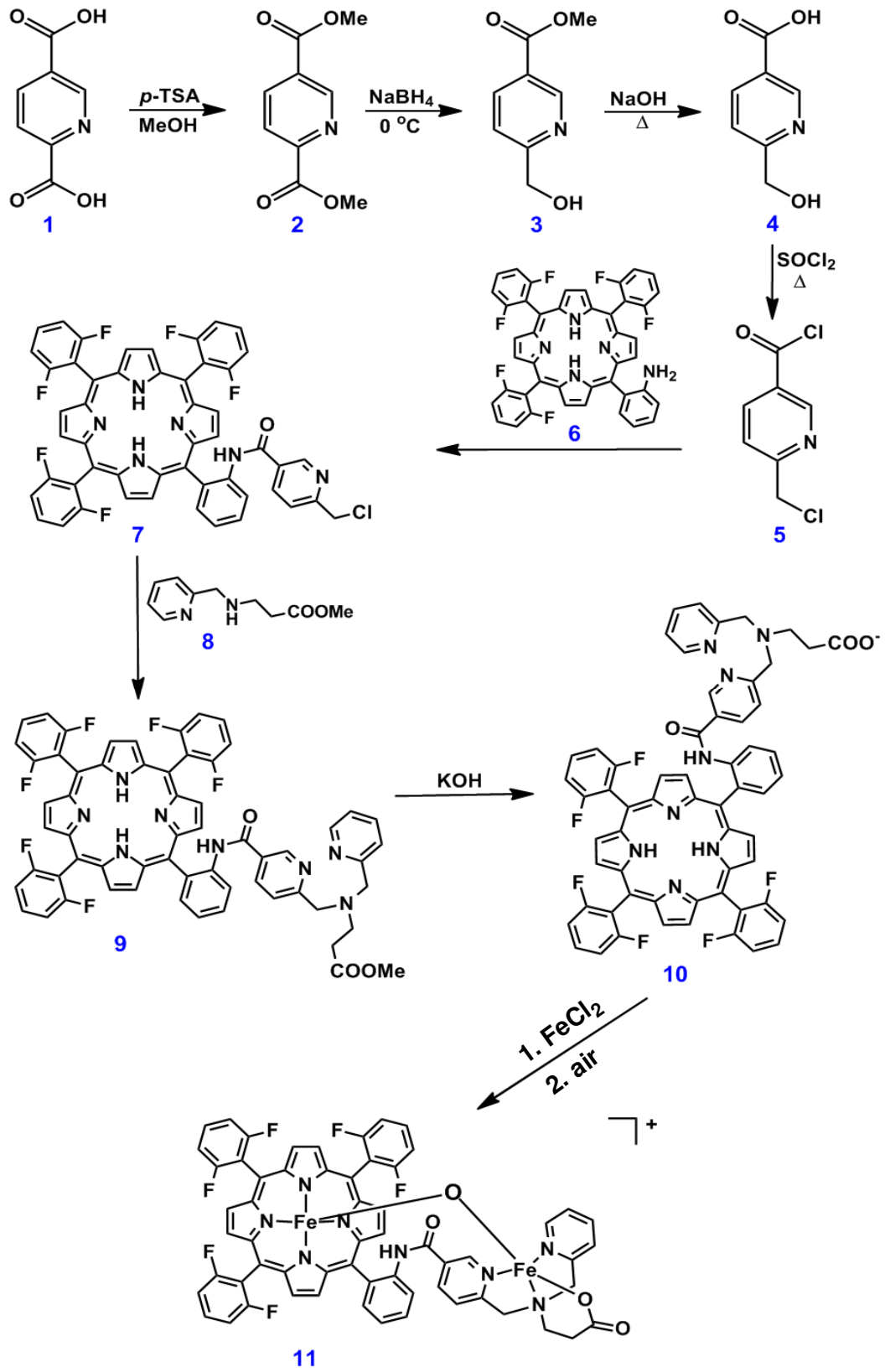

Scheme 4.3. Synthetic scheme for the synthesis of the amide-tethered heme/non-heme diiron complex **11**.

The remainder of the non-heme binding site is synthesized separately by the reductive amination of 2-pyridine carboxaldehyde with the hydrochloride salt of 3-amino propionic acid methyl ester. Under basic conditions the hydrochloride salt of 3-amino propionic acid methyl ester is deprotonated, leaving the primary amine able to couple with 2-pyridine carboxaldehyde to give the corresponding imine intermediate. Subsequent reduction with $NaBH_4$ then yields the desired product 2-aminomethyl-(N-methylpropionate)pyridine (**8**). Coupling of **8** with **7** is achieved by simple S_N^2 nucleophilic substitution in DMF resulting in the formation of F_6(BMPA-OMe)TPPH_2 (**9**) where BMPA-OMe represents the methyl ester of BMPA-Pr. Unfortunately, however, deprotection of the methyl ester is non-trivial. A 10% solution of 2M KOH in methanol and 90% dichloromethane is able to efficiently cleave the ester at room temperature over 24 hours. However, this method also results in significant decomposition of the amide bond which links the heme and non-heme component. As a result, typical yields for the formation of the linked heme/non-heme ligand F_6(BMPA-Pr)TPPH_2 (**10**) are in the range of 20-30%. Alternative conditions were also tried. However, these methods were either too weak to deprotect the methyl ester or resulted in decomposition of the product.

With the covalently linked heme/non-heme ligand **10** in hand, preliminary studies have been performed in regards to iron metallation, reduction, and NO binding. Metallation of **10** with $FeCl_2$, followed by exposure to atmosphere dioxygen results in the transient formation of the corresponding ferric chloride complex as a red/brown material. Addition of NaOH or prolonged exposure to atmospheric water vapor yields the orange diiron μ-oxo species [Fe(F_6[Fe(BMPA-Pr)]TPP)]O (**11**), as evidenced by mass spectroscopy (m/z = 1159). Such a result is encouraging as the formation of an oxo bridge indicates the two iron centers are held within close proximity of one another. In fact, the resting state of NorBC contains a similar μ-oxo bridged heme/non-heme structure in the enzyme active site.[35]

Absorbance measurements were used to monitor the reduction of **11** to what is presumed to be the corresponding di-ferrous state (see Figure 4.9). Here, both KC_8 and $Na_2S_2O_4$ have been shown to produce spectral changes consistent with the reduction of **11** generating a new product which is distinctly more red in color. Both methods result in a shift of the Soret band from 413 nm for the μ-oxo bridge to 435 nm. This reduction is also fully reversible upon exposure to atmospheric dioxygen resulting in the return to the diferric complex **11**. Most interesting is the ability of the reduced material to bind NO gas. Upon

addition of NO, the Soret band shifts immediately to 403 nm consistent with the formation of a ferrous heme nitrosyl. Due to the lack of sufficient material, no further tests were conducted and it is yet unclear whether the non-heme iron site is able to bind NO under these conditions.

Ether-Linked Heme/Non-Heme Model Complexes

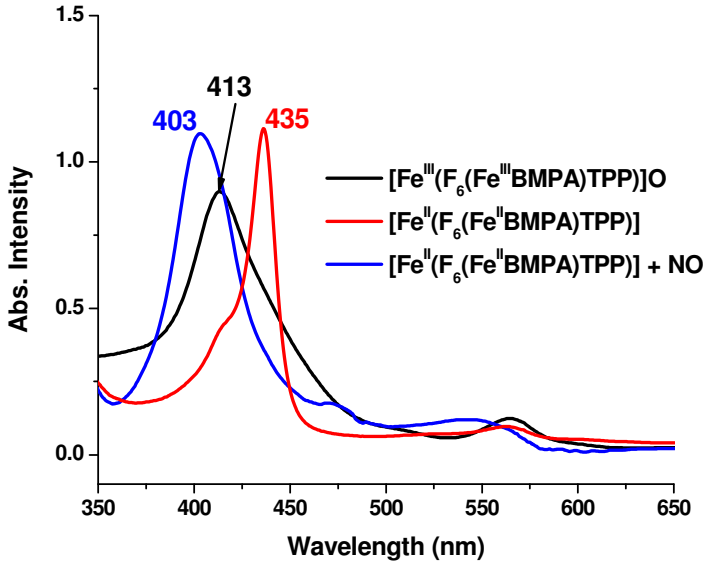

Figure 4.9. UV-visible absorbance spectra of [Fe^{III}(F$_6$(Fe^{III}BMPA)TPP)]O (**11**, blue) along with the reduced di-ferrous analog (red) and then resulting product of NO binding (black).

Due to the synthetic complications encountered when using a base-sensitive amide tether, an alternative synthetic route was developed. The introduction of a covalent ether linkage between the heme and the non-heme iron coordination sites represents a far more robust chemical tether. Here, tri-(2,6-difluorophenyl)-(*ortho*-X-phenyl)porphyrin where X = OH or Br will provide the base porphyrin ligand onto which the non-heme ligand will be attached. A synthetic scheme is presented for the attachment to the *ortho* pyridine position of the non-heme BMPA-Pr ligand (see Scheme 4.4).

Commercially available 2,6-dihydroxymethylpyridine (**12**) can be converted to the mono- and di-brominated products 2-hydroxymethyl-6-bromomethylpyridine (**13**) and 2,6-dibromomethylpyridine, respectively. While brominating reagents such as PBr_3 and CBr_4 almost exclusively favor formation of the di-bromo product, short reflux in 48% HBr affords **13** in ~ 30% yield. Nucleophilic

substitution of **13** with the secondary amine **8** then yields *ortho*-hydroxymethyl(BMPA-OMe) (**14**).

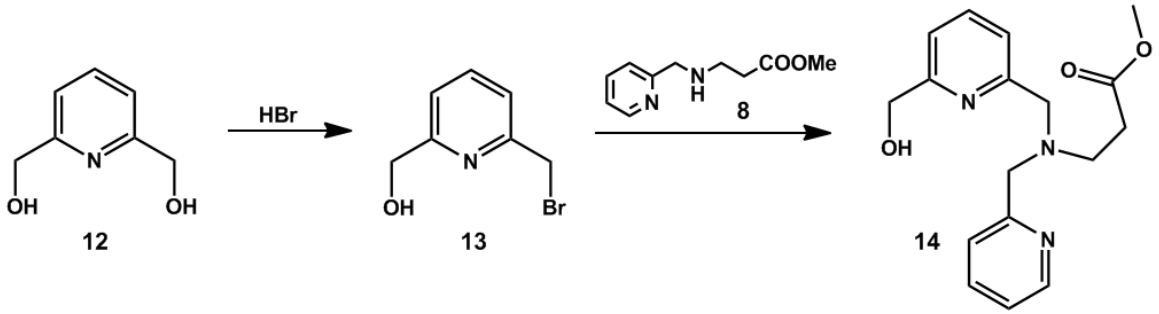

Scheme 4.4. Synthetic scheme for the synthesis of the hydroxylated non-heme ligand **14**.

The corresponding heme component, tri-(2,6-difluorophenyl)-(*ortho*-bromo-phenyl)porphyrin, has been designed to couple with the hydroxymethyl functionality on **14**. Preliminary results indicate the successful synthesis of this porphyrin. However, the major side product of this reaction, tetra-(2,6-diflurophenyl)porphyrin, is practically difficult to separate from the desired brominated porphyrin. As a result, it is proposed that bromination of **14** to yield *ortho*-bromomethyl(BMPA-OMe) followed by coupling to the hydroxylated porphhyin, tri-(2,6-difluorophenyl)-(*ortho*-hydroxy-phenyl)porphyrin, represents a more efficient strategy going forward.

Experimental

In general, reactions were performed applying inert gas (Schlenk) techniques. Preparation and handling of air sensitive materials was carried out under an argon atmosphere in an MBraun glovebox equipped with a circulating purifier (O_2, H_2O < 0.1 ppm). Compounds **1** and **12** were purchased from commercial suppliers and used without further purification. Infrared spectra were obtained from KBr disks on a Perkin-Elmer BX spectrometer. Proton magnetic resonance spectra were recorded on a Varian Inova 400 MHz and a Varian Mercury 300 MHz instrument. Electrochemical studies were carried out with a CH instruments CHI660C electrochemical workstation. Spectroelectrochemical measurements were obtained using a three-component system, consisting of a platinum mesh working electrode, a carbon felt auxiliary electrode, and a platinum wire reference electrode. Spectra were recorded in either 0.1 M tetrabutylammonium perchlorate in CH_3CN or 0.1 M KCl

in H_2O. Potentials were corrected to the SHE standard and the CH_3CN measurements were also corrected by measuring the ferrocenium/ferrocene couple under the same conditions (+624 mV vs. SHE).

Dimethyl-pyridine-2,5-carboxylate (2). In a 250 ml round-bottom flask, 10 g pyridine-2,5-dicarboxylic acid was combined with 13.7 g *p*-toluenesulfonic acid monohydrate in 120 methanol. The solution was brought to reflux for 48 hrs. Upon cooling to room temperature the resulting off-white precipitate is collected and washed with sat. Na_2CO_3. The resulting slurry was extracted with 200 ml $CHCl_3$ and the organic layer was dried with Na_2SO_4, filtered, and evaporated under reduced pressure to yield a white powder. Yield: 7.92 g (68 %). ^{1}H-NMR (400 MHz, $CDCl_3$): 9.29 (s, 1H), 8.43 (d, 1H), 8.19 (d, 1H), 4.02 (s, 3H), 3.97 (s, 3H).

Methyl-2-hydroxymethyl nicotinamide (3). In a dry round-bottom flask under inert atmosphere, 1 g dimethyl pyridine-2,5-dicarboxylate was combined with 2.27 g $CaCl_2$ in a mixture of 11 ml anhydrous THF and 12 ml anhydrous ethanol. After stirring for 30 minutes the reaction was cooled to 0 °C in an ice bath and 486 mg of $NaBH_4$ was slowly added in several portions. The reaction was then allowed to stir at 0 °C for 4 hours under inert atmosphere. The reaction was warmed to room temperature taking care to vent the buildup of H_2 gas. Extraction with CH_2Cl_2 followed by subsequent drying with Na_2SO_4 and evaporation of the solvent yields a faint yellow solid. Yield: 610 mg (70 %). ^{1}H-NMR (400 MHz, $CDCl_3$): 9.14 (s, 1H), 8.27 (d, 1H), 7.33 (d, 1H), 4.81 (d, 2H), 3.93 (s, 3H).

6-hydroxymethyl nicotinic acid (4). In a round-bottom flask, 600 mg of methyl-2-hydroxymethyl nicotinamide was dissolved in 5 ml THF. A separate solution containing 430 mg NaOH in 5 ml H_2O was added and the two-phase solution was stirred at reflux for 2 hrs. At this point the aqueous layer was collected, acidified to pH = 3 with HCl, extracted with CH_2Cl_2, neutralized to pH = 7 with Na_2CO_3, and evaporated under reduced pressure to give an off white solid. The solid material was washed with DMF and dried thoroughly under vacuum to give 1.6 g of a white solid (mix of 1 g NaCl with 600 mg **4**). The material was used without further purification. ^{1}H-NMR (400 MHz, D_2O): 8.73 (s, 1H), 8.01 (d, 1H), 7.41 (d, 1H).

(2-chloromethyl-5-carboxylic acid chloride)pyridine (5). In a dry round-bottom flask under inert atmosphere, 100 mg 6-hydroxymethyl nicotinic acid was combined with 3 ml anhydrous/ air-free CH_2Cl_2 and the resulting suspension was brought to reflux under inert atmosphere. 0.2 ml of freshly distilled $SOCl_2$ was added via syringe and the reaction was allowed to stir at reflux for 1 hr. At this point the material takes on a red color and the solvent/$SOCl_2$ is removed under reduced pressure. The dark red product is used immediately in the synthesis of **7** to avoid further decomposition.

Tri-(2,6-difluorophenyl)-(2-aminophenyl)porphyrin (6). Prepared via previously published procedures.[29]

(7). Under inert/anhydrous conditions, 38 mg of **6** was dissolved in 7 ml of dry/air-free CH_2Cl_2. The freshly prepared **5** was dissolved in 3 ml dry/air-free CH_2Cl_2 and added slowly via syringe to the solution of **6**. Upon addition the solution turns slowly from purple to green and is allowed to stir for 1 -24 hrs. until TLC (silica, CH_2Cl_2) shows no remaining **6**. The reaction is then diluted with 15 ml CH_2Cl_2, washed with sat. $NaHCO_3$, washed with H_2O, dried with Na_2SO_4, filtered, and evaporated under reduced pressure to yield a purple solid. Purified by column chromatography (silica) eluted with CH_2Cl_2 followed by addition of 2% methanol to elute the desired product. Yield: 30 mg (66 %). ^{1}H-NMR (400 MHz, CD_2Cl_2): 8.83 (m, 8H), 8.19 (s, 1H), 8.12 (d, 1H), 7.86 (t, 1H), 7.75 (m, 3H), 7.59 (m, 2H), 7.38 (m, 6H), 6.40 (d, 1H), 6.23 (d, 1H), 4.10 (s, 2H), -2.74 (s, 2H) LCT-MS: m/z = 891 (mass + H).

2-aminomethyl-(N-methylpropionate)pyridine (8). A mixture of 3.1 g 3-amino propionic acid methyl ester hydrochloride with 6.2 ml triethylamine in 17 ml methanol was slowly added via addition funnel (15-20 min.) to 2.38 g 2-pyridine carboxaldehyde in 40 ml methanol. The resulting orange solution was allowed to stir at room temperature for 8 hrs. At this point the reaction was set on ice and 1.7 g of $NaBH_4$ was added very slowly in several portions. The resulting cloudy solution was allowed to stir for 1 hr. before filtration to remove the undesired precipitate. The remaining solution was evaporated under reduced pressure and the residue was extracted with 80 ml CH_2Cl_2. Rotary evaporation of the organic extract gave **8** as a thick orange gel. Accurate mass could not be determined due to presence of solvent in the gel. ^{1}H-NMR (400 MHz, $CDCl_3$): 8.51 (d, 1H), 7.60 (t, 1H), 7.27 (d, 1H), 7.11 (t, 1H), 3.88 (s, 2H), 3.65 (s, 3H), 2.90 (t, 2H), 2.53 (t, 2H).

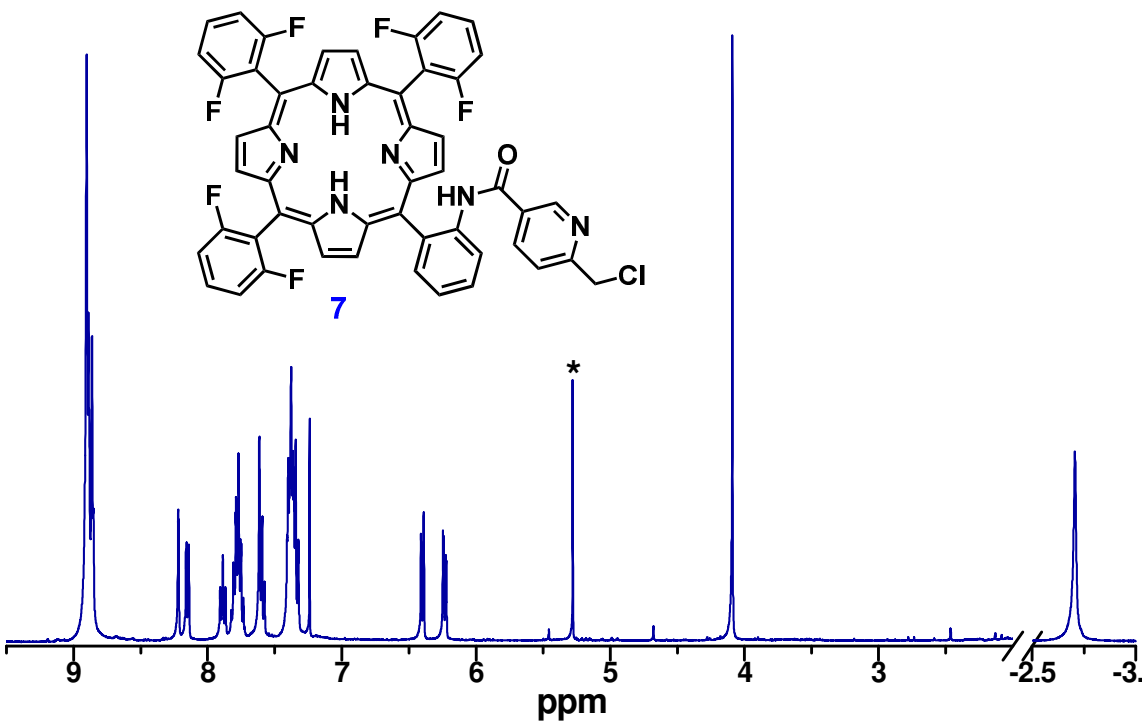

Figure 4.10. ^{1}H-NMR spectrum of **7** showing attachment of chloromethylpyridine moiety. Exact peak positions are given above in the experimental.

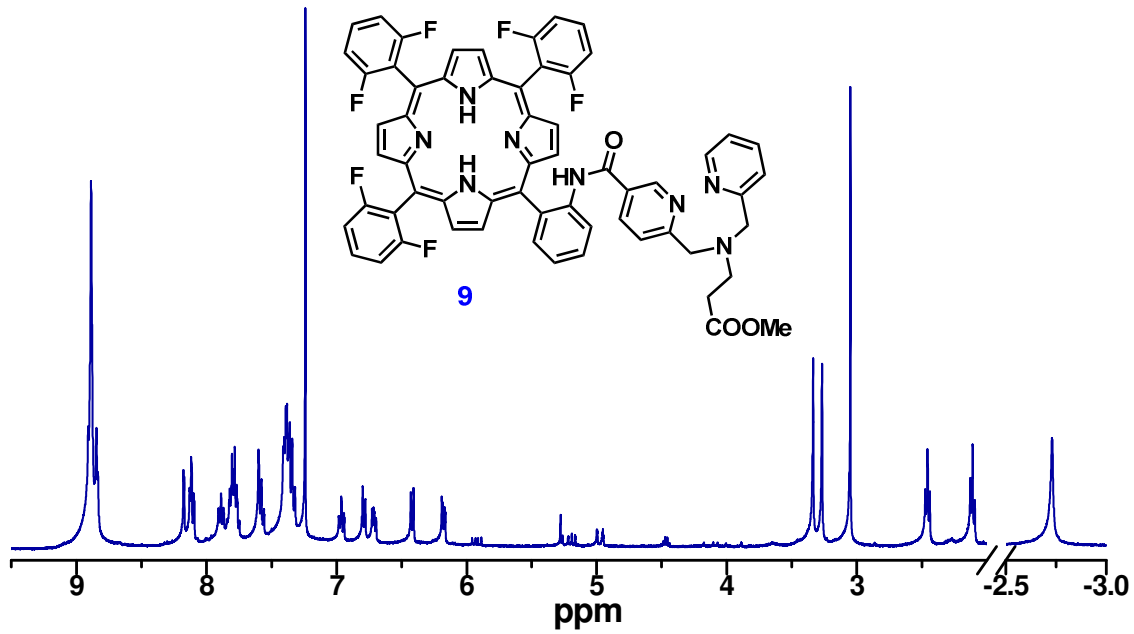

Figure 4.11. ^{1}H-NMR spectrum of **9** showing attachment of the BMPA-OMe non-heme binding site. New features can be seen between 6.5 and 7 ppm corresponding to the new pyridine ring, as well as new methylene proton features between 3 and 3.5 ppm.

(9). In a small round-bottom flask, 20 mg **7** was dissolved in 3 ml DMF. A large excess (65 mg) of **8** was then added and the reaction was allowed to stir at room temperature for 4 days. The solvent was removed under reduced pressure. Purified via column chromatography (silica) eluted with 3 % methanol in CH_2Cl_2. Yield: ~90 %. ^{1}H-NMR (400 MHz, $CDCl_3$): 8.88 (m, 8H), 8.18 (s, 1H), 8.12 (t, 1H), 7.89 (t, 1H), 7.78 (m, 3H), 7.58 (m, 2H), 7.36 (m, 6H), 6.96 (t, 1H), 6.79 (d, 1H), 6.72 (t, 1H), 6.42 (d, 1H), 6.18 (d, 1H), 3.34 (s, 2H), 3.27 (s, 2H), 3.05 (s, 3H), 2.46 (t, 2H), 2.11 (t, 2H), -2.70 (s, 2H) LCT-MS: m/z = 1049 (mass + H) and 1071 (mass + Na).

(10). A solution of 20 mg KOH in 0.2 ml methanol was diluted to 2 ml with CH_2Cl_2 and used to dissolve the material obtained from **9**. The resulting solution was stirred at room temperature for 24 hrs. before dilution with CH_2Cl_2, washing with H_2O, washing with dilute HCl, washing again with H_2O, drying with Na_2SO_4, and rotary evaporation. The obtained crude purple solid was purified via column chromatography (silica) eluting with CH_2Cl_2 followed by increments of 5 % and 10 % methanol. With 10 % methanol a broad streaky band is eluted which is the desired product **10**. Elution at 5 % give a decomposition product in which the amide tether has been cleaved.

(11). A small ~3 mg sample of **10** was dissolved in 1.5 ml of dry/air-free methanol under inert atmosphere. 10 mg anhydrous $FeCl_2$ was added and the reaction was brought to reflux under inert atmosphere for 3 hrs. After this point the reaction was exposed to air and the methanol was allowed to evaporate. The residue was dissolved in CH_2Cl_2 and filtered to remove any insoluble material. The organic layer was then washed with H_2O to remove excess $FeCl_2$. Following drying with Na_2SO_4, rotary evaporation of the solvent left a deep red/orange solid. Material can be crystallized slowly from CH_2Cl_2/pentane however no x-ray quality crystals have been obtained. LCT-MS: m/z = 1159. UV-vis: Soret = 413 nm, Q_v = 564 nm.

2-hydroxymethyl-6-bromomethylpyridine (13). To a round-bottom flask containing 1.02 g 2,6 dihydroxymethyl pyridine was added 10 ml of 48 % HBr. The solution was brought to reflux for 1 hr. After this time the reaction was cooled to 0 °C in an ice bath and taken to a basic pH with 10 ml of 30 % NaOH. The solution was extracted twice with CH_2Cl_2, dried with Na_2SO_4, filtered, and evaporated under reduced pressure to yield an orange oil. Purification by column chromatography (silica) eluted with CH_2Cl_2 to remove 2,6-dibromopyridine

(R_f = 0.45) followed by diethylether to elute **13** (R_f = 0.53). Rotary evaporation yields a white solid. Yield: 390 mg (26 %). ^{1}H-NMR (400 MHz, $CDCl_3$): 7.71 (t, 1H), 7.37 (d, 1H), 7.18 (d, 1H), 4.78 (d, 2H), 4.56 (s, 2H), 3.74 (t, 1H).

***Ortho*-hydroxymethyl(BMPA-Ome) (14).** In a round-bottom flask, 200 mg **8** was dissolved in 2 ml DMF and combined with 0.35 ml disopropylethylamine. The resulting solution was stirred to combine and 200 mg **13** was added. The reaction was brought to 50 °C overnight. The reaction was diluted with H_2O, extracted with CH_2Cl_2. Elution through silica with CH_2Cl_2 followed by methanol yields **14** as a red oil with a DMF. ^{1}H-NMR (400 MHz, $CDCl_3$): 8.50 (d, 1H), 7.63 (m, 2H), 7.46 (d, 1H), 7.33 (d, 1H), 7.13 (t, 1H), 7.06 (d, 1H), 4.70 (s, 2H), 3.81 (s, 4H), 3.61 (s, 3H), 2.91 (t, 2H), 2.55 (t, 2H), 1.76 (s_{broad}, 1H).

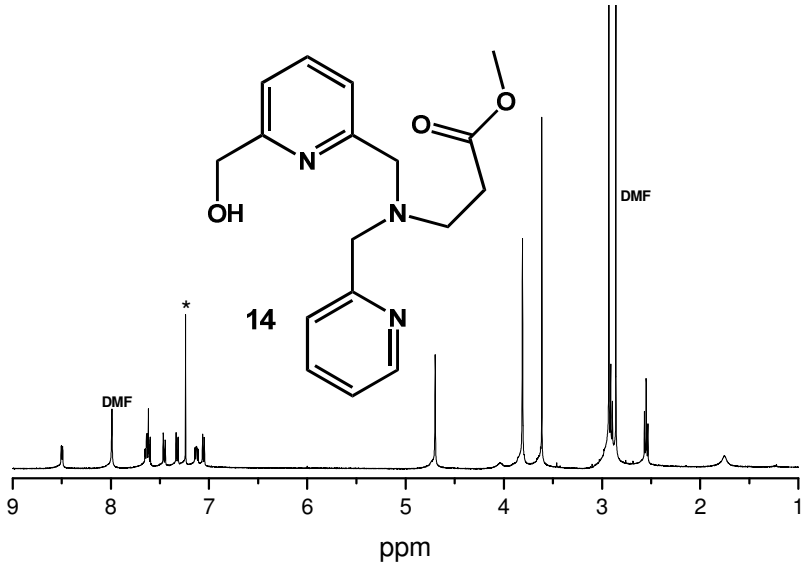

Figure 4.12. ^{1}H-NMR spectrum of *ortho*-hyrdoxymethyl(BMPA-OMe). Residual DMF is present in the crude product (red oil). See experimental text for assignment.

References

(1) Wang, J.; Schopfer, M. P.; Puiu, S. C.; Sarjeant, A. A. N.; Karlin, K. D., *Inorg. Chem.* **2010,** *49*, 1404.
(2) Schopfer, M. P.; Wang, J.; Karlin, K. D., *Inorg. Chem.* **2010,** *49*, 6267.
(3) Zumft, W. G., *J. Inorg. Biochem.* **2005,** *99*, 194.
(4) Moenne-Loccoz, P.; de Vries, S., *J. Am. Chem. Soc.* **1998,** *120*, 5147.
(5) Kumita, H.; Matsuura, K.; Hino, T.; Takahashi, S.; Hori, H.; Fukumori, Y.; Morishima, I.; Shiro, Y., *J. Biol. Chem.* **2004,** *279*, 55247.
(6) Lehnert, N.; Berto, T. C.; Galinato, M. G. I.; Goodrich, L. E., In *The Handbook of Porphyrin Science*, Kadish, K. M.; Smith, K. M.; Guilard, R., Eds. World Scientific: Singapore, 2011; Vol. 14, pp 1-247.
(7) Praneeth, V. K. K.; Neese, F.; Lehnert, N., *Inorg. Chem.* **2005,** *44*, 2570.
(8) Praneeth, V. K. K.; Nather, C.; Peters, G.; Lehnert, N., *Inorg. Chem.* **2006,** *45*, 2795.
(9) Berto, T. C.; Praneeth, V. K. K.; Goodrich, L. E.; Lehnert, N., *J. Am. Chem. Soc.* **2009,** *131*, 17116.
(10) McCandlish, E.; Miksztal, A. R.; Nappa, M.; Sprenger, A. Q.; Valentine, J. S.; Stong, J. D.; Spiro, T. G., *J. Am. Chem. Soc.* **1980,** *102*, 4268.
(11) Jourd'heuil, D.; Jourd'heuil, F. L.; Kutchukian, P. S.; Musah, R. A.; Wink, D. A.; Grisham, M. B., *J. Biol. Chem.* **2001,** *276*, 28799.
(12) Schopfer, M. P.; Mondal, B.; Lee, D.-H.; Sarjeant, A. A. N.; Karlin, K. D., *J. Am. Chem. Soc.* **2009,** *131*, 11304.
(13) Nasri, H.; Ellison, M. K.; Krebs, C.; Huynh, B. H.; Scheidt, W. R., *J. Am. Chem. Soc.* **2000,** *122*, 10795.
(14) Brown, C. A.; Pavlosky, M. A.; Westre, T. E.; Zhang, Y.; Hedman, B.; Hodgson, K. O.; Solomon, E. I., *J. Am. Chem. Soc.* **1995,** *117*, 715.
(15) Zhang, Y.; Pavlosky, M. A.; Brown, C. A.; Westre, T. E.; Hedman, B.; Hodgson, K. O.; Solomon, E. I., *J. Am. Chem. Soc.* **1992,** *114*, 9189.
(16) Gronberg, K. L. C.; Roldan, M. D.; Prior, L.; Butland, G.; Cheesman, M. R.; Richardson, D. J.; Spiro, T. G.; Thomson, A. J.; Watmough, N. J., *Biochemistry* **1999,** *38*, 13780.
(17) Enemark, J. H.; Feltham, R. D., *Coord. Chem. Rev.* **1974,** *13*, 339.
(18) Timoteo, C. G.; Pereira, A. S.; Martins, C. E.; Naik, S. G.; Duarte, A. G.; Moura, J. J. G.; Tavares, P.; Huynh, B. H.; Moura, I., *Biochemistry* **2011,** *50*, 4251.
(19) Berto, T. C.; Speelman, A. L.; Zhang, S.; Lehnert, N., *Coord. Chem. Rev.* **2012,** *In Press*.
(20) Garcia Serres, R.; Grapperhaus, C. A.; Bothe, E.; Bill, E.; Weyhermuller, T.; Neese, F.; Wieghardt, K., *J. Am. Chem. Soc.* **2004,** *126*, 5138.
(21) Patra, A. K.; Dube, K. S.; Sanders, B. C.; Papaefthymiou, G. C.; Conradie, J.; Ghosh, A.; Harrop, T. C., *Chem. Sci.* **2012,** *3*, 364.
(22) Butler, A. R.; Megson, I. L., *Chem. Rev.* **2002,** *102*, 1155.
(23) Hung, M.-C.; Tsai, M.-C.; Lee, G.-H.; Liaw, W.-F., *Inorg. Chem.* **2006,** *45*, 6041.
(24) Tonzetich, Z. J.; Heroguel, F.; Do, L. H.; Lippard, S. J., *Inorg. Chem.* **2011,** *50*, 1570.
(25) Tran, N. G.; Kalyvas, H.; Skodje, K. M.; Hayashi, T.; Moenne-Loccoz, P.; Callan, P. E.; Shearer, J.; Kirschenbaum, L. J.; Kim, E., *J. Am. Chem. Soc.* **2011,** *133*, 1184.
(26) Tonzetich, Z. J.; Wang, H.; Mitra, D.; Tinberg, C. E.; Do, L. H.; Jenney, F. E., Jr.; Adams, M. W. W.; Cramer, S. P.; Lippard, S. J., *J. Am. Chem. Soc.* **2010,** *132*, 6914.

(27) Vanin, A. F.; Poltorakov, A. P.; Mikoyan, V. D.; Kubrina, L. N.; Burbaev, D. S., *Nitric Oxide* **2010,** *23*, 136.
(28) Collman, J. P.; Devaraj, N. K.; Decreau, R. A.; Yang, Y.; Yan, Y.-L.; Ebina, W.; Eberspacher, T. A.; Chidsey, C. E. D., *Science* **2007,** *315*, 1565.
(29) Kim, E.; Shearer, J.; Lu, S.; Moenne-Loccoz, P.; Helton, M. E.; Kaderli, S.; Zuberbuhler, A. D.; Karlin, K. D., *J. Am. Chem. Soc.* **2004,** *126*, 12716.
(30) Naruta, Y.; Sasaki, T.; Tani, F.; Tachi, Y.; Kawato, N.; Nakamura, N., *J. Inorg. Biochem.* **2001,** *83*, 239.
(31) Kim, E.; Chufan, E. E.; Kamaraj, K.; Karlin, K. D., *Chem. Rev.* **2004,** *104*, 1077.
(32) Wasser, I. M.; Huang, H.-W.; Moenne-Loccoz, P.; Karlin, K. D., *J. Am. Chem. Soc.* **2005,** *127*, 3310.
(33) Collman, J. P.; Dey, A.; Yang, Y.; Decreau, R. A.; Ohta, T.; Solomon, E. I., *J. Am. Chem. Soc.* **2008,** *130*, 16498.
(34) Collman, J. P.; Yang, Y.; Dey, A.; Decreau, R. A.; Ghosh, S.; Ohta, T.; Solomon, E. I., *Proc. Natl. Acad. Sci. USA* **2008,** *105*, 15660.
(35) Hino, T.; Matsumoto, Y.; Nagano, S.; Sugimoto, H.; Fukumori, Y.; Murata, T.; Iwata, S.; Shiro, Y., *Science* **2010,** *330*, 1666.
(36) Collman, J. P.; Dey, A.; Yang, Y.; Decreau, R. A.; Ohta, T.; Solomon, E. I., *J. Am. Chem. Soc.* **2008,** *130*, 16498.
(37) Collman, J. P.; Yan, Y.-L.; Lei, J.; Dinolfo, P. H., *Inorg. Chem.* **2006,** *45*, 7581.
(38) Collman, J. P.; Yang, Y.; Decreau, R. A., *Org. Lett.* **2007,** *9*, 2855.
(39) Martens, C. F.; Murthy, N. N.; Obias, H. V.; Karlin, K. D., *Chem. Commun.* **1996**, 629.
(40) Kopf, M.-A.; Neuhold, Y.-M.; Zuberbuhler, A. D.; Karlin, K. D., *Inorg. Chem.* **1999,** *38*, 3093.

Chapter 5

Modeling the N_2O_2 Intermediate of NorBC

The mechanism of NO reduction within the diiron heme/non-heme active site of NorBC is currently debated within the literature (see Chapter 1).[1-4] One likely intermediate is a bridging hyponitrite complex where $N_2O_2^{2-}$ is bound between the two ferric iron centers within the enzyme.[1-2, 5-6] This species is proposed to form via radical-type N-N bond formation. In order to study the properties of such an intermediate, the model complex $[Fe(OEP)]_2(\mu\text{-}N_2O_2)$ has been synthesized by Richter-Addo and coworkers where two ferric octaethylporphyrin (OEP) units are bridged by the hyponitrite dianion.[7] This complex currently represents the only structurally-characterized di-ferric hyponitrite complex as a model for the key N-N bound intermediate in NorBC. Previous studies have proposed the formation of metal hyponitrite intermediates for both iron and copper complexes in the presence of excess NO.[8-9] However, these species are transient and have thus not been characterized. A bidentate hyponitrite Pt complex has also been crystallized.[10] However, such a complex does not serve as a biomimetic model. The hyponitrite dimer $[Fe(OEP)]_2(\mu\text{-}N_2O_2)$ thus offers a truly unique opportunity to study the properties of iron hyponitrite complexes and gain insight into their biological significance.

Due to the strong *trans* effect of NO, as discussed in Chapter 2, a radical-based N-N coupling mechanism would favor the formation of a six-coordinate (6C) ferrous heme nitrosyl; resulting in a additional radical character on NO which would facilitate formation of the corresponding hyponitrite intermediate. However, even 6C ferrous heme nitrosyls have been shown to be unreactive with respect to N-N coupling. Furthermore, these systems do not react with free NO; which has even greater radical character than ferrous heme nitrosyl complexes. Analysis of the electronic structure and reactivity of complexes which model the key hyponitrite intermediate proposed for NorBC offer an opportunity to gain insight into the mechanism of N-N coupling.

As previously reported by Richter-Addo and coworkers, the hyponitrite dimer rapidly decomposes in the presence of HCl to generate N_2O and H_2O along with [Fe(OEP)(Cl)].[7] New reactivity observed in our laboratory shows that $[Fe(OEP)]_2(\mu\text{-}N_2O_2)$ also undergoes thermal decomposition yield two equivalents of [Fe(OEP)(NO)], the reverse reaction to the proposed N-N bond formation step in NO reduction by NorBC. Given this interesting reactivity, a detailed characterization of the electronic structure and reactivity is warranted. Within this chapter is presented the characterization of $[Fe(OEP)]_2(\mu\text{-}N_2O_2)$ using a combination of magnetic circular dichroism (MCD), Nuclear Resonance Vibrational Spectroscopy (NRVS), SQUID magnetic measurements, DFT calculations, and kinetic studies.

5.1. Characterization of $\{[Fe(OEP)]_2(N_2O_2)\}$

In order to gain insight into the mechanism of NorBC from the model complex $[Fe(OEP)]_2(\mu\text{-}N_2O_2)$ it is first necessary to develop a clear understanding of the electronic structural properties of $[Fe(OEP)]_2(\mu\text{-}N_2O_2)$. In a previous publication, Richter-Addo and coworkers have already detailed the crystal structure of $[Fe(OEP)]_2(\mu\text{-}N_2O_2)$ and performed a cursory vibrational characterization along with preliminary DFT calculations on a S = 5 high-spin computational model of the complex.[7] Here, the DFT calculated atomic charges reveal a high degree of anionic character on the O-atom of hyponitrite. This is in agreement with observed reactivity in the presence of HCl where protonation of the hyponitrite O-atom leads to N_2O formation with generation

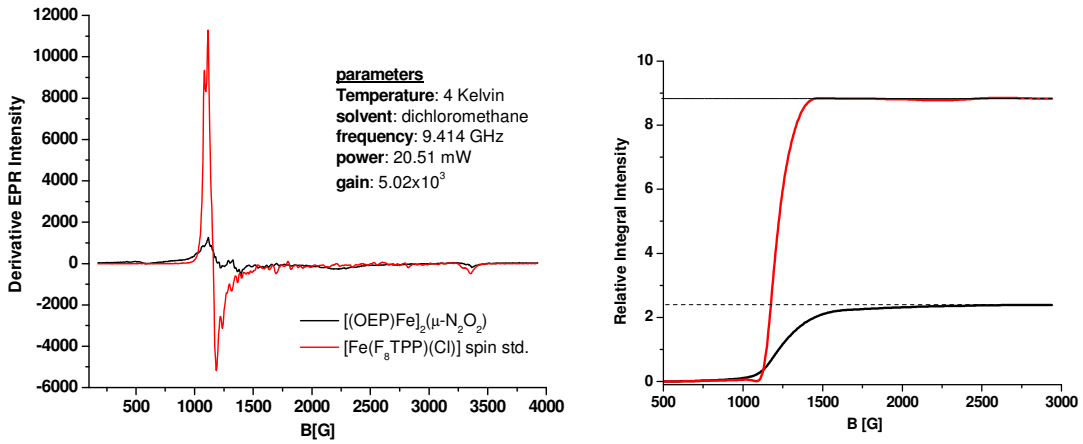

Figure 5.1. EPR spectrum of $[(OEP)Fe]_2(\mu\text{-}N_2O_2)$ versus the S = 5/2 spin standard $[Fe(F_8TPP)(Cl)]$ recorded at 4 K.(left) Spin quantification of the EPR data.(right)

of [Fe(OEP)]Cl and H_2O. Interestingly, EPR spectra recorded at 77 K show g-values of 5.74 and 2.03; consistent with an S = 5/2 high-spin ferric heme. This is surprising as the two iron centers within $[Fe(OEP)]_2(\mu\text{-}N_2O_2)$ would be expected to be magnetically coupled; thus yielding an EPR-silent complex.

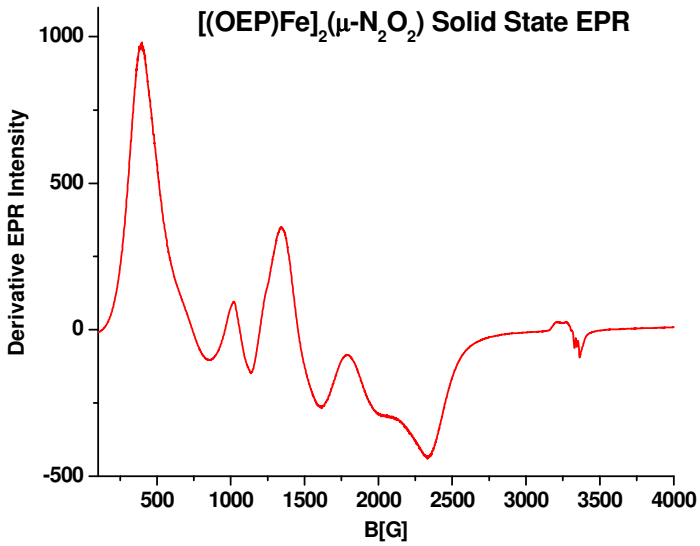

Figure 5.2. Solid state EPR spectrum of $[(OEP)Fe]_2(\mu\text{-}N_2O_2)$ recorded at 4 K.

In an effort to more thoroughly probe the electronic structure and spin state of $[Fe(OEP)]_2(\mu\text{-}N_2O_2)$, liquid He (4 K) EPR spectroscopy has been employed. As previously reported, the EPR spectrum of a frozen CH_2Cl_2 solution of $[Fe(OEP)]_2(\mu\text{-}N_2O_2)$, shown in Figure 5.1, does indeed show signals consistent with an S = 5/2 high-spin complex. However, spin quantification against known S = 5/2 standards shows the response to be only a minor component of the $[Fe(OEP)]_2(\mu\text{-}N_2O_2)$ sample (~20 % impurity). It is therefore more accurate to assign $[Fe(OEP)]_2(\mu\text{-}N_2O_2)$ as EPR-silent; displaying either strongly ferromagnetic (integer spin) or antiferromagnetic (zero spin) coupling across the hyponitrite bridge. The observed impurity is consistent across multiple preparations of $[Fe(OEP)]_2(\mu\text{-}N_2O_2)$ and therefore most likely represents a [Fe(OEP)(X)] side product inherent to the synthesis of this complex. EPR spectra obtained on solid samples of $[Fe(OEP)]_2(\mu\text{-}N_2O_2)$ show highly distorted signals indicative of intermolecular spin coupling in the solid state.[11] This data is shown in Figure 5.2.

As $[Fe(OEP)]_2(\mu\text{-}N_2O_2)$ is EPR-silent, SQUID susceptibility measurements were employed in an effort to determine the molecular spin state. These data are

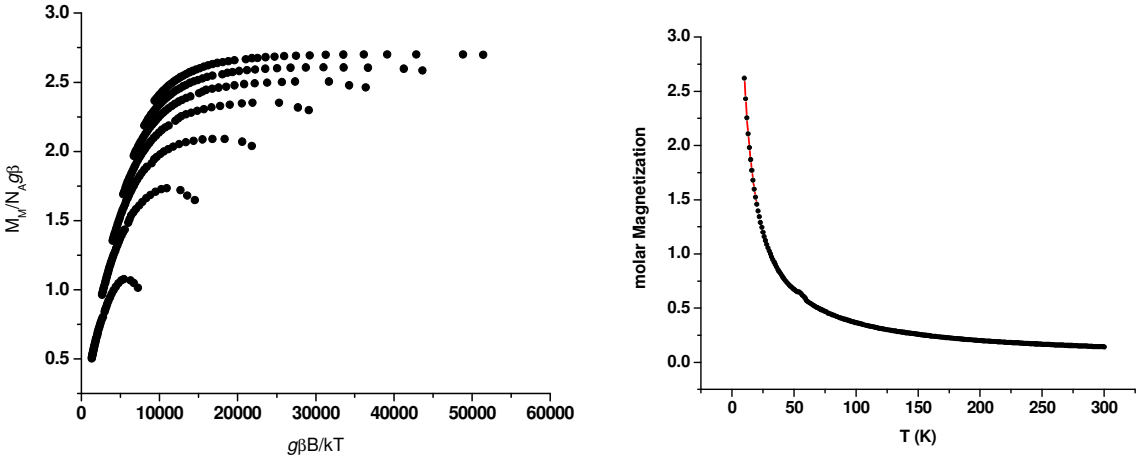

Figure 5.3. SQUID susceptibility data for $[(OEP)Fe]_2(\mu\text{-}N_2O_2)$. (left) Data recorded from 1.8 – 10 K at each field between 1 – 7 T, (right) data collected at 0.5 T.

shown in Figure 5.3 and indicate an effective magnetic moment (μ_{eff}) of 7.7 μ_{BM} at 250 K. Surprisingly, this is consistent with an intermediate S = 3 total spin, likely resulting from ferromagnetic coupling of two S = 3/2 intermediate spin Fe(III) centers. The ferromagnetic coupling is maintained between 1.8 and 250 K, indicating a strong nuclear dipolar coupling (J). Several other ferric OEP complexes have been reported in the literature to be intermediate spin; such as $[Fe(OEP)]ClO_4$, $[Fe(OEP)(3\text{-}ClPy)]ClO_4$ (3-ClPy = 3-chloropyridine), and $[Fe(OEP)(ONNMe_2)]ClO_4$.[12-14] In addition to these, $[Fe(OEP)]_2(\mu\text{-}N_2O_2)$ represents another rare example of a synthetic intermediate-spin ferric heme complex with axial anionic oxygen donors.

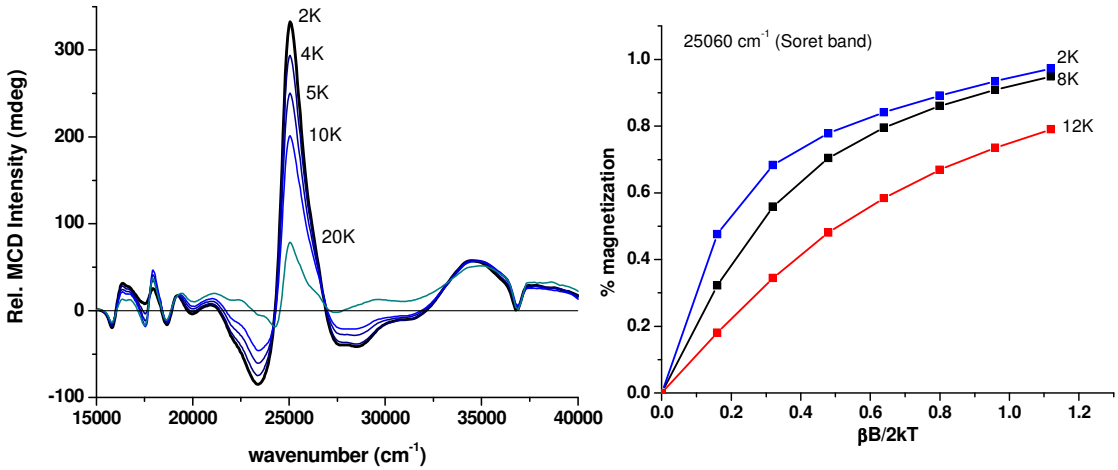

Figure 5.4. MCD spectra of $[(OEP)Fe]_2(\mu\text{-}N_2O_2)$ recorded in polystyrene matrix at 2 K (left). Magnetization plots calculated for the Soret band show a large degrees of anisotropy as evident from the nesting behavior (right).

In support of the observed S = 3 total spin, low-temperature (< 50 K) VTVH MCD spectra on $[Fe(OEP)]_2(\mu\text{-}N_2O_2)$ embedded in a polystyrene matrix show both temperature- and field-dependent saturation. This observation is in accordance with MCD C-term intensity resulting from ferromagnetic coupling between the two iron centers. The alternative antiferromagnetically coupled spin state would be expected to lead to a diamagnetic ground-state, and hence, lack of C-term intensity. Therefore, MCD intensity would not show field saturation. The average MCD spectra of $[Fe(OEP)]_2(\mu\text{-}N_2O_2)$ taken at 2 K between 1 – 7 T are shown in Figure 5.4. Magnetization plots generated from the $[Fe(OEP)]_2(\mu\text{-}N_2O_2)$ MCD data show, as expected, a high degree of nesting. As a result, fitting of the MCD data to determine total spin is non-trivial and was not performed.

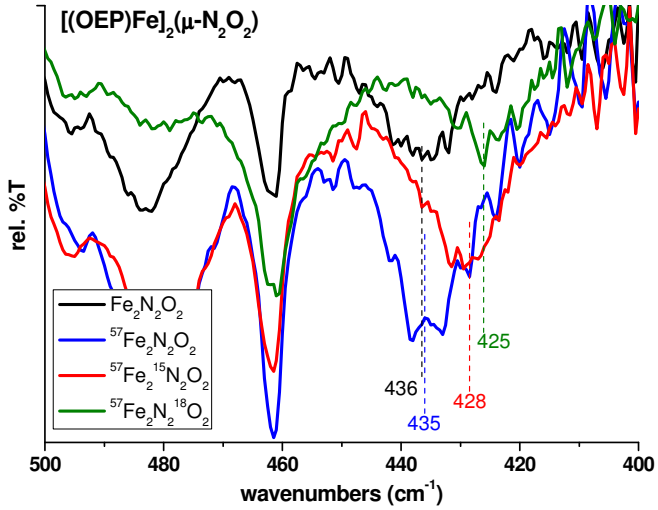

Figure 5.5. IR spectra of $[(OEP)Fe]_2(\mu\text{-}N_2O_2)$ and isotopes thereof. Isotope sensitivity consistent with an Fe-O-N bending mode at 436 cm^{-1}.

Vibrational data was obtained using both FT-IR and NRVS[15-16] spectroscopy to gain more insight into the nature of the hyponitrite bridge and expand on magnetic data presented above. Here, vibrational assignments are key as they provide insight into the bond strengths and energies within the hyponitrite unit. The antisymmetric N-O stretching feature of $[Fe(OEP)]_2(\mu\text{-}N_2O_2)$ has been previously assigned at 982 cm^{-1} based on ^{15}N and ^{18}O labeling of the hyponitrite bridge.[7] In addition, a weak isotope-sensitive band is also present at 436 cm^{-1} in the infrared spectrum. This feature is sensitive to both ^{15}N and ^{18}O labeling and is therefore tentatively assigned as an Fe-O-N bending mode (see Figure 5.5). As the FT-IR features associated with the Fe-O-N-N-O-Fe unit are

relatively weak and difficult to identify, NRVS measurements were employed in an attempt to further elucidate the vibrational structure of $[Fe(OEP)]_2(\mu\text{-}N_2O_2)$. Unfortunately, as shown in Figure 5.6, only a single isotope-sensitive band is visible in the NRVS spectra which is located at 322 cm^{-1} and shifts to 310 cm^{-1} upon $^{15}N^{18}O$ labeling. The lack of features in the NRVS spectra is surprising as NRVS intensity is directly correlated with ^{57}Fe motion within a given vibrational mode. Additionally, the NRVS technique has been quite successful in regards to characterization of small molecule-bound heme complexes. It could therefore be inferred that the Fe-O-N-N-O-Fe unit in $[Fe(OEP)]_2(\mu\text{-}N_2O_2)$ would likely be highly NRVS-active;[17-18] this is, however, not the case.

Table 5.1. Comparison of DFT predicted and experimentally determined geometric and vibrational properties for $[Fe(OEP)]_2(\mu\text{-}N_2O_2)$.

	$[(P)Fe]_2(\mu\text{-}N_2O_2)$ S = 3	$[(P)Fe]_2(\mu\text{-}N_2O_2)$ S = 5	$[Fe(OEP)]_2(\mu\text{-}N_2O_2)$ crytal structure
Geometric properties [Å, °]			
Fe-O	1.94	1.90	1.89
N-O	1.34	1.35	1.38
N-N	1.28	1.27	1.25
Fe---Fe	6.89	6.83	6.69
heme-heme	7.16	7.60	7.26
Fe displacement	0.25	0.47	0.40
Fe-O-N	123.7	124.6	118.6
O-N-N	109.8	109.4	108.5
Vibrational properties [cm^{-1}]			
$\nu(N\text{-}O)_s$	967	963	-
$\nu(N\text{-}O)_{as}$	1025	1011	982
$\nu(N\text{-}N)$	1230	1279	-
$\nu(Fe\text{-}O)_{as}$	509	526	436
$\delta(Fe\text{-}O\text{-}N)_{as}$	338	342	322
$\delta(O\text{-}N\text{-}N)_s$	702	742	-
$(O\text{-}N\text{-}N\text{-}O)_{rocking}$	293	295	-
$(O\text{-}N\text{-}N\text{-}O)_{twist}$	314/317	323	-
E_u (porphyrin)	280	234	272(241)

DFT calculations were employed in order to aid in the assignment of the vibrational features of $[Fe(OEP)]_2(\mu\text{-}N_2O_2)$ and investigate the lack of intense NRVS features for this complex. Geometry optimizations were performed at the BP86/TZVP theory level followed by B3LYP/TZVP single point energy calculations on the porphine approximated model, $[(P)Fe]_2(\mu\text{-}N_2O_2)$. Here, geometric parameters of both the S = 3 and S = 5 DFT models match the experimentally determined parameters well. The Fe-O bond is predicted at 1.94 and 1.90 Å for the S = 3 and S = 5 models, respectively, compared to 1.89 Å in the crystal structure. Furthermore, O-N distances and Fe-O-N angles were predicted at 1.34 and 1.35 Å along with 123.7° and 124.6° for the S = 3 and S = 5 models,

respectively, compared to 1.38 Å and 118.6° in the crystal structure. Additional geometric parameters are detailed in Table 5.1.

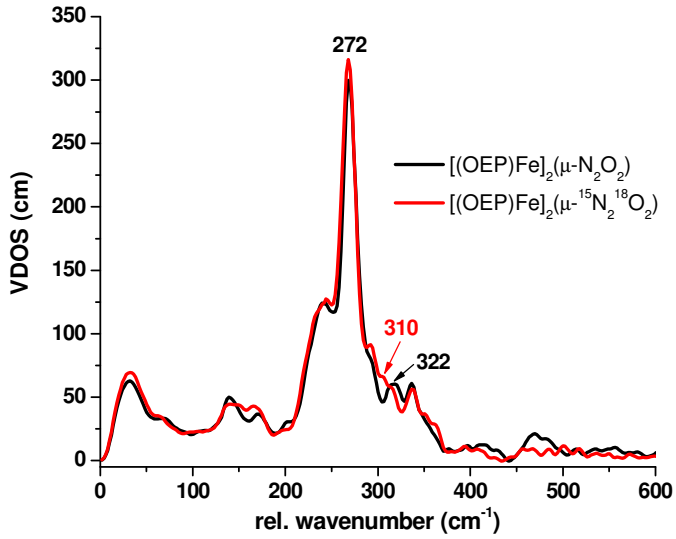

Figure 5.6. NRVS spectra of $[(OEP)Fe]_2(\mu\text{-}N_2O_2)$ and the corresponding $^{15}N_2{}^{18}O_2$ isotope.

Frequency calculations on this model at the BP86/TZVP theory level predict a total of eight vibrational modes with significant Fe-O-N-N-O-Fe character between ~300 – 1300 cm^{-1}. Interestingly, the DFT-predicted vibrational modes show only minimal iron displacement, with most of the atomic motion located on the hyponitrite bridge. This curious result explains the observed lack of NRVS intensity as vibrational features with low iron motion will be extremely weak and difficult to resolve.[15] Currently, only three of the predicted features can be assigned using a combination of FT-IR and NRVS spectroscopy. For the S = 3 model, both the symmetric and antisymmetric N-O stretching features are predicted to be within 50 cm^{-1} of the experimentally observed 982 cm^{-1} feature at 967 and 1025 cm^{-1}, respectively. As this mode is observed in the FT-IR spectrum it is most likely the antisymmetric stretch, as previously stated, due to the symmetry forbidden nature of the corresponding symmetric mode. Additionally, the afore mentioned $^{15}N_2{}^{18}O_2$ isotope-sensitive FT-IR feature at 436 cm^{-1} is assigned as an antisymmetric Fe-O stretching vibration, predicted at 509 cm^{-1} for the S = 3 DFT model. This mode again has the appropriate symmetry to be IR-allowed. The final vibrational feature observed at 322 cm^{-1} with ^{57}Fe-enriched NRVS measurements is predicted to be an antisymmetric Fe-O-N bending mode which DFT estimates at 338 cm^{-1}. Vibrational data was also predicted for the high-spin S = 5 $[(P)Fe]_2(\mu\text{-}N_2O_2)$ model. As shown in Table

5.1, the intermediate-spin S = 3 model is in better agreement with experimentally determined vibrational data; the only exception being the proposed antisymmetric N-O stretch which is in closer agreement with a high-spin model.

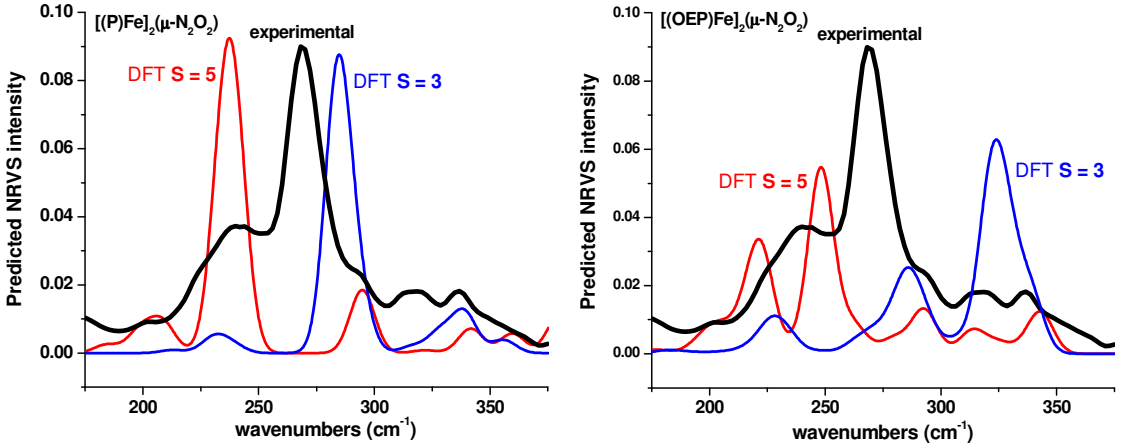

Figure 5.7. DFT predicted versus experimental NRVS data showing the shift in the porphyrin-based E_u-symmetric vibrational mode upon change in spin state. Spectra predicted with the porphine approximation show clean single E_u features while DFT models employing the full OEP ligand predict split E_u-symmetric features.

In addition to vibrational features associated specifically with the Fe-O-N-N-O-Fe moiety, NRVS allows for accurate identification of the porphyrin in-plane Fe-$N_{pyrrole}$ stretching mode of E_u symmetry in heme-containing samples. As shown in Table 5.1, this mode is predicted to be highly sensitive to the total spin in the truncated $[(P)Fe]_2(\mu\text{-}N_2O_2)$ model. Here, the porphine E_u feature is predicted at 234 and 280 cm^{-1} for S = 5 and S = 3 $[(P)Fe]_2(\mu\text{-}N_2O_2)$ models, respectively, as shown in Figure 5.7, top. Here the position of the E_u mode supports the S = 3/2 spin state of the [Fe(OEP)] centers. Inclusion of the complete OEP ligand in the DFT model maintains the observed separation between the S = 5 and S = 3 E_u band, however, due to the loss of symmetry in OEP compared to porphine, the predicted features are split into a major (higher energy) and minor (lower energy) component. The experimentally observed E_u feature is also split in agreement with the DFT results; showing signals at 272(major) and 241(minor) cm^{-1}, respectively, as shown in Figure 5.7. In this case, the experimental NRVS spectrum places the E_u vibrational mode intermediate between the predicted E_u vibrations in the S = 5 and S = 3 models. In the DFT calculated spectra the S = 3 $[Fe(OEP)]_2(\mu\text{-}N_2O_2)$ model predicts the E_u mode at 324 and 286 cm^{-1} while the corresponding S = 5 model

places the feature at 248 and 221 cm^{-1}. A plot of the predicted versus experimental NRVS data is shown in Figure 5.7.

5.2. Reactivity and Decomposition of $[Fe(OEP)]_2(\mu\text{-}N_2O_2)$

The hyponitrite-bridged dimer $[Fe(OEP)]_2(\mu\text{-}N_2O_2)$ displays interesting reactivity in the presence of both HCl and 1-methylimidazole (MI). Addition of HCl promotes NOR-type reactivity and results in the production of N_2O as previously reported.[7] In addition to N_2O formation in the presence of acid, $[Fe(OEP)]_2(\mu\text{-}N_2O_2)$ slowly decomposes in solution at room temperature to yield two equivalents of [Fe(OEP)(NO)] (see Scheme 5.1). This reaction is in essence the reverse of the proposed N-N radical-type coupling of two coordinated NO ligands in the active site of NorBC; where two Fe-NO units couple to yield a hyponitrite bridge:[2, 4]

$$2[Fe(OEP)(NO)] \rightleftharpoons [Fe(OEP)]_2(\mu\text{-}N_2O_2)$$

Obviously, ferrous heme nitrosyls are stable in solution and do not spontaneously dimerize. For this reason, $[Fe(OEP)]_2(\mu\text{-}N_2O_2)$ can only be obtained from preformed $N_2O_2^{2-}$. This relates back to the extraordinary stability of the Fe-NO bond in ferrous heme nitrosyls. Importantly, the synthetic model complex $[Fe(OEP)]_2(\mu\text{-}N_2O_2)$ offers the unique opportunity to study the reactivity and electronic structure of the diiron hyponitrite moiety outside of a reactive protein environment. In particular, elucidation of the mechanism of the dissociation of the complex can shed light on the corresponding reductive N-N coupling of nitrosyl moieties within NorBC.

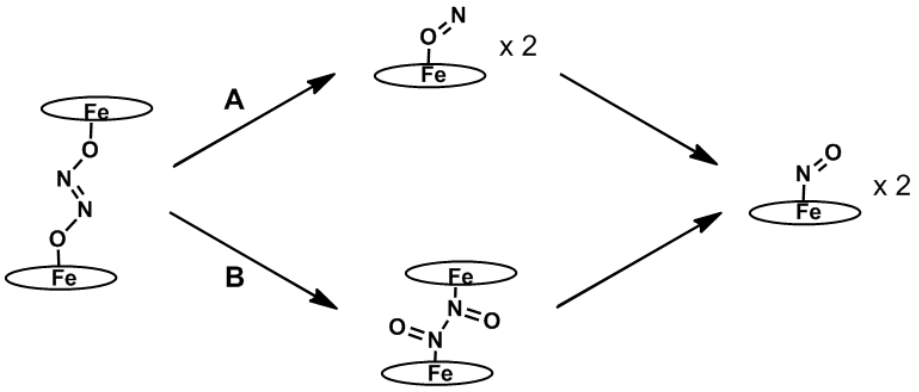

Scheme 5.1. Potential decomposition pathways of $[(OEP)Fe]_2(\mu\text{-}N_2O_2)$ in solution.

In order to experimentally probe the thermal decomposition of $[Fe(OEP)]_2(\mu\text{-}N_2O_2)$, UV-visible absorption and EPR spectroscopy have been employed. EPR

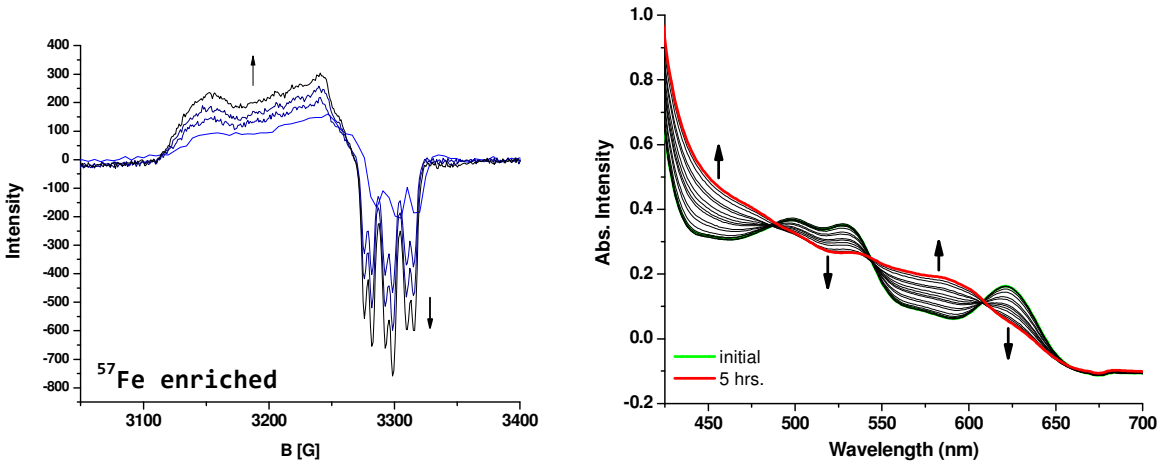

Figure 5.8. EPR spectra of thermally annealed samples of $[(OEP)Fe]_2(\mu\text{-}N_2O_2)$ in toluene (left) and absorption spectra of the corresponding thermal decomposition at 30 °C over the course of 5 hours (right).

spectroscopy shows clear decomposition to [Fe(OEP)(NO)] as a final product. Spectra recorded on thermally annealed samples of $[Fe(OEP)]_2(\mu\text{-}N_2O_2)$ in toluene slowly decompose to reveal an axial S = 1/2 species with clear three-line hyperfine splitting on g_{min} (see Figure 5.8). These data are consistent with formation of a ferrous heme nitrosyl where coupling of the nuclear spin (I = 1) of ^{14}N with the electron spin (S = ½) leads to a characteristic three-line splitting in the EPR spectrum.[19] In addition, absorption measurements, shown in Figure 5.8, performed at 30 °C in CH_2Cl_2 show clean isosbestic conversion of the 620 nm Q-band of $[Fe(OEP)]_2(\mu\text{-}N_2O_2)$ to a new species with broad absorption features between 565 and 595 nm; consistent with formation of [Fe(OEP)(NO)]. The observed rate constant for this transformation has been measured at $6.4x10^{-5}$ s^{-1} under the given conditions. The slow rate constant is in agreement with DFT calculations which predict high-energy intermediates in the decomposition pathway. Both absorption and EPR spectroscopy are thus in agreement and clearly show formation of the five-coordinate ferrous heme nitrosyl [Fe(OEP)(NO)].

In the presence of 1-methylimidazole (MI), as a model for histidine in proteins, a 1 mM toluene solution of $[Fe(OEP)]_2(\mu\text{-}N_2O_2)$ decomposes to yield [Fe(OEP)(NO)] at noticeably faster rates than in the absence of an axial base. As monitored by 77 K EPR spectroscopy, full conversion to the nitrosyl product is achieved after only 80 minutes in the presence of a 13-fold molar excess of MI; compared to an estimated 6 hours for $[Fe(OEP)]_2(\mu\text{-}N_2O_2)$ alone (see Figure 5.9). This result was also confirmed by absorption spectroscopy at 30 °C in

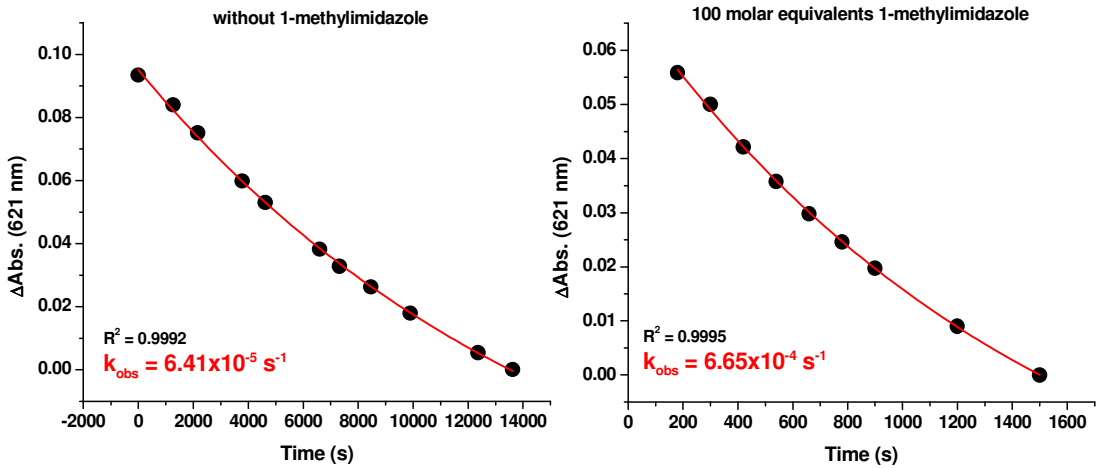

Figure 5.9. Kinetic plots of the thermal decomposition of $[(OEP)Fe_2](\mu\text{-}N_2O_2)$ in the absence (left) and presence (right) of 1-methylimidazole.

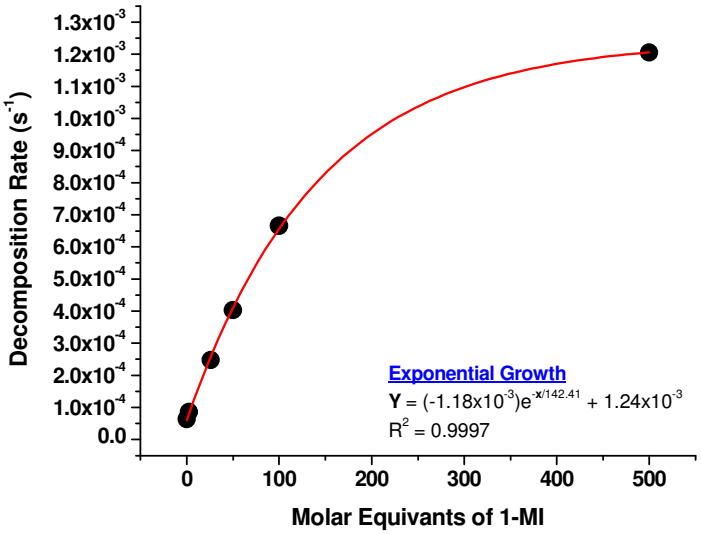

Figure 5.10. Dependence of the decomposition rate of $[(OEP)Fe]_2(\mu\text{-}N_2O_2)$ on molar equivalents of MI.

the presence of varied MI equivalents. Figure 5.10 shows the rate dependence of [Fe(OEP)(NO)] formation on the MI concentration, giving a maximal rate of $1.24x10^{-3}$ s^{-1} when MI is in >500 molar excess. Importantly, saturation behavior is observed as higher concentrations of MI are added; implying equilibrium effects upon MI addition. Based on these findings it is likely that decomposition occurs most rapidly via a bis-imidazole complex where MI binds axially across the N_2O_2-bridged complex (see Scheme 5.2). Here, equilibrium binding of MI prohibits complete formation of the unstable bis-imidazole adduct, only reaching complete formation at >500 molar excess of MI. At relatively high equivalents of MI (>100 eq.), NO is also displaced from the

product complex [Fe(OEP)(NO)]. Here, the large excess of MI readily displaces NO, yielding the corresponding six-coordinate bis-imidazole complex $[Fe(OEP)(MI)_2]$. This reaction is observed in EPR experiments where the [Fe(OEP)(NO)] product can be seen to disappear in the presence > 100 equivalents of MI.

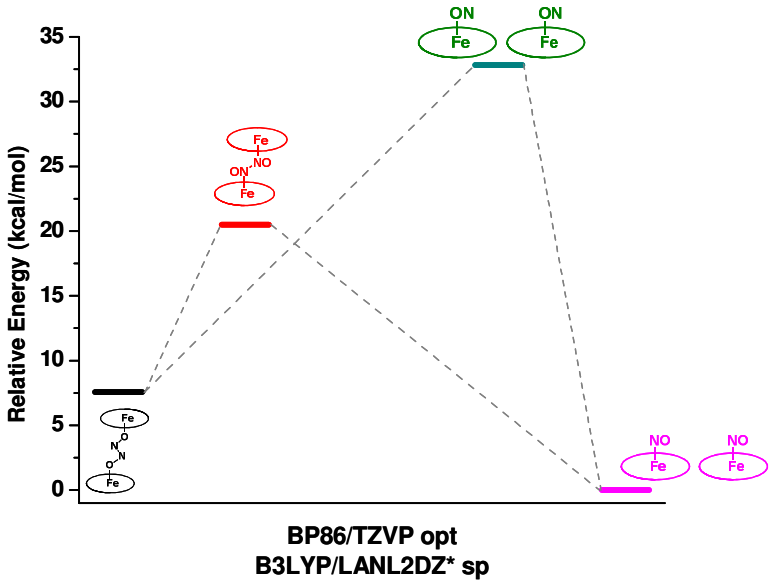

Figure 5.11. Relative energies of potential reaction intermediates calculated from BP86/TZVP optimized structures using B3LYP/LANL2DZ* single point energies.

Given that the hyponitrite bridge is O-bound in $[Fe(OEP)]_2(\mu\text{-}N_2O_2)$, there are several potential pathways leading to the observed nitrosyl product. The most likely of which are labeled as A and B in Scheme 5.1 and involve either preliminary breaking of the N-N bond of hyponitrite, leading to two O-bound [Fe(OEP)(ON)] complexes which rapidly isomerize to the energetically favored N-bound isomer; or isomerization of $[Fe(OEP)]_2(\mu\text{-}N_2O_2)$ leading to an N-bound hyponitrite bridge which is followed by N-N bond cleavage to yield the observed [Fe(OEP)(NO)] product. In order to further elucidate the mechanism of N-N bond cleavage resulting in formation of [Fe(OEP)(NO)], DFT calculations were employed. Full optimization of $[Fe(OEP)]_2(\mu\text{-}N_2O_2)$ was performed at the BP86/TZVP theory level for both the S = 3 and S =5 spin states. The experimentally observed S = 3 intermediate-spin state is predicted to be 18.5 kcal/mol below the S = 5 high-spin state. Analogous calculations applied to the porphine-approximated complex $[(P)Fe]_2(\mu\text{-}N_2O_2)$ after employing B3LYP/TZVP single point energies on the BP86/TZVP optimized structures raises the energy of the S = 3 ground state relative to the S = 5 state. Using this model, the S = 5 spin state is now favored by 5.3 kcal/mol. Comparatively, the two S = 1/2

[Fe(P)(NO)] product compounds are located 6.0 kcal/mol below the S = 3 hyponitrite-bridged starting material. In light of the experimentally observed S = 3 spin, DFT analysis was performed on intermediate-spin porphine-approximated models in order to assess the mechanism of [Fe(OEP)(NO)] formation and to determine why the reverse reaction is not observed. Interestingly, both likely decomposition pathways (see Scheme 5.1) proceed through either an N-bound hyponitrite-bridged isomer or a transient pair of O-bound heme nitrosyls, respectively. Both of these intermediate states are predicted to be energetically unfavorable and exist between 12 and 25 kcal/mol above the S = 3 $[(P)Fe]_2(\mu\text{-}N_2O_2)$ starting material (see Figure 5.11). It can thus be concluded that although there is a large thermodynamic driving force for [Fe(OEP)(NO)] formation, this reaction is kinetically hindered by high-energy intermediates.

Of the proposed decomposition mechanisms given in Scheme 5.1, pathway A, which involves initial N-N bond breaking followed by isomerization of the nitrosyl unit, does not require compression of the heme-heme distance. The

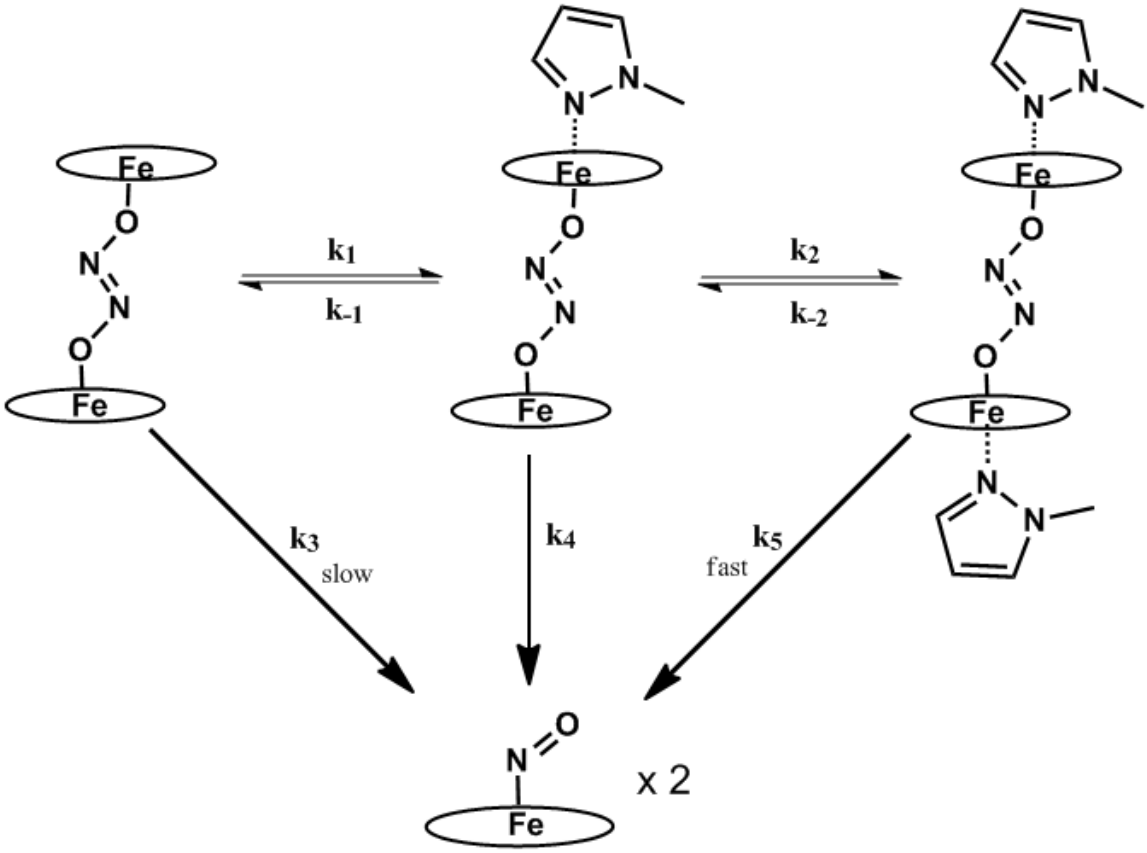

Scheme 5.2. Schematic depiction of equilibrium binding of 1-MI. Decomposition via k_3 is observed to be slow in comparison to decomposition via k_5.

required shortening of the Fe-Fe distance for the formation of an N-bound hyponitrite in pathway B is substantial. DFT calculations predict a heme-heme distance of 7.16 Å for the crystallographically observed O-bound hyponitrite isomer and 5.71 Å for the corresponding N-bound isomer. Importantly, the crystal structure of $[Fe(OEP)]_2(\mu\text{-}N_2O_2)$ shows two disordered CH_2Cl_2 solvent molecules packed around the N_2O_2 core between the heme planes.[7] Therefore, there exists an additional energetic barrier to compression of the heme-heme distance as these solvent molecules must be expelled from the core. This matter is further compounded by steric interactions of the ethyl substitutents on OEP^{2-}. The porphine approximation used in the DFT calculations neglects these interactions, which represent an additional energetic barrier to formation of an N-bound $[Fe(OEP)]_2(\mu\text{-}N_2O_2)$ isomer. For these reasons, we propose pathway B to be more similar in energy to that of pathway A, representing a barrier of ~20 – 25 kcal/mol.

Both DFT and experimental results indicate a slow dissociation of $[Fe(OEP)]_2(\mu\text{-}N_2O_2)$ into [Fe(OEP)(NO)]. The DFT predicted barrier of 20 – 25 kcal/mol fits well with the observed decomposition rate of $6.41\text{x}10^{-5}$ s^{-1}, which correlates with an activation energy of ~23 kcal/mol. Importantly, because [Fe(OEP)(NO)] is ~7 kcal/mol lower in energy than $[Fe(OEP)]_2(\mu\text{-}N_2O_2)$, the dimerization of [Fe(OEP)(NO)] must overcome a barrier of ~32 kcal/mol. This large barrier results in a predicted rate of approximately $1\text{x}10^{-11}$ s^{-1} which is far too slow to ever generate an observable amount of $[Fe(OEP)]_2(\mu\text{-}N_2O_2)$. For this reason, the dissociation of $[Fe(OEP)]_2(\mu\text{-}N_2O_2)$ is slow and the dimerization of [Fe(OEP)(NO)] is kinetically forbidden.

In summary, the model complex $[Fe(OEP)]_2(\mu\text{-}N_2O_2)$ exhibits an intermediate S = 3 total spin, due to ferromagnetic coupling of two S = 3/2 iron centers across a hyponitrite bridge. Interestingly, $[Fe(OEP)]_2(\mu\text{-}N_2O_2)$ is able to dissociate across the central N-N bond, leading to the formation of [Fe(OEP)(NO)]. The dissociation rate is relatively slow in the absence of an axial base, indicative of a substantial kinetic barrier for this reaction. However, upon addition of MI, the dissociation rate constant increases until saturation at a rate of $1.24\text{x}10^{-3}$ s^{-1}. These results provide further evidence that a radical-type coupling within NorBC is unlikely. However, in the event that a radical coupling mechanism in fact possible, these results indicate that the presence of an axial N-donor, such as the proximal histidine (HIS) residue in NorBC, favors formation of a heme nitrosyl rather than a hyponitrite species. It is

therefore likely that during NorBC turnover the axial HIS ligand is displaced, leading to a five-coordinate hyponitrite intermediate. In this way, the back reaction to reform a ferrous heme nitrosyl is suppressed. Upon formation of a $N_2O_2^{2-}$ bridge in the NorBC active site, displacement of the heme iron towards the proximal pocket may be responsible for dissociation of the proximal HIS ligand. A similar scenario has been proposed based on enzymatic studies where spectroscopic characterization of NorBC from *Paracoccus denitrificans* indicates lability of the heme b_3 Fe-HIS bond.[4]

Experimental

Preparation and handling of air sensitive materials was carried out under an argon atmosphere in an MBraun glovebox equipped with a circulating purifier (O2, H2O < 0.1 ppm). Infrared spectra were obtained from KBr disks on a Perkin-Elmer BX spectrometer. Electronic absorption spectra were measured using an Analytical Jena Specord 600 instrument. Electron paramagnetic resonance spectra were recorded on a Bruker X-band EMX spectrometer equipped with an Oxford Instruments liquid nitrogen cryostat. EPR spectra were typically obtained on frozen solutions using ~20 mW microwave power and 100 kHz field modulation with the amplitude set to 1 G. SQUID susceptibility measurements were conducted on a Quantum Design MPMS-XL7 equipped with an Evercool Dewar. Samples were prepared as mixtures with either eicosane or silicon oil in a polycarbonate capsule.

The complex $[Fe(OEP)]_2(\mu\text{-}N_2O_2)$ was prepared by the Richter-Addo laboratory as previously reported and stored under inert gas at -34 °C until ready to use. All solvents were purified by distillation under and Ar atmosphere followed by three freeze-pump-thaw cycles prior to use. 1-methylimidazole was obtained from Sigma-Aldrich and was also purified by distillation under and Ar atmosphere followed by three freeze-pump-thaw cycles prior to use.

References

(1) Blomberg, M. R. A.; Sieghahn, P. E. M., *Biochemistry* **2012,** *51*, 5173.
(2) Girsch, P.; de Vries, S., *Biochim. Biophys. Acta* **1997,** *1318*, 202.
(3) Lehnert, N.; Berto, T. C.; Galinato, M. G. I.; Goodrich, L. E., In *The Handbook of Porphyrin Science*, Kadish, K. M.; Smith, K. M.; Guilard, R., Eds. World Scientific: Singapore, 2011; Vol. 14, pp 1-247.
(4) Moenne-Loccoz, P., *Nat. Prod. Rep.* **2007,** *24*, 610.
(5) Arikawa, Y.; Onishi, M., *Coord. Chem. Rev.* **2012,** *256*, 468.
(6) Blomberg, L. M.; Blomberg, M. R. A.; Sieghahn, P. E. M., *Biochim. Biophys. Acta* **2006,** *1757*, 240.
(7) Xu, N.; Campbell, A. L. O.; Powell, D. R.; Khandogin, J.; Richter-Addo, G. B., *J. Am. Chem. Soc.* **2009,** *131*, 2460.
(8) Franz, K. J.; Lippard, S. J., *J. Am. Chem. Soc.* **1999,** *121*, 10504.
(9) Schneider, J. L.; Carrier, S. M.; Ruggiero, C. E.; Young, V. G., Jr.; Tolman, W. B., *J. Am. Chem. Soc.* **1998,** *120*, 11408.
(10) Arulsamy, N.; Bohle, D. S.; Imonigie, J. A.; Moore, R. C., *Polyhedron* **2007,** *26*, 4737.
(11) Safo, M. K.; Gupta, G. P.; Walker, F. A.; Scheidt, W. R., *J. Am. Chem. Soc.* **1991,** *113*, 5497.
(12) Axe, F. U.; Flowers, C.; Loew, G. H.; Waleh, A., *J. Am. Chem. Soc.* **1989,** *111*, 7333.
(13) Dolphin, D. H.; Sams, J. R.; Tsin, T. B., *Inorg. Chem.* **1977,** *16*, 711.
(14) Scheidt, W. R.; Geiger, D. K.; Hayes, R. G.; Lang, G., *J. Am. Chem. Soc.* **1983,** *105*, 2625.
(15) Scheidt, W. R.; Durbin, S. M.; Sage, J. T., *J. Inorg. Biochem.* **2005,** *99*, 60.
(16) Lehnert, N., Quantum Chemistry Centered Normal Coordinate Analysis (QCC-NCA): Routine Application of Normal Coordinate Analysis for the Simulation of the Vibrational Spectra of Large Molecules. In *Computational Inorganic and Bioinorganic Chemistry*, Solomon, E. I.; King, R. B.; Scott, R. A., Eds. John Wiley & Sons: Chirchester, UK, 2009; pp 123-140.
(17) Rai, B. K.; Durbin, S. M.; Prohofsky, E. W.; Sage, J. T.; Wyllie, G. R. A.; Scheidt, W. R.; Sturhahn, W.; Alp, E. E., *Biophys. J.* **2002,** *82*, 2951.
(18) Lehnert, N.; Galinato, M. G. I.; Paulat, F.; Richter-Addo, G. B.; Sturhahn, W.; Xu, N.; Zhao, J., *Inorg. Chem.* **2010,** *49*, 4133.
(19) Lehnert, N., Electron Paramagnetic Resonance and Low-Temperature Magnetic Circular Dichroism Spectroscopy of Ferrous Heme Nitrosyls. In *The Smallest Biomolecules: Diatomics and their Interactions with Heme Proteins*, Ghosh, A., Ed. Elseviere: Amsterdam, 2008; pp 147-171.

Chapter 6

Endothelial NO Export by Hb/Mb-NO_2^-

The role of NO and nitrite-bound methemoglobin (Hb(III)-NO_2^-) in hypoxic signaling is highly controversial. One provoking possibility is that hemoglobin (Hb) functions as a nitrite anhydrase, producing N_2O_3 (from nitrite) as an NO carrier. The ability of Hb to generate N_2O_3 would provide an intriguing means of NO release from red blood cells. To investigate this process, models of the hemoglobin/myoglobin active site have been constructed. Our results show that the O-bound (nitrito) form of Hb/Mb(III)-NO_2^- is essential for the formation of N_2O_3. This may explain why Hb/Mb adopt the nitrito binding geometry over the more common N-bound (nitro) form. The formation and release of N_2O_3 is shown to be energetically favorable by 1 - 3 kcal/mol by the DFT calculations, opening up the anhydratase function of Hb/Mb as a biologically feasible process.

6.1. DFT Assessment of N_2O_3 Formation by Hb/Mb-NO_2^- and NO

The role of nitrite in mammalian hypoxic vasodilation is currently a highly contested topic within the field of biological chemistry.[1] In particular, hypoxia sensing is not well understood, although several theories have been proposed. One intriguing possibility, as investigated experimentally by Basu et al, is that an intermediate methemoglobin-nitrite species (Hb(III)-NO_2^-) is able to activate nitrite to produce the meta-stable species N_2O_3 in the presence of free NO.[2a] Such a scenario would provide a convenient means of NO escape (via N_2O_3) from Hb-rich red blood cells (RBCs) under hypoxic conditions. As N_2O_3 possesses a half-life of ~1 ms and a diffusion coefficient of 1000 $\mu m^2\ s^{-1}$, it is not unreasonable to expect that some fraction of N_2O_3 can diffuse out of the erythrocyte.[2] Once released from the RBCs, the NO (obtained via decomposition of N_2O_3 in blood) would then induce vasodilation, and in this way, would direct blood flow to hypoxic tissue.[1] The proposed physiological reactions are shown below in Equations 1-4. Deoxyhemoglobin, Hb(II) in Equation 1, is obtained by release of O_2 from oxy-Hb in dioxygen-poor tissue.

$$Hb(II) + NO_2^- + H^+ \rightarrow Hb(III) + NO + OH^- \quad (1)$$

$$Hb(III) + NO_2^- \rightarrow Hb(III)\text{-}NO_2^- \quad (2)$$

$$Hb(III)\text{-}NO_2^- + NO \rightarrow Hb(III)\text{-}N_2O_3(-) \quad (3)$$

$$Hb(III)\text{-}N_2O_3(-) \rightarrow Hb(II) + N_2O_3 \quad (4)$$

It is known that hemoglobin and myoglobin (Mb) can act as nitrite reductases,[3] Equation 1. However, the feasibility of the nitrite anhydratase reaction, Equation 3, is unknown. Another important question with regard to this reaction is the binding mode of nitrite. It has been shown through a variety of methods (DFT, protein crystallography, model compounds) that nitrite can bind to ferric hemes in either an N-bound (nitro) or O-bound (nitrito) conformation.[4] Most commonly, nitrite shows preference for the nitro binding mode. Interestingly, however, recent crystallographic results indicate that the unusual nitrito form is found in both Hb and Mb, and is therefore biologically relevant.[5] The exact nature of the Fe(III)-nitrite bond can be expected to have direct implications for the reactivity of the bound molecule. This work seeks to clarify the geometric structure of the heme-nitrite complex within ferric Hb/Mb, and to elucidate the feasibility of Equations 3 and 4 as a function of the nitrite binding mode, using DFT calculations.

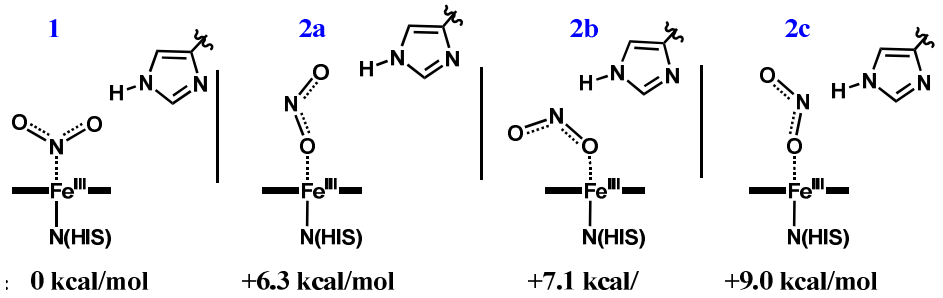

Scheme 6.1. Potential $Mb(III)\text{-}NO_2^-$ structures and their relative energies (BP86/TZVP). All species show S = 1/2 ground states.

To model the interaction of NO with nitrite-bound met-Hb/Mb, a structural model for the Hb/Mb active site was generated based on a high resolution crystal structure of oxy-Mb (PDB code: 1A6M).[6] The model consists of heme b, stripped of its peripheral substituents, one axial (proximal) histidine ligand, and, fixed at the crystallographically determined distance from the iron center, the distal histidine residue, which is involved in hydrogen-bonding interactions with heme-bound molecules. The distal histidine is only fixed at the terminal α-carbon atom, such that its orientation relative to bound substrates is free to optimize. The model system obtained this way

serves as a general model for both the Hb and Mb active sites (therefore referred to as Hb/Mb).

Table 6.1. Comparison of relevant bond lengths and angles between DFT models and protein crystal structures (PDB: 3LR7 and 3D7O).

	Fe-$O_{nitrite}$ [Å]	Fe-N_{His} [Å]	$O_{nitrite}$–N_{His} [Å]	ON-NO_2 [Å]	∠ONO [°]	ref.
Mb(III)-NO_2^-	2.0	2.1	$3.2_{terminal}$ $2.7_{internal}$	-	114	19
αHb(III)-NO_2^-	2.0	2.0	$3.3_{terminal}$ $2.9_{internal}$	-	110	20
2a	1.900	2.024	$3.078_{terminal}$	-	111	-
2a-N_2O_3	1.959	1.976	$3.005_{terminal}$	2.052	119	-

In order to assess the preferred binding mode of nitrite, it was positioned within the distal pocket of our model system in several different orientations with respect to both coordination mode to heme and interaction with the distal histidine residue. These orientations include a nitro (N-bound) and three distinct nitrito (O-bound) coordination modes which are shown in Scheme 1. All orientations were optimized at the BP86/TZVP theory level employing only the constraints indicated above. These structures are inspired by crystallographically observed binding modes of nitrite found in the literature,[4,5] and also recent DFT calculations that explored nitrite binding geometries using a more restricted Mb active site model.[2a] Experimentally, structures **1** and **2a,b** have been observed, where **2b** is seen only in Mb mutants.[5a] The final structure, **2c**, is obtained from **2a** by rotation of nitrite, but this binding geometry has not been observed experimentally. Finally, a distorted Fe-ONO unit similar to **2b** is observed in the β-subunit of Hb, but this tilted structure is not predicted by our DFT results. Overall, the N-bound nitro configuration (**1**) is predicted to be the lowest energy conformation, which is not in agreement with the crystallographically observed structures of ferric Hb/Mb-nitrite adducts. This indicates that besides the hydrogen bond from the distal histidines, other interactions within the active sites of these proteins must contribute to the preference for O-bound nitrite in these cases. The lowest energy nitrito structure (**2a**), in which the remaining O atom of nitrite forms a hydrogen bond with the distal His, is located only 6.3 kcal/mol higher in energy than **1**. The two other nitrito structures **2b** and **2c** are only slightly higher in energy than **2a**. Our calculations follow the experimentally observed results and predict **1** and **2a** to be energetically most favorable. In particular, **2a** corresponds closely to

the experimentally observed structures of met-Mb/Hb nitrite adducts. Our computational models favor H-bonding between the terminal (not bound to Fe) O-atom of NO_2^- and the distal histidine residue, whereas experimentally, H-bonding to the internal O-atom of nitrite is also observed. This finding is attributed to secondary protein effects not accounted for in our model.

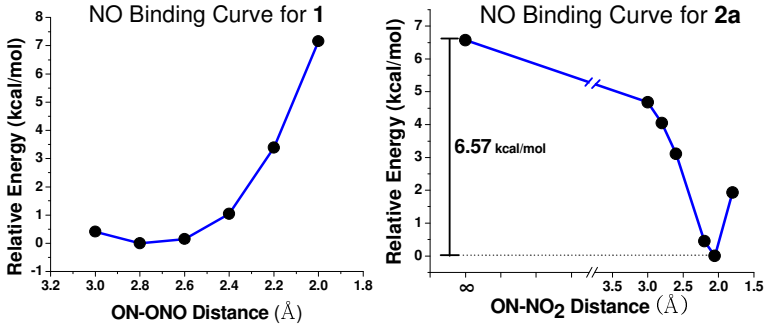

Figure 6.1. Binding curves for NO interacting at either the N atom (**2a**) or O atom (**1**) of ferric Hb/Mb-bound nitrite. The PES is associative (favorable) for formation of N_2O_3 only in the case of **2a**. B3LYP/LanL2DZ and BP86/TZVP calculations were used to construct these energy surfaces.

The interaction of NO with the two lowest energy nitrite-bound structures, **1** and **2a**, was then analyzed in order to assess the potential of each binding mode for N_2O_3 generation. To accomplish this, NO was introduced at a series of fixed distances from the nitrite ligand and each point was allowed to optimize. In this way, potential energy surfaces were generated for NO binding to Hb/Mb(III)-NO_2^- in both **1** and **2a**. Importantly, in the case of the N-bound nitrite complex **1**, the N-atom of nitrite is involved in strong binding to the iron(III) center, and hence, cannot interact with NO. Any attempts to form an N-N bond between the incoming NO and the iron-bound nitrogen atom led to the movement of NO towards nitrite's uncoordinated O atoms. This, however, does not allow for NO coupling to the coordinated NO_2^- ligand either: as seen in Figure 6.1, left, NO addition to **1** leads to a very shallow energy minimum around 2.8 Å, corresponding to the formation of a very weakly associated [ONO-NO]$^-$ adduct. Below ONO-NO distances of 2.8 Å, the nitrite-NO interaction is strongly dissociative. These results demonstrate that *in the normally encountered nitro complex of ferric heme, nitrite is not reactive towards NO, and hence, Equation 3 is not feasible in this case*.

In the case of **2a**, which is the experimentally observed binding mode in met-Hb, the NO_2^- ligand is coordinated to ferric heme such that one O atom binds to the Fe(III) center, while the other O atom forms a hydrogen bond with the distal histidine (O-H distance: 2 Å; cf. Scheme 6.1). Importantly, the N

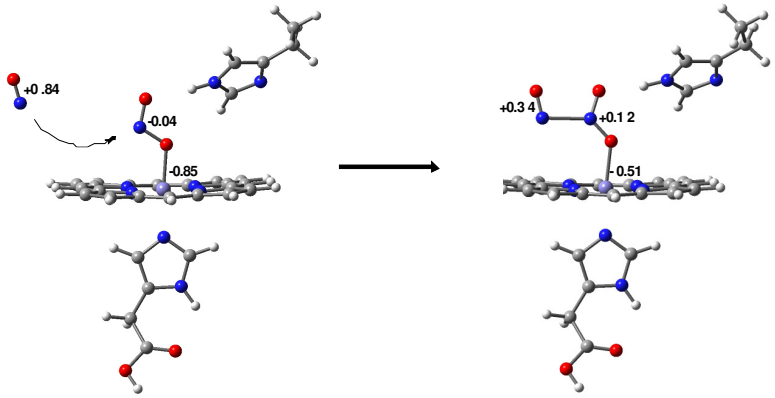

Figure 6.2. Intermediate N_2O_3-bound structure resulting from the reaction of the nitrito complex **2a** with NO. Calculated spin density values for the NO-adduct of **2a** (see on the right) indicate a delocalized radical throughout the Fe(III)-N_2O_3(-) unit. Spin density values are indicated in black. Calculated with BP86/TZVP.

atom of nitrite is now accessible to react with free NO, and, indeed, is able to form the necessary N-N bond to generate N_2O_3. Figure 6.1, right shows the calculated potential energy surface for NO binding to Hb/Mb(III)-NO_2^-. The calculated Fe(III)-N_2O_3(-) structure at the energy minimum predicts a long ON-NO_2^- distance of 2.05 Å and is stabilized by ~7 kcal/mol relative to the NO-free precursor. The observed energy difference provides a significant driving force for NO addition to **2a**. No energy barrier (intermediate) is observed for the formation of the N_2O_3(-) ligand. Further thermodynamic driving force will originate from the entropy gain upon formation of the N-N bond, which can in general be estimated to about -10 kcal/mol at room temperature for small molecule binding to transition metal complexes.[7] Based on this estimate, *the free energy for NO addition to the nitrito complex **2a** is favorable by -15 to -20 kcal/mol at room temperature, and no energy barrier is observed for this process*.

Spin density analysis of **2a** prior to NO association shows values of +0.84 on NO and -0.86 on Fe(III) (see Figure 6.2, left). These values are consistent with the radical nature of NO and the low-spin Fe(III) electronic structure of the Hb/Mb(III)-NO_2^- complex. As NO approaches the bound nitrite, the spin density decreases in magnitude to +0.34 and -0.51 on NO and iron, respectively. This observation is in agreement with the eventual reduction of iron from the ferric to the ferrous state upon dissociation of N_2O_3. The formally Hb/Mb(III)-N_2O_3(-) complex therefore represents an intermediate state at which N_2O_3 is bound to the low-spin iron center and the unpaired electron of NO is delocalized throughout the Fe-O_2N-NO π system. The calculated structure of this N_2O_3-bound intermediate is shown in Figure 6.2, right. The calculated

spin density plot of the Mb(III)-N_2O_3(-) intermediate is shown in Figure 6.3, which further illustrates this observation.

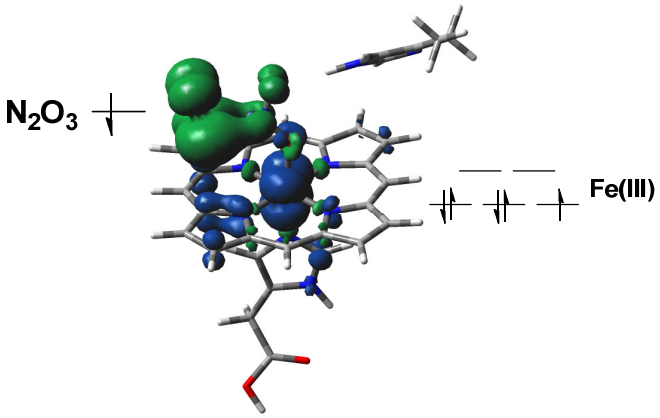

Figure 6.3. Calculated (BP86/TZVP) spin density plot of the Hb/Mb(III)-N_2O_3(-) intermediate. The results show low-spin Fe(III) bound to N_2O_3(-) with a delocalized radical in the π-system (green contour).

Based on our calculations, NO attack on the bound nitrite of Hb/Mb(III)-NO_2^- is not likely to occur through a radical-radical coupling mechanism between NO_2• (as a resonance structure of the ferric nitrite complex) and the incoming NO•, as has been previously proposed.[2a] Calculated spin densities on the NO_2^- moiety consistently show values of < 0.05 during NO approach (see Figure 6.4). These data are consistent with a Fe(III)-NO_2^- electronic structure. Additionally, the redox potential of the NO_2^-/NO_2• pair is relatively high at approximately +1 V.[8] In comparison, the heme sites within Mb and Hb typically show redox potentials in the range of +50 - +200 mV and therefore, are not likely capable of forming a Hb/Mb(II)-NO_2• species.[9] In other words, the contribution of the Hb/Mb(II)-NO_2• resonance structure to the ground state of ferric heme-nitrite complexes is expected to be negligible.

Upon formation of the Hb/Mb(III)-N_2O_3(-) intermediate, N_2O_3 must be able to dissociate from the heme site in order to export NO out of the red blood cell. To model the dissociation process, N_2O_3 was step-wise dissociated from the low-spin iron center of our Hb/Mb model to yield low-spin five-coordinate Hb/Mb(II) and free N_2O_3. The dissociation of N_2O_3 from the iron center is quite endothermic in the low-spin state with a dissociation energy of ~16 kcal/mol. Importantly, however, since five-coordinate ferrous Hb/Mb sites are high-spin, the spin crossover of the iron center upon dissociation of N_2O_3 also needs to be considered. Taking into account the high-spin five-coordinate Hb/Mb(II) product state, N_2O_3 dissociation becomes less endothermic: the final high-spin

product is 4 - 6.5 kcal/mol higher in energy than the initial N_2O_3(-)-bound ferric heme complex (B3LYP/TZVP, depending on the heme structure).[10,11] The predicted high-spin Hb/Mb(II) product state therefore makes the N_2O_3 dissociation process energetically feasible. The spin crossover of the iron center is expected very early on the PES due to the fact that N_2O_3(-) is only a weak ligand to a ferric heme. Hence, due to this early spin crossover, the energy barrier for N_2O_3 dissociation should be very small.

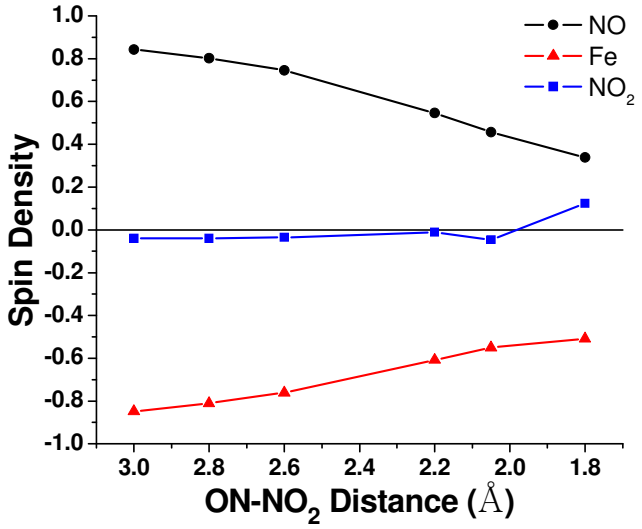

Figure 6.4. Spin density plots for NO, NO_2^-, and Fe within **2a**. As NO approaches the Fe(III)-ONO^- moiety, spin density becomes delocalized across the whole Fe-ONO-NO(-) π system. Calculated with BP86/TZVP.

In summary, our calculations show that both the addition of NO to Hb/Mb(III)-NO_2^- and the dissociation of N_2O_3 from the resulting Hb/Mb(III)-N_2O_3(-) species are energetically feasible, resulting in a total energy for the complete process of -1 to -3 kcal/mol. The net entropy contribution is likely to be negligible as NO association followed by N_2O_3 dissociation can be expected to be close to entropically neutral. The free energy for N_2O_3 production by met-Hb can therefore conservatively be estimated to be slightly exothermic, which indicates that the reaction is biologically feasible. One important restriction for this process is that this reaction is only possible in the ferric nitrito (O-bound) binding mode of nitrite; otherwise, this reaction is energetically very unfavorable. Through generation of the metastable species N_2O_3, it would be possible for NO to escape inactivation (trapping) within red blood cells as previously proposed.[3b] The calculations presented in this paper provide corroborative evidence that the nitrite anhydratase reaction of met-Hb is indeed energetically feasible, which

provides support for the idea of nitrite-dependent signaling in the cardiovascular system, as previously proposed by Basu et al.[2a] While this manuscript was under revision, Hopmann et al. published DFT results that also show the feasibility of the nitrite anhydrase reaction.[12] Importantly, the incorporation of the distal histidine residue in our Hb/Mb active site model (in contrast to ref.12) significantly lowers the predicted free energy of this process and further supports the possibility of N_2O_3-mediated hypoxic signaling.

Experimental

All structures were optimized using the BP86 functional[13] and TZVP basis set[14] unless otherwise stated. The applied model system for the calculations is described in the text. The distal histidine is fixed at the terminal α-carbon at a biologically accurate distance for Hb/Mb of 8.8 Å from the Fe center (see Figure 6.5). Structures **1**, **2a**, **2b**, and **2c** were optimized with only the Fe center and the terminal carbon (C-54, the anchor atom) of the distal histidine fixed in space (to maintain an accurately sized distal pocket). When assessing

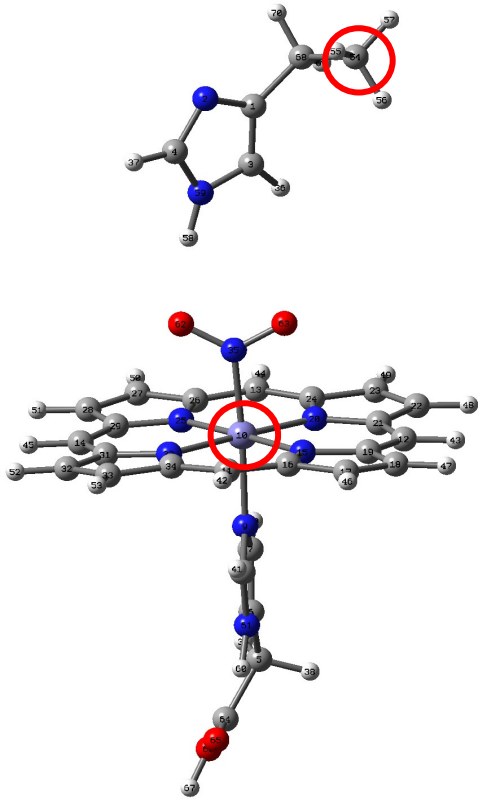

Figure 6.5. Structure of the Hb/Mb(III)-NO_2^- model used in our calculations, indicating the Fe center and the terminal C atom (the 'anchor' atom) of the distal histidine, which were fixed in space for the geometry optimizations. Structure **1** is shown as an example.

the interaction of NO with our Hb/Mb(III)-NO_2^- model, the porphine ring was fixed in space instead of the Fe center, and the NO_2-NO distance was varied in a stepwise manner. All other coordinates (except of the anchor atom of the distal histidine) were optimized. A similar approach was used for calculating structures along the N_2O_3 dissociation coordinate. The applicability of this approximation, i.e. fixing the porphine ring in space, was tested for the Fe-N_2O_3(-) distances of 2.1 Å and infinity (completely dissociated complex) by using the obtained structures, and allowing the porphine ring to optimize in a

following calculation (see below). In both cases, the obtained change in relative energy caused by optimizing the porphine ring was less than 7%. The interaction of NO with **1** was investigated using the B3LYP functional[15] and the LANL2DZ basis set[16] for the geometry optimizations. Since this process did not lead to the formation of a stable product, the PES was not recalculated with BP86/TZVP in this case. The dissociation of N_2O_3 from **2a** was treated in an identical manner as the association of NO, using BP86/TZVP to calculate the relevant geometries. However, since the dissociation process of N_2O_3 is associated with a transition of the heme from low-spin to high-spin, final energies were calculated using B3LYP/TZVP single points on the BP86/TZVP structures in this case, delivering a N_2O_3 dissociation energy of +6.5 kcal/mol. We also attempted to optimize the starting and ending structures for the N_2O_3 dissociation reaction with B3LYP/TZVP. In this case, a N_2O_3 dissociation energy of about +3 kcal/mol was obtained, but the ferric N_2O_3(-) complex has somewhat diminished spin densities, which makes this number less reliable. Application of B3LYP is necessary here because it is known from the literature that gradient-corrected functionals like BP86 are not able to reproduce the relative energies of different spin-states of a transition metal complex accurately. In contrary, these methods generally favor low-spin ground states even for five-coordinate ferrous heme centers,[17] which experimentally are known to be high-spin. Because of this, the spin crossover observed during N_2O_3 dissociation also requires that in this case, B3LYP energies have to be considered. The energies of the final high-spin and low-spin N_2O_3-dissociated products were determined by separately optimizing our five-coordinate Hb/Mb(II) model systems and N_2O_3 at the BP86/TZVP theory level, followed by B3LYP/TZVP single point energy calculations. In order to accurately model the Fe displacement from the porphyrin ring in five-coordinate hemes, these structures were first optimized with only the porphine ring and the anchor atom of the distal histidine fixed in space (see above). This allowed Fe to move out of the heme plane, and resulted in a longer distance between Fe and the terminal C-atom (anchor atom) of the distal histidine. The structures were then further optimized by fixing the Fe center and now allowing the porphine ring to optimize (still keeping the anchor atom of the distal histidine fixed). All geometry optimizations and single point energy calculations were preformed with the program package Gaussian 03.[18] Orbitals were visualized using GaussView.

References

(1) Diesen, D. L.; Hess, D. T.; Stamler, J. S. *Circ Res.* **2008**, *103*, 545. b) Gladwin, M. T. *Circulation*. **2008**, *117*, 594. c) Crawford, J. H.; Isbell, T. S.; Huang, Z.; Shiva, S.; Chacko, B. K.; Schechter, A. N.; Darley-Usmar, V. M.; Kerby, J. D.; Lang, J. D. Jr.; Kraus, D.; Ho, C.; Gladwin, M. T.; Patel, R. P. *Blood*. **2006**, *107*, 566. d) Singel, D. J.; Stamler, J. S. *Annu. Rev. Physiol.* **2005**, *67*, 99.

(2) Basu, S.; Grubina, R.; Huang, J.; Conradie, J.; Huang, Z.; Jeffers, A.; Jiang, A.; He, X.; Azarov, I.; Seibert, R.; Mehta, A.; Patel, R.; King, S. B.; Hogg, N.; Ghosh, A.; Gladwin, M. T.; Kim-Shapiro, D. B. *Nature Chem. Biol.* **2007**, *3*, 785. b) Miranda, K. M.; Espey, M. G.; Jourd'heuil, D.; Grisham, M. B.; Fukuto, J. M.; Feelisch, M.; Wink, D. A. The Chemical Biology of Nitric Oxide. In *Nitric Oxide: Biology and Pathology*; Ignarro, L. J., Ed.; Academic Press, **2000**, 41.

(3) Haldane, J. *J. Hyg.* **1901**, *1*, 115-122. b) Gladwin, M. T.; Grubina, R.; Doyle, M. P. *Acc. Chem. Res.* **2009**, *42*, 157.

(4) Einsle, O.; Messerschmidt, A.; Huber, R.; Kroneck, P. M. H.; Neese, F. J. *Am. Chem. Soc.* **2002**, *124*, 11737. b) Silaghi-Dumitrescu, R. *Inorg. Chem.* **2004**, *43*, 3715. c) Wyllie, G. R. A.; Scheidt, W. R. *Chem. Rev.* **2002**, *102*, 1067. d) Yi, J.; Heinecke, J.; Tan, H.; Ford, P. C.; Richter-Addo, G. B. *J. Am. Chem. Soc.* **2009**, *131*, 18119.

(5) Copeland, D. M.; Soares, A.; West, A. H.; Richter-Addo, G. B. *J. Inorg. Biochem.* **2006**, *100*, 1413. b) Yi, J.; Safo, M. K.; Richter-Addo, G. B. *Biochemistry*, **2008**, *47*, 8247.

(6) Vojtechovsky, J.; Chu, K.; Berendzen, J.; Sweet, R. M.; Schlichting, I. *Biophys. J.* **1999**, *77*, 2153.

(7) Blomberg, L. M.; Blomberg, M. R. A.; Siegbahn, P. E. M. *J. Biol. Inorg. Chem.* **2004**, *9*, 923.

(8) Ram, M. S.; Stanbury, D. M. *Inorg. Chem.* **1985**, *24*, 2954.

(9) Taylor, J. F.; Morgan, V. E. *J. Biol. Chem.* **1942**, *144*, 15.

(10) Gradient-corrected functionals like BP86 are generally not able to reproduce the relative energies of different spin states of transition metal complexes well. In order to investigate how a change in spin state affects the total energy for N_2O_3 dissociation, it is therefore inevitable to use hybrid functionals like B3LYP.

(11) a) Ghosh, A. *Coord. Chem. Rev.* **2009**, *253*, 523. b) Pierloot, K.; Vancoillie, S. *J. Chem. Phys.* **2006**, *125*, 124303. c) Praneeth, V. K. K.; Paulat, F.; Berto, T. C.; DeBeer George, S.; Näther, C.; Sulok, C. D.; Lehnert, N. *J. Am. Chem. Soc.* **2008**, *130*, 15288. d) Goodrich, L. E.; Paulat, F.; Praneeth, V. K. K.; Lehnert, N. *Inorg. Chem.* **2010**, *49*, 6293.

(12) Hopmann, K. H.; Cardey, B.; Gladwin, M. T.; Kim-Shapiro, D. B.; Ghosh, A. *Chem. Eur. J.* **2011**, *17*, 6348.

(13) a) Perdew, J.P. *Phys. Rev. B* **1986**, *33*, 8822. b) Becke, A. D. *J. Chem. Phys.* **1988**, *84*, 4524.

(14) a) Schaefer, A.; Horn, H.; Ahlrichs, R. *J. Chem. Phys.* **1992**, *97*, 2571. b) Schaefer, A.; Huber, C.; Ahlrichs, R. *J. Chem. Phys.* **1994**, *100*, 5829.

(15) a) Becke, A. D. *Phys. Rev. A* **1988**, *38*, 3098. b) Becke, A. D. *J. Chem. Phys.* **1993**, *98*, 1372. c) Becke, A. D. *J. Chem. Phys.* **1993**, *98*, 5648.

(16) a) Wadt, W. R.; Hay, P. J. *J. Chem. Phys.* **1985**, *82*, 270. b) Wadt, W. R.; Hay, P. J. *J. Chem. Phys.* **1985**, *82*, 284. c) Wadt, W. R.; Hay, P. J. *J. Chem. Phys.* **1985**, *82*, 299.

(17) a) Ghosh, A. *Coord. Chem. Rev.* **2009**, *253*, 523-525. b) Pierloot, K.; Vancoillie, S. *J. Chem. Phys.* **2006**, *125*, 124303.
(18) Frisch, M. J.; Trucks, G. W.; Schlegel, H. B.; Scuseria, G. E.; Robb, M. A.; Cheeseman, J. R.; Montgomery, Jr., J. A.; Vreven, T.; Kudin, K. N.; Burant, J. C.; Millam, J. M.; Iyengar, S. S.; Tomasi, J.; Barone, V.; Mennucci, B.; Cossi, M.; Scalmani, G.; Rega, N.; Petersson, G. A.; Nakatsuji, H.; Hada, M.; Ehara, M.; Toyota, K.; Fukuda, R.; Hasegawa, J.; Ishida, M.; Nakajima, T.; Honda, Y.; Kitao, O.; Nakai, H.; Klene, M.; Li, X.; Knox, J. E.; Hratchian, H. P.; Cross, J. B.; Bakken, V.; Adamo, C.; Jaramillo, J.; Gomperts, R.; Stratmann, R. E.; Yazyev, O.; Austin, A. J.; Cammi, R.; Pomelli, C.; Ochterski, J. W.; Ayala, P. Y.; Morokuma, K.; Voth, G. A.; Salvador, P.; Dannenberg, J. J.; Zakrzewski, V. G.; Dapprich, S.; Daniels, A. D.; Strain, M. C.; Farkas, O.; Malick, D. K.; Rabuck, A. D.; Raghavachari, K.; Foresman, J. B.; Ortiz, J. V.; Cui, Q.; Baboul, A. G.; Clifford, S.; Cioslowski, J.; Stefanov, B. B.; Liu, G.; Liashenko, A.; Piskorz, P.; Komaromi, I.; Martin, R. L.; Fox, D. J.; Keith, T.; Al-Laham, M. A.; Peng, C. Y.; Nanayakkara, A.; Challacombe, M.; Gill, P. M. W.; Johnson, B.; Chen, W.; Wong, M. W.; Gonzalez, C.; and Pople, J. A.; Gaussian, Inc., Pittsburgh PA, 2003.
(19) Yi, J.; Orville, A. M.; Skinner, J. M.; Skinner, M. J.; Ricter-Addo, G. B. *Biochemistry* **2010**, *49*, 5969.
(20) Yi, J.; Safo, M. K.; Richter-Addo, G. B. *Biochemistry* **2008**, *47*, 8247.

Chapter 7

Concluding Remarks

Since the discovery of nitric oxide (NO) as an essential biological signaling agent, research into the biological role of NO and metal nitrosyls has become a diverse and varied field.[1] In particular, the mechanism of NO reduction by denitrifying bacteria continues to garner the attention of the scientific community.[2-4] These bacteria contain the enzyme bacterial nitric oxide reductase (NorBC), which is known to facilitate NO reduction via a diiron heme/non-heme active site. Currently, the exact mechanism of reduction continues to be a point of controversy in the literature.[3] This thesis has been aimed at the use of synthetic model complexes of the NorBC active site to help elucidate the mechanism of NO reduction.

Firstly, sophisticated heme nitrosyl model complexes which employ covalently bound N-donor ligands were employed in order to develop true six-coordinate heme nitrosyls in solution. Here, the ligand T*o*-F_2PP-BzIM, which contains a tethered imidazole moiety bound to the *ortho*-phenyl position of a fluorinated TPP derivative, has been shown to promote imidazole coordination to the corresponding ferrous heme nitrosyl in solution. Detailed spectroscopic information was collected on [Fe(T*o*-F_2PP-BzIM)(NO)] and reveals a clean nine-line hyperfine splitting in the EPR spectrum. Additionally, infrared spectroscopy shows a ν(N-O) stretching feature at 1644 cm^{-1}. Interestingly, the strength of the Fe-(N-donor) bond in the benzyl-linked complex [Fe(T*o*-F_2PP-BzIM)(NO)] is still slightly weaker than that observed for [Fe(T*o*-F_2PP)(MI)(NO)] with free MI, as evidenced by the higher ν(N-O) stretching frequency. However, [Fe(T*o*-F_2PP-BzIM)(NO)] represents the first truly six-coordinate ferrous heme-nitrosyl which is stable in solution without the need for excess N-donor base. This complex provides a structurally accurate model for the proposed heme b_3 nitrosyl adduct in NorBC.

Second, biomimetic non-heme iron nitrosyls were developed in order to compliment the heme models presented in Chapter 2. Here, non-heme iron nitrosyls of the BMPA-Pr ligand provide accurate structural models for the

non-heme Fe_B site of NorBC. The [Fe(BMPA-Pr)(NO)]X series of compounds displays a remarkable range of ν(N-O) stretching frequencies based on the nature of the counter ion, X. DFT calculations coupled with detailed spectroscopic analysis has revealed the nature of NO in high-spin non-heme iron nitrosyls to be a strong π-donor ligand. As a result, the effective nuclear charge of iron can modulate this donation and thus dictate the strength of the N-O bond. Alternative non-heme iron nitrosyl complexes have also been investigated. Here, replacement of the carboxylate moiety in BMPA-Pr with a phenol functionality appears to result in a five-coordinate non-heme iron nitrosyl complex.

Next, the reactivity between synthetic heme and non-heme iron nitrosyl complexes has been investigated in an attempt to elucidate the mechanism of NO reduction by NorBC. A radical-based N-N coupling mechanism appears unlikely based on the observed lack of reactivity between a variety of iron nitrosyl complexes. As an alternative, non-heme iron nitrosyl complexes were chemically and electrochemically reduced in an attempt to probe an alternative redox-type couple involving a non-heme $\{FeNO\}^8$ complex. However, reduction of [Fe(BMPA-Pr)(NO)]X results only in formation of a structurally uncharacterized dinitrosyliron complex (DNIC). A more sterically hindered nitrosyl moiety is likely required to prevent DNIC formation and favor reduction to the desired $\{FeNO\}^8$ complex. In addition to assaying the reactivity of separate heme and non-heme iron nitrosyl complexes, the synthesis of a covalently linked heme/non-heme construct has been developed. Preliminary synthetic efforts show the formation of a stable di-ferric oxo-bridged species which is susceptible to reduction and subsequent NO binding.

In addition, the hyponitrite-bridged complex $[(OEP)Fe]_2(\mu\text{-}N_2O_2)$ has been investigated in collaboration with Dr. George B. Richter-Addo and coworkers at the University of Oklahoma.[5] This complex offers a unique opportunity to probe the reactivity and electronic structure of the proposed hyponitrite intermediate formed during NO reduction by NorBC. SQUID susceptibility shows an overall S = 3 spin which likely results from the ferromagnetic coupling of two intermediate S = 3/2 spin [Fe(OEP)] units. The vibrational properties of $[(OEP)Fe]_2(\mu\text{-}N_2O_2)$ have also been clarified using IR and NRVS spectroscopy coupled with DFT calculations. Interestingly, $[(OEP)Fe]_2(\mu\text{-}N_2O_2)$ has been shown to thermally decompose over several hours to yield [Fe(OEP)(NO)] at a rate of $6.4\text{x}10^{-5}$ s^{-1}. Addition of an axial base such as 1-methylimidazole drastically increases the rate of this decomposition to a maximal value of $1.24\text{x}10^{-3}$ s^{-1}.

Finally, DFT calculations have been employed to examine the likelihood of N_2O_3 formation as a result of NO attack on *in silico* models of nitrite-bound hemoglobin (Hb) and myoglobin (Mb). The calculations show that both the addition of NO to Hb/Mb(III)-NO_2^- and the dissociation of N_2O_3 from the resulting Hb/Mb(III)-N_2O_3(-) species are energetically feasible, resulting in a total energy for the complete process of -1 to -3 kcal/mol. One important restriction for this process is that this reaction is only possible in the ferric nitrito (O-bound) binding mode of nitrite; otherwise, this reaction is energetically very unfavorable. Additionally, the incorporation of a distal histidine residue in the Hb/Mb active site model significantly lowers the predicted free energy of this process in comparison to model systems lacking this residue;[6] further supporting the possibility of N_2O_3-mediated hypoxic signaling.

Future work on this project should focus on probing alternative heme and non-heme iron nitrosyl/nitroxyl reaction pathways. Based on the work presented in this thesis, a radical based coupling mechanism in unlikely. However, reduction of the non-heme iron nitrosyl to the corresponding {FeNO}^{8} species, via electron transfer from heme b_3, may result in a reactive Fe_B(II)-NO^- /Fe_{b3}(II)-NO^+ pair. The reactivity of such a species can be probed with model complexes via synthesis of ferric heme nitrosyl complexes (which have been reported previously) and reduced high-spin {FeNO}^{8} non-heme iron nitroxyl complexes (which are currently being investigated in the Lehnert laboratory). Reactivity studies using these two synthetic complexes will provide valuable insight into the mechanism of NO reduction by NorBC.

References

(1) Lehnert, N.; Scheidt, W. R., *Inorg. Chem.* **2010,** *49*, 6223.
(2) Hino, T.; Nagano, S.; Sugimoto, H.; Tosha, T.; Shiro, Y., *Biochim. Biophys. Acta.* **2012,** *1817*, 680.
(3) Moenne-Loccoz, P., *Nat. Prod. Rep.* **2007,** *24*, 610.
(4) Wasser, I. M.; de Vries, S.; Moenne-Loccoz, P.; Schroder, I.; Karlin, K. D., *Chem. Rev.* **2002,** *102*, 1201.
(5) Xu, N.; Campbell, A. L. O.; Powell, D. R.; Khandogin, J.; Richter-Addo, G. B., *J. Am. Chem. Soc.* **2009,** *131*, 2460.
(6) Hopmann, K. H.; Cardey, B.; Gladwin, M. T.; Kim-Shapiro, D. B.; Ghosh, A., *Chem. Eur. J.* **2011,** *17*, 6348.